Single molecule force spectroscopy study of integrins and syndecans interactions in bladder cancer cells

Joanna Danilkiewicz

Rozprawa doktorska wykonana pod kierunkiem
prof. dr. hab. Wojciecha Kwiatka
oraz
dr Katarzyny Pogody
w Zakładzie Biofizyki Mikrostruktur
Instytutu Fizyki Jądrowej
Polskiej Akademii Nauk w Krakowie

Doctoral thesis under supervision of
prof. dr hab. Wojciech Kwiatek
and
dr Katarzyna Pogoda
in the Department of Biophysical Microstructures
Institute of Nuclear Physics
Polish Academy of Sciences

Kraków, 2020

To the author of Lorem Ipsum

Acknowledgements

I would like to express my sincere gratitude and deep appreciation to my thesis supervisors professor Wojciech Maria Kwiatek and doctor Katarzyna Pogoda for their invaluable help, for all the great advice both scientific and non-scientific, and for the trust they have put in me.

I would also like to thank professor Małgorzata Lekka of Department of Biophysical Microstructures where the AFM measurements were prformed and all the current and past members of the Department of Biophysical Microstructures who made wonderful colleagues all that time. Many thanks also to the Department of Biophysical Microstructures technicians: Joanna Wiltowska-Zuber, Joanna Pabijan, Klaudia Suchy for providing great support in regard of cell culture and laboratory maintenance.

Let me put on record my appreciation and deep gratitude to the head of the Institute of Nuclear Physics PAS professor Marek Jezabek, International Doctoral Studies INP PAS heads professor Tadeusz Lesiak, professor Anna Kaczmarska and especially professor Andrzej Horzela for their exceptional help, understanding and compassionate approach to proteges.

I sincerely acknowledge professor Piotr Laidler and his group for a constructive discussion.

Last but not least, I would love to thank my parents, friends and family for all the love and support I got from them and for that they believed in me more than I did myself. I especially thank Michał Seneka Kański the Fearless Misspelling Vanquisher, Father to the Commas, Him Who Tames the Silly Sorrows, and Andrea Politano that he is and that I am.

The AFM (Nanowizard 4, JKP Instruments), laminar chamber for cell culture and incubator purchase has been realized under the project co-funded by the Małopolska Regional Operational Program, Measure 5.1 - Krakow Metropolitan Area as an important hub of the European Research Area for 2007-2013, project no MRPO.05.01.00-12-013/1.

Podziękowania

Chciałabym bardzo serdecznie podziękować państwu prof. Wojciechowi Kwiatkowi i dr Katarzyie Pogodzie za nieocenioną pomoc, konsultacje zarówno w zakresie czysto naukowym i nie tylko oraz pokładaną we mnie wiarę.

Dziękuję również prof Małgoracie Lekkiej, kierowniczce Zakładu Badania Mikrostruktur Biofizycznych, gdzie przeprowadziłam badania AFM oraz wszystkim byłym i obecnym kolegom z Zakładu Badania Mikrostruktur Biofizycznych, z którymi wspaniale mi się współpracowało. Wielkie podzięowania również dla pań techniczek Zakładu Badania Mikrostruktur Biofizycznych: Joanny Wiltowskiej-Zuber, Joanny Pabijan i Klaudii Suchy za ogromną pomoc w ramach hodowli komórkowej i utrzymaniu funkcjonowania laboratorium.

Chciałabym wyrazić również ogromne uznanie i wdzięczność względem prof Marka Jeżabka dyrektora IFJ PAN oraz kierowników Międzynarodowego Studium Doktoranckiego IFJ PAN prof. Tadeusza Lesiaka, prof. Anny Kaczmarskiej, a szczególnie prof. Andrzeja Horzeli za ich niesamowitą pomoc, opiekę i pełne zrozumienia podejście do podopiecznych.

Podziękowania dla profesora Piotra Leidlera za pomoc w postaci konstruktywnej dyskusji.

W końcu chciałabym podziękować rodzicom, przyjaciołom i rodzinie za okazaną miłość i wsparcie oraz za to, że wierzyli we mnie bardziej niż ja sama. Szczególnie dziękuję Michałowi Senece Kańskiemu, niestrudzonemu pogromcy literówek, ojcu przecinkom i tępicielowi smętnych przemyśleń oraz Andrei Politano za to, że on jest i ja jestem.

Zakup komory laminarnej do hodowli komórkowej oraz inkubatora został współfinansowany w ramach projektu the Małopolska Regional Operational Program, Measure 5.1 - Krakow Metropolitan Area as an important hub of the European Research Area for 2007-2013, project no MRPO.05.01.00-12-013/15.

Zakup mikroskopu sił atomowych (Nanowizard 4, JKP Instruments) został zrealizowany w oparciu o project: Małopolska Regional Operational Program, Measure 5.1 – "Krakow Metropolitan Area as an important hub of the European Research Area" for 2007-2013, numer projektu MRPO.05.01.00-12-013/15.

Contents

Nomenclature

aa amino acid

AFM atomic force microscopy

AMIDAS adjacent metal ion dependent adhesion site

APTES 3-amino-propyltriethoxysilane

ATCC American Type Culture Collection (Manassas, VA, USA)

BE Bell-Evans (model)

BL BioLever BL-RB150VB AFM probe (100 μm long cantilever)

c-Src tyrosine-protein kinase Src

CASK Ca^{2+}/calmodulin-associated Ser/Thr kinase

CBC contact based calibration

CFC contact free calibration

CS chondroitin sulphate

DFS dynamic force spectroscopy

DHS Dudko-Hummer-Szabo (model)

EDTA ethylenediaminetetraacetic acid

EWLC extensible worm-like chain (model)

FAK focal adhesion kinase

FAs focal adhesions

FBS foetal bovine serum

FD force-distance (curve)

FFT fast Fourier transform

FN fibronectin

FN4-12 fibronectin III fragment 4-12, FNIII4-12

FNY Friddle-Noy-De Yorego (model)

GA glutaraldehyde

GTP guanosine-5'-triphosphate

HEPES 4-(2-hydroxyethyl)-1-piperazineethanesulfonic acid

HS heparan sulphate

HSA human serum albumin

IC50 half maximal inhibitory concentration

LDV laser Doppler vibrometer

Mab monoclonal antibody

MIDAS metal ion dependent adhesion site

OPN osteopontin

PBS phosphate buffer saline

PDMS polydimethylsiloxane

PDZ *P*SD-95, *d*iscs large, *Z*O1 (domain)

PEG polyethylene glycol

pFA para-formaldehyde

PSD power spectral density

RMS root mean square

RT room temperature

SCFS single cell force spectroscopy

SD mean standard deviation

SDC-1 syndecan-1

SDC-4 syndecan-4

SDCs syndecans

SHO simple harmonic oscillator

SMC smooth muscle cells

SPM scanning probe microscopy

TR400 OMCL TR400PSA-1 AFM probe with 200 μm long cantilever

TRITC tetramethylrhodamine

VdW Van der Waals (interactions)

VN vitronectin

WLC worm-like chain (model)

Symbol index

α_1, α_2 electronic polarizabilities of molecules

ϵ dielectric constant in water

ϵ_0 dielectric constant of vacuum

η medium viscosity

Γ hydrodynamic function

γ empirical parameter of Dutko-Hummer-Szabo model equal to 0.5772

s $\Lambda(Re)$ hydrodynamic function of an arbitrary shape cantilever

ν_1 and ν_2 ionization potentials

ρ_c cantilever density

ρ_m medium density

ρ_w water density

τ complex bond lifetime

τ_0 complex bond lifetime in the absence of external force

ω_0 harmonic oscillator or cantilever resonance frequency

ω_{vac} cantilever resonance frequency in vacuum

A_0 resonance amplitude (of a cantilever)

A_{noise} noise amplitude (of fluctuations)

a slope of Bell-Evans model fit

a_{eff} effective tip radius

b intercept of Bell-Evans model fit

c_1, c_2 Lorenz function fit constants

D relative tip-sample distance

D_{dif} local diffusion rate

$< d^2 >$ mean square displacement

d cantilever displacement

d_c cantilever bending

d_i sample indentation

E Young's modulus

E_{stored} energy stored in an oscillator

E_{diss} energy dissipated per oscillation cycle

F external pulling force

F_{adh} adhesion force

F_c critical force (upon which a bond breaks)

F_{drag} hydrodynamic drag force

F_{Hook} force in a Hooke's law

F_{unb} the most probable unbinding force

F_{unsp} the most probable non-specific adhesion force

F_{EWLC} pulling force in the Extensible Worm Like Chain model

E_b energy barrier height

G' storage modulus

G_0 free energy of a complex

G* free energy of a complex pulled away with the F force

h tip height

h_P Planck constant

h_{cant} cantilever thickness

h_{eff} effective tip height

J flux across the potential barrier

k force constant

k_0 off-rate in the absence of pulling force

k_B Bolzman constant

k_{cant} cantilever force constant

k_{comp} receptor-ligand complex stiffness

$\frac{k_{dyn}}{k_{stat}}$ ratio of dynamic and static spring constants

k_{off} reaction off-rate also known as dissociation rate

k_{SHO} simple harmonic oscillator fundamental mode spring constant

k_{sys} force constant of a system

L cantilever longest dimension (length)

L_0 linear dimension length scale of the flow

L_c Worm-like chain model polymer contour length

L_P polymers persistence length

l_r loading rate

m cantilever mass

M_e effective mass

Q quality factor

P probability of single rupture event

P_L persistence length

r distance between interacting surfaces, atoms or molecules

$\vec{r}(s)$ position vector along the chain: s$\in (0, L_c)$

Re Reynolds number

S probability function of a complex survival after time t

s sensitivity

T temperature

t time

u_1, u_2 molecule dipole moments

v velocity

v_{cant} cantilever tip velocity

w rectangular cantilevers width, triangular cantilevers one arm width

w_i the potential of interactions i=vdW Van der Waals interaction potential, i = K Keesom force potential, i=D Debye force potential

W_{adh} work of adhesion (specific and unspecific combined)

x reaction or force pulling coordinate

x_b bond length in the absence of pulling force

Z cantilever position during AFM measurements

$< z^2 >$ time average mean square of a cantilever deflection

Amino acid sequences

GRGD Gly-Arg-Gly-Asp

GRGDTP Gly-Arg-Gly-Asp-Try-Pro

PHSRN Pro-His-Ser-Arg-Asn

Streszczenie

Celem niniejszej pracy doktorskiej było sprawdzenie stosowalności dynamicznej spektroskopii sił AFM w opisie mechanizmu oddziaływań adhezyjnych peptydów i przeciwciał do receptorów obecnych na powierzchni żywych komórek. Praca dostarcza opisu różnic krajobrazu energetycznego wiązania wybranych fragmentów fibronektyny i monoklonalnych przeciwciał przeciwko syndekanom w zależności od stopnia złośliwości komórek nowotworu pęcherza. **Hipoteza pracy zakłada, że parametry krajobrazu energetycznego oddziaływań adhezyjnych wyznaczone za pomocą dynamicznej spektroskopii sił AFM pozwalają na rozróżnienie przerzutujących i nieprzerzutujących linii komórek raka pęcherza moczowego.** Praca zawiera optymalizację procedury pomiaru dynamicznej spektroskopii siły na żywych komórkach oraz analizy specyficznych oddziaływań adhezyjnych. W oparciu o dane eksperymentalne przetestowano przewidywania dwóch teoretycznych modeli pozwalających na wyznaczenie parametrów oraz rekonstrukcję obrazu energetycznego zerwania wiązania: fenomenologicznego modelu Bella-Evansa i deterministycznego modelu Dudko-Hummer-Szabo. Oba modele umożliwiają analizę zależności siły adhezji od szybkości przykładania siły zrywającej pozwalając na wyznaczenie parametrów opisujących kinetykę oraz szerokość bariery potencjału tego procesu. Wyniki posłużyły do stwierdzenia, że model Dudko-Hummer-Szabo, który jest bardziej realistyczny oraz wzbogacony o energię swobodną zerwania wiązania, charakteryzuje się wyższą wiarygodnością. Jednocześnie, model Bella-Evansa, pomimo swojego uproszczenia, może służyć do zgrubnego opisu różnic kinetyki zrywania pojedynczych wiązań. Zaangażowanie modelu Extensible Worm-Like-Chain znanego z fizyki polimerów oraz rozciągania białek było kluczowe dla postępu pracy i pozwoliło na rozróżnienie pomiędzy zerwaniem niespecyficznych wiązań od specyficznych oraz obliczenie prędkości obciążania (loading rate) siły rozciągającej w momencie tuż przed zerwaniem wiązania. Badanie wykonano przy pomocy próbników AFM funkcjonalizowanych krótkim heksapeptydem GRGDTP, dłuższym fragmentem modułu III fibronektyny FN4-12 na powierzchni niezłośliwych komórek nowotworu przewodu moczowego oraz komórek nowotworu pęcherza trzeciego stopnia złośliwości. Eksperyment z monok-

lonalnymi przeciwciałami przeciwko syndekanowi-1 i syndekanowi-4 został rozszerzony o panel komórek: niezłośliwego nowotworu nabłonka pęcherza moczowego, drugiego i trzeciego stopnia nowotworu pęcherza oraz przerzutujących komórek nowotworu pęcherza. Uzyskane wyniki pozwoliły na charakterystykę kinetyki oddziaływań adhezyjnych peptydów oraz przeciwciał do powierzchni żywych komórek przy zastosowaniu dynamicznej spektroskopii sił AFM. Parametry krajobrazu energetycznego wyznaczone przy zastosowaniu modeli Bell-Evansa oraz Dutko-Hummer-Szabo pozwoliły na rozróżnienie pomiędzy niezłośliwymi, złośliwymi i przerzutującymi komórkami raka pęcherza moczowego, dowodząc słuszności postawionych tez pracy doktorskiej. Uzyskany wynik nie jest jednak prostą funkcją stopnia złośliwości badanych komórek, co zostało przedyskutowane w oparciu o złożoność badanych układów biologicznych.

Summary

The doctoral thesis aims to examine the applicability of AFM dynamic force spectroscopy in the description of mechanism of peptides and antibodies adhesion to the surface of living cells. It provides insight in fibronectin fragments and syndecan monoclonal antibodies of choice binding energy landscape distinctions depending on the malignancy grade of bladder cancer cell line. **The hypothesis states that differences in unbinding energy landscape parameters, measured by AFM dynamic force spectroscopy, are sufficient to distinguish between transitional, malignant, and non-malignant bladder cancer cells.** The work included dynamic force spectroscopy measurement on live cells optimization and specific adhesion forces analysis protocol. Basing on experimental data, the two theoretical models, that include unbinding energy landscape parameters reconstruction, were examined: the phenomenological Bell-Evans and the deterministic Dudko-Hummer-Szabo. Both models allow the determination of adhesion dependence on force loading rate, kinetic parameters of a process, and the corresponding bond length. The results suited to conclude that the Dudko-Hummer-Szabo model predictions are more realistic, enriched with unbinding free energy parameter,and hence more robust. Simultaneously, Bell-Evans model, despite its simplistic approach, can suit to describe the approximated differences between kinetic parameters of single unbinding events. The crucial part of this work was an incorporation of Extensible Worm-Like-Chain model known from polymer physics and proteins unfolding, in order to distinguish specific unbinding events, and to calculate system loading rates of pulling forces in the last moment before specific unbinding event. The study included experiments with AFM probes functionalized with short GRGDTP hexapeptide, and longer fibronectin III fragment FN4-12 against the surface of non-malignant cells of ureter and grade 3 bladder cancer. The experiment with AFM probes functionalized with monoclonal antibodies against syndecan-1 and syndecan-4 was extended to test a panel of five different cell lines including: non-malignant cells of ureter, grade 2, grade 3, and transitional bladder cancer cells. AFM dynamic force spectroscopy on the surface of living cells allowed to decode the peptides' and the antibodies' adhesion ki-

netic parameters calculated with Bell-Evans and Dudko-Hummer-Szabo models. The thesis was confirmed due to the differences in energy landscape parameters that allowed to distinguish between non-malignant, malignant and transitional cell lines. Obtained result is not a simple function of malignancy grade as discussed based on the biological systems complexity.

1 Introduction

The thesis principle topic focuses on the robust and complex analysis of specific adhesive properties and energy landscapes of integrins and syndecans binding extracellular matrix proteins of choice in different grade of malignancy bladder cancer cells. The choice of intact living cells rather than purified proteins ensures the orientation allowing binding and preserves post-translational modifications crucial to examine not only the expression of assessed molecules but also their unbinding energy landscape. The term "specific force" or "specific interaction" is henceforth interpreted as forces present exclusively between a specific pair of ligands of interest. Such interactions result in relatively strong adhesion between molecular groups. The specific interactions may be distinguished from non-specific through examination of AFM force-distance curves shape denoting the type of physical interactions between examined molecules. An important part of this work is the determination of specific and distinction from the unspecific interactions. The specific receptor-ligand interactions play crucial role in a variety of biological interactions, reflect the cells membrane composition, participate in cell-environment communication. The transmembrane receptors, including integrins and syndecans, altered expression is common in cancerous cells [45, 69, 108, 121]. Many proteins function as mechanoreceptors so the information about their mechanical energetic landscape reflects their physiological function. Moreover, to mediate multiple functions, integrins exhibit structural diversity, flexibility, and are capable of conformational changes. The members of mentioned surface receptor families are binding extracellular matrix proteins: fibronectin (FN) and vitronectin (VN). Nevertheless, expression of surface receptors is not the only parameter relevant for the cells interactions and intrinsic processes; equally crucial are the interactions between ligands and receptors dependent on their ligation with ions, polysaccharides etc. The functional properties of ligand-receptor relations are highly dependent on the complex conformation resulting in altered interactions between its atoms and thereafter in altered nano-mechanical and adhesive properties as shown on the example of integrins [60]. The RGD containing peptides binding to integrins and syndecans to their monoclonal antibodies might suit as an example of complex conformational

changes being more crucial for the regulation of receptor function than surface expression or clustering.

The main aim of this work is a robust, quantitative characterisation of specific nanoscale adhesion forces of fibronectin and vitronectin associated molecular complexes interactions in different levels of malignancy bladder cancer cells. The direct examination of interaction forces assures extensive insight into the nanoscale mechanics of a biological system. The dynamic force spectroscopy (DFS) probes the inner properties of molecular interactions yielding in the insight in properties that are difficult or impossible to detect in near equilibrium dissociation assays. The aim of the thesis is to firstly, develop robust procedure for AFM data collecting and analysis and then to compare the parameters of energy landscape of integrins and syndecans complexes types with the two ECM proteins of choice (fibronectin and vitronectin). Within the course of thesis preparation, I aimed to understand and describe the mechanism of selective receptor recognition process through studies of force interactions of single and multiple molecular complexes involving integrins and syndecans in nanoscale. The work aims to deepen the knowledge on physical base of mechanisms of integrins and syndecans synergistic binding to fibronectin and vitronectin.

To achieve PhD thesis aim, an atomic force microscopy (AFM) technique was applied working in a single-molecule and single-cell force spectroscopy mode in order to collect data that suited to calculate unbinding energy landscape parameters of molecules of choice on the surface of live cells. In addition fluorescence microscopy was involved to image the structures of the cells. The experiments were performed on bladder cancer cell lines: non-malignant cell cancer of ureter cells, grade 2-4 bladder carcinoma including two transitional lines. Such a broad panel of bladder cancer cells was selected to assess the interactions on all levels of malignancy in live cells. Bladder cancer is diagnosed in almost 550 thousands of patients yearly [59]. The death toll in 2018 equalled almost 200 thousands of patients [59] which pose a highly disturbing ratio. Such a high death rate suggests poorly developed specific treatment and early diagnosis procedures that should be improved.

Experimental data interpretation lead to the thesis that AFM based specific adhesion properties of ECM proteins examination may suite as a tool for selective detection of cancerous cells and malignancy prognostic parameter. The crucial point of the thesis preparation was adjustment of dynamic force spectroscopic (DFS) experiments and data analysis procedure the way it provided robust results for living cells. It was obtained thanks to a specific AFM probe functionalization and employment of a model known from polymer physics in order to distinguish specific unbinding events basing on the curve shape. Thus, the worm-like chain model was employed to describe processes on the elastic membrane. The unbinding forces collected this way were fitted with two distinct models calculating the unbinding energy landscape parameters. The Bell-Evans (BE) and the Dudko-Hummer-Szabo (DHS) models were then compared as they helped to describe different aspects of unbinding dynamics.

2 The current state of knowledge

2.1 Fibronectin and vitronectin as extracellular matrix proteins

Extracellular matrix (ECM) provides chemical and mechanical cues, anchorage and support for immersed cells required for tissue morphogenesis, stem cell differentiation, homoeostasis and cancer progression. Cells can sense the matrix rigidity and adapt the strength of membrane receptors (integrins) linkage with cytoskeleton accordingly [32]. It contains mainly water and a variety of polysaccharides and proteins including proteoglycans (PGs) composed of protein core covalently linked to a glycosaminoglycan (GAG) chains and fibrous proteins such as collagens, fibronectin, vitronectin. The main proteins of interest are ECM ingredients: fibronectin (FN) and less studied vitronectin (VN). Fibronectin and vitronectin are non-collagenous proteins that are a constituting major component of extracellular matrix surrounding cells. These proteins serve as anchoring sites for cells mainly through the RGD motif, by which they bind to integrins and hence actively participate in regulation of such cellular functions like adhesion [93, 150, 166], motility, modulation of extracellular signals, metastasis [105, 210] and cytokine as well as growth factor association [16, 21, 27, 46]. FN is observed as a dimer joined by two C-terminal disulphide bonds and is capable of other FN dimers, collagen, heparin and cell-surface integrin receptors binding. FN fibrils pose a crucial factor in mediating cell attachment and migration. Their type III modules super-molecular assemblies are continuously, dynamically stretched by cell traction forces [183]. Fibronectin III characterizes with multiple binding sites including RGD sequence on FNIII10, LDV on FNIII5 and PHSRN on FNIII9 and HepII on FNIII12-14 modules respectively as pictured in the Fig. 1. Vitronectin also characterize with the presence of RGD sequence. As a multifunctional serum protein, it is present in many locations in the animal organisms. VN was proven to localize within the stroma of wound tissue together with FN [75] where it plays a crucial role due to the ability to bind heparin [43] and in the late-stage glioblastoma parenchyma. Simultaneously, it is not present in normal glia nor in early stage tumours [71].

VN present in human bladder originates from two sources: localized synthesis by urothelial cells and transport with bloodstream from liver [227]. On the contrary, it is not present on the epithelial bladder basal membrane that contains FN [215]. The schematic structure and interactions of fibronectin are presented in Fig. 1. Another less known RGD containing protein osteopontin (OPN) was found in elevated levels in plasma of patients with transitional bladder cancer [3]. Human T24 bladder cancer cells express OPN and therefore it was proposed as a potential cancer progression marker [224, 226]. Simultaneously, it was not found in normal bladder tissue [17].

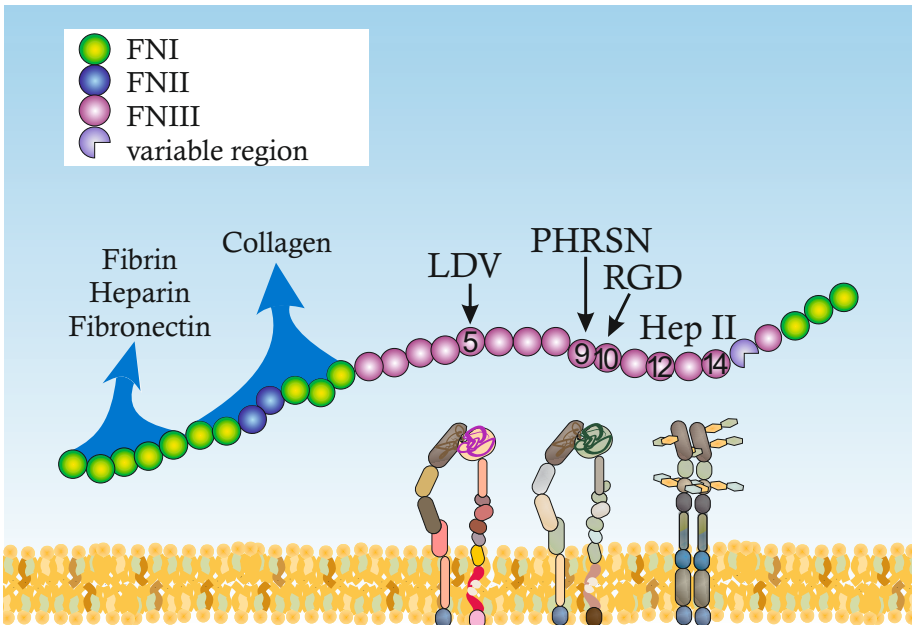

Figure 1: Fibronectin structure: colours designate different FN modules with LDV motif present on FNIII5, PHSRN on FNIII9, RGD on FNIII10 and hepII on FNIII12-14. Fibrin binding region 2 on FNII and heparin and FN binding motifs on FNIII12-14 and glycans are omitted for the image clarity. RGD cooperates with PHSRN in integrin binding process while LDV is a part of complexes with distinct integrins. Schematic image out of scale.

2.2 The integrins conformations and their ligands

Integrins are cell adhesion, transmembrane, heterodimeric receptors that transduce bidirectional signals across plasma membrane. Integrins are the key nexus element connecting all the proteins inside the cell named adhesome and the extracellular matrix environment of a cell. Thus, they mediate actin cytoskeleton interactions with the cell environment. The adhesome contains depending on the report up to 2400 proteins out of which 60 were assigned as functionally crucial consensus adhesome based on both literature screening and proteomic mass spectrometry experiment [86, 87]. The integrins are composed of two subunits i.e. α and β, both contain short cytoplasmic transmembrane and large extracellular domain [4]. Integrins are in their active state while dimerized creating the large "head" and ligand-binding socket in which β subunit is repositioned toward RGD-binding motif to create stable high-affinity complex [222]. It is typical for several receptors from integrin family to bind RGD amino acid sequence present in extracellular matrix (ECM) proteins. The RGD motif recognition domain is present in several integrins specifically binding either to fibronectin (FN) and/or to vitronectin (VN) [152] and/or to osteopontin (OPN). Examples are $\alpha_5\beta_1$, $\alpha_4\beta_1$, $\alpha_V\beta_6$, $\alpha_{IIb}\beta_3$ binding FN, $\alpha_8\beta_1$, $\alpha_V\beta_1$, $\alpha_V\beta_3$ binding both VN and FN, and $\alpha_V\beta_5$, $\alpha_V\beta_8$ selective for VN [5,6,92,152,186,223]. Additionally, osteopontin creates complexes with $\alpha_5\beta_1$, $\alpha_V\beta_1$, $\alpha_V\beta_3$, $\alpha_V\beta_5$ RGD binding domains [39]. However these are not the only integrin ligands. For example integrin $\alpha_V\beta_3$ was reported to bind also to denatured collagen type I through the RGD motif [42] and $\alpha_{IIb}\beta_3$ to fibrinogen in a manner implying two bound states and more complex mechanism than simple RGD binding [123]. For the sake of image clarity laminin and collagens were omitted in the Fig 2 representing the RGD based complexes of integrins and distinct ECM components. The $\alpha_5\beta_1$ integrin was believed to be specific for the interaction with fibronectin, in which it recognizes and binds preferentially to the RGD motif [122] before it appeared to bind OPN as well. Moreover, osteopontin activates $\alpha_V\beta_3$ integrin boosting $\alpha_5\beta_1$ growth factor signaling in non-small cells lung cancer and facilitates cancer progression due to growth factor receptor inhibition [22]. However, these are not only examples of integrin family members. The described

receptors mediate distinct bidirectional functions connecting ECM molecules to signalling and cytoskeletal molecules inside a cell thanks to their diverse structure, molecular dynamism, and flexibility. The α_3, α_V, β_1 and β_4 subunits were discovered in proper bladder epithelial cells while α_5 and β_3 were excluded by the same immunohistochemical scrutiny [215].

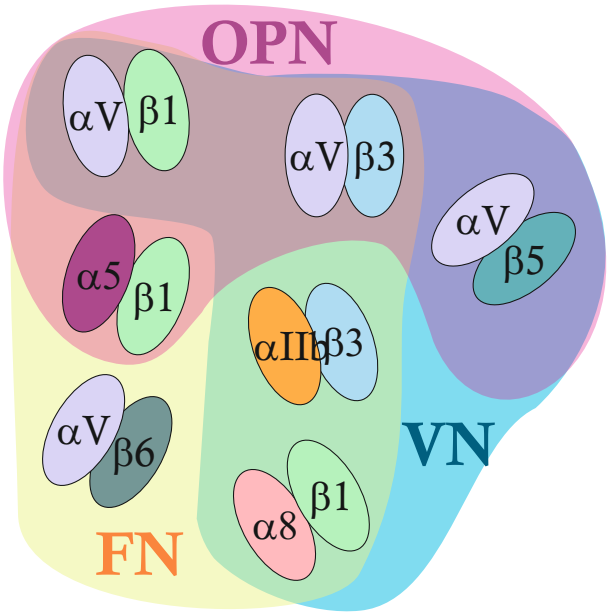

Figure 2: Scheme of distinct integrins binding to fibronectin (FN), vitronectin (VN) and/or osteopontin (OPN).

Integrins exist in three states: inactivated, activated and specifically activated that have different both affinities and, as a result of clustering in focal adhesions (FAs), also avidities[1] [66,67]. Mechanisms proposed to describe the avidity changes in integrin $\alpha_4\beta_1$ rely on changes in the number of interacting molecules due to the alteration of the receptor topology or differences in the affinity of the individual bonds [30, 31]. The observation was confirmed also for $\alpha_{IIb}\beta_3$ integrin for which there was observed polyvalent binding after clustering based activation with a chemical agent (rhodostomin) [88]. Altogether affinity regulation is proposed to

[1]The overall strength of cellular adhesiveness

be a major factor that governs the avidity of β_1 integrins. Simultaneously, FN causes retention of mature β_1 integrins on the cell surface. The initiation of final differentiation in keratinocytes with occupied β_1 integrin subunit is independent of cytoskeleton assembly [208]. This kind of behaviour is characteristic for cancerous cells. Integrins can be put in an open, enabled for ligand binding, state when they are activated by either antibodies, high concentrations of extracellular magnesium and manganese ions outside-in and inside-out signalling molecules like for example talin [194] or kindlin-2 phosphorylating a tyrosine binding pocket [179]. For example talin binds to the β subunit that changes its conformation by separation of the cytoplasmatic and transmembrane subunits fragments [207]. Such a conformation stabilises extended integrin form and results in the raised ligand-binding affinity [126, 196]. Integrins heterodimers crystallization experiments proved them to exist in a bent conformation [223] that is supposed to be inactive [139]. The widely believed model of integrin activation assumes that integrin extension (open headpiece) is mechanically linked to high affinity state [181]. According to a standard model, integrins can take three distinct conformations: bent with low affinity headpiece and extended with either high or low affinity headpiece. However, in the last decade there were many implications that intermediate functional forms exist as well i.e. not fully bent conformer or bent conformations capable of binding ligands. Electron microphotography of $\alpha_V\beta_3$ integrin in the Ca^{2+} buffer can reach between 90° and 135° while the bent structure unable to bind ligands is at 135° as obtained from crystallography [196]. On the other hand Takagi et. al. rotary shadowed images of integrin $\alpha_5\beta_1$ suggested that C-terminal opening of integrin can result in its activity independent from bending [195]. Simultaneously, bent conformation $\alpha_V\beta_3$ integrin creating a complex with RGD peptide was crystallized [223] and a complex with fibronectin fragment was visualised with TEM [1]. This would suggest that a rapid stepwise conversion between bent and extended states does not occur and intermediate forms play significant role in ligand binding. It is believed that grouping of integrins by multivalent ligands enhances their avidity along with introducing changes in membrane fluidity [24]. Mg^{2+} ions are proven to increase the affinity of integrins [65] and to be necessary for metal ion de-

pendent site (MIDAS) integrins activation [115] that promotes the higher affinity conformations. The two activated forms are thought to be transient and can revert back to the low affinity conformation after seconds to minutes due to calcium and zinc ions believed to promote closed state and inhibit ligand binding [180,203,212]. At physiological conditions, the coexistence of calcium and magnesium ions yields in integrins existent in all three conformations. The FRET $\alpha_4\beta_1$ LDV domain experiments proved that the Mn^{2+} conformational changes result in the integrin extended only half of its maximum extension. Simultaneously, the divalent cations regulate $\alpha_4\beta_1$ integrins ligand binding affinity and dissociation rate by several orders of magnitude [31]. In parallel manganese cations have also been reported as inducing an active conformational state of $\alpha_{IIb}\beta_3$ [124]). Adding 1 mM Ca^{2+} abolishes RGD specific interactions while 1mM Mn^{2+} promotes them. Simultaneously, EDTA is a potent blocking agent for RGD-integrin interactions [147]. Cell attachment and migration on ECM proteins may be regulated by distinct intracellular signals. For example, endothelial cell migration, on VN requires Ca^{2+} present in medium. This results in a rise in intracellular Ca^{2+} concentration that is hereby available for $\alpha_V\beta_3$ and $\alpha_2\beta_1$ ligation promoting rather migration than attachment. The same experiment proved that on collagen neither cell migration nor attachment were independent on external calcium ions concentration. β_1 integrin subunit on endothelial cells was proven to be a flow direction sensor as it was activated by single direction laminar flow but not by bidirectional movements [220]. However, the new approach implies that integrins constantly and continuously change their conformation. Affinity can be increased by mechanical tension stabilizing an open conformation. In case of $\alpha_5\beta_1$, it is proven that the mechanical tension engages synergy site of FN binding and thereby FAK phosphorylation [62]. Among many roles of integrins family members there are some key tasks:

- Providing cells with external, mechanical support by binding the ECM molecules: fibronectin, vitronectin, laminin, collagens etc.
- ECM connection to actin cytoskeleton stabilization
- Assuring the balance between inside-out and outside-in signalling by acting as bidirectional signal transducers

- Allowing and enhancing adhesion between cells
- Regulation of cells proliferation, wound healing and tumour progression
- Mechanosensing and mechanotransduction.

Integrins are molecules responsible for multiple cellular functions. For example ligation of integrins $\alpha_V\beta_3$ and $\alpha_2\beta_1$ with Ca^{2+} ions results in different intracellular signalling events as described before [114]. Another example can be glioblastoma cells migration that was inhibited highly selectively by $\alpha_5\beta_1$ integrin antagonists but increased by $\alpha_V\beta_3$ and $\alpha_V\beta_5$ antagonists [161]. Integrins $\alpha_V\beta_1$ and $\alpha_V\beta_6$ actively participate in epithelial-mesenchymal transition-like change in breast cancer cells [104]. The properties of cellular adhesion were widely studied on the example of fibroblasts adhesion to fibronectin pictured also in Fig 3. After initial rapid myosin motor driven spreading stage, the necessity of adhesion sites development occurs [165]. Mechanical spreading force generation requires link between ECM proteins and integrins through talin, which activates integrin binding to matrix [15]. Subsequent phase of force transition to actin cytoskeleton requires stabilization of the link between β_1 and β_3 integrins and cytoskeleton [148].

Cells response depends equally on the inside-out and outside-in signal transduction mechanisms. Focal adhesion kinase[2] (FAK) phosphorylation, microtubules and myosins are believed to be incorporated in this process. However, the key mechanism remains unclear but connected with complex cross-talk between GTP [3] and Ca^{2+} levels, phosphorylation and proteolysis [11]. The cyclic hydrodynamic pressure caused the increase in integrin α_5 expression and FAK phosphorylation, which plays crucial role in integrin α_5 signalling whereas not in α_1, α_3, α_4, α_V, β_1 and β_3 integrins. Additionally, the level of p-FAK[4] was lowered and abolished proliferation of bladder smooth muscle cells due to the α_5 integrin inhibition [211]. On the other hand β_1 integrin is believed to control vasoregulation, serving as a smooth muscle cells mechanosensor. This assumption is justified by activation of

[2]focal adhesion associated protein kinase, which phosphorylation is inevitable for adhesion and cells spreading.

[3]guanosine-5'-triphosphate, an agent responsible for phosphate transport(phosphorylation) and hence energy transfer.

[4]phosphorylated FAK

integrins in presence of peptides that regulate Ca^{2+} channels conformation on cell membrane and hence smooth muscle cells (SMCs) contraction and vasoconstriction[5] triggering [131, 219].

For example in melanoma cells it is proven that $\alpha_V\beta_3$, capable of binding RGD motif of either fibrinogen, VN, OPN or FN, expression correlate with invasiveness and malignancy level [130]. The β_1 integrin expression correlates with increased elasticity parameter of the surrounding ECM, invasiveness, and metastasis of hepatocellular cells carcinoma in patients with cirrhosis [231]. Moreover, the experiment on hepatocellular carcinoma cells performed on the substrates of distinct elasticity suggested that β_1 integrins are the key mechanosensors transdusing signals into the metastatic cells. In the same scrutiny β_3 expression could not be measured successfully and α_4 and β_5 were expressed on the level below detectable. β_1 and α_V integrins expression levels changed significantly for the samples cultured on the substrates of distinct Young's moduli while the change in α_5 subunit expression was mainly correlated with malignancy progress [47]. Another metastasis promoting process associated with integrins is FAK complex activation involving its substrate c-Src[6]. It translates in raised cell motility, survival and cycle progression. The role of integrins in described process is to recruit and activate aforementioned tyrosine kinases in focal adhesions [134]. The important factor is that that FAK and c-Src require simultaneous activation. Neither activation of FAK nor of c-Src alone correlates with breast carcinoma malignant transformation [127]. This leads to the conclusion that enhanced adhesion of tumour cells to the ECM takes important part in metastasis processes.

2.3 Syndecan-1 and -4, their significance in cancer cells research and interactions with integrins

The family of syndecan receptor consists of four members numbered from 1 to 4 all being type I (transmembrane) integral receptors binding to variety of

[5] blood vessels contraction

[6] proto-oncogene tyrosine-protein kinase Src that phosphorylates specific tyrosine residues in other tyrosine kinases.

ligands including the fibronectin [175], collagen types I, III, and V [109], and thrombospondin [191]. Syndecan-1 was first cloned in 1989 and named syndecan after a Greek word *syndein* - to bind together. In the following years the structure of three more syndecans was described. Each syndecan consists of three functionally distinct domains: an extracellular, transmembrane and cytoplasmic domain [156, 157]. The schematic representation of a syndecan structure is presented in the Fig. 3. The cytosolic domain of syndecans, conserved in all the family members, consists of three functionally distinct regions (C1, V, C2 subdomains) and is believed to be responsible for inside-out signalling. C1 is responsible for clustering syndecans in dimers and oligomers and hence for regulation of ligands binding affinity. C2 domain conserved EFYA sequence is responsible for interactions with cytoskeleton through a so called PDZ (PSD-95, discs large, ZO1) domain [76] and the Ca^{2+}/calmodulin-associated Ser/Thr kinase (CASK) [89, 90]. These short sequences conserved in all the syndecans indirectly participate in intracellular signalling and transcriptional control. Cytoplasmatic tail phosphorylation affects regulatory mechanisms such as syndecans binding to its signalling partners. Syndecan-1 cytoplasmatic domain co-sediments with F-actin [158] and colocalizes in polarized NMuMG cells with the actin cytoskeleton [157]. The V region of cytoplasmatic domain varies between distinct syndecans. For example in SDC-4, it is responsible for antiparallel dimerization of syndecan heterodimers [182] together with the main dimerization transmembrane domain. Syndecan-4 monomers dimerize or polymerize creating a zone of negative charge on the membrane and thus facilitate interactions with positively charged ligands [72]. It also controls channels responsible for cytosolic calcium equilibrium [74]. The extracellular domain of each syndecan contains cell-binding domain and distinct heparan binding sites near the COOH terminus, which can covalently bind linear chains of heparan sulphate (HS) or chondroitin sulphate (CS), making it a hybrid proteoglycan. HS chains are integral parts of fibronectin complexes and signalling complexes between distinct growth factors, and their respective receptors. Each of the syndecans contains HS, while syndecan-l and syndecan-3 also contain CS [42,156]. Each single SDC molecule have multiple attachment sites and thus can develop several

interactions with ECM molecules stabilizing cells adhesion in a highly efficient manner. The number of chondroitin sulphate chains differs in epithelial cells due to distinct posttranslational modifications in response to changing from single to multiple layer organization [172]. The ectodomain of syndecans on NMuMG cells is proven to undergo proteolytic shredding (i.e. detachment from cell surface glycosaminoglycan rich fragment) in response to cells rounding and trypsynization that cause cells losing their polarity [98, 176, 213]. The heparan and chondroitin sulphate concentrations change in response to TGF-β [160], altogether with the shedding (loss of CS and HS) mechanism suggest that every glycosaminoglycan binding site may vary its affinity in response to environmental conditions and result in distinct cell behaviour. The described mechanism provides the opportunity to reduce the stability of the cell-matrix linkage and allow cells to detach from the substrate. For example, syndecan-1 shedding protects against tissue damage during the neutrophilic inflammatory response by modulating the availability of certain chemokines [82]. The role of SDCs in mammalian cells can be divided in seven main categories:

- Providing cells with external, mechanical support by binding the ECM molecules: fibronectin, collagens etc.
- ECM connection stabilization vs. destabilization balance
- Enhancing adhesion between cells
- The other receptors control in response to growth factors, fibronectin, antithrombin etc. stimulation - migration regulation
- Regulation of cells proliferation and tumour progression
- Mechanotransduction
- Playing the key role in integrin turnover.

The choice of syndecan-1 was dictated by its presence in virtually all mature epithelial tissues [81], in embryonic and undifferentiated mesenchymal cells [204, 205] and its great significance in a variety of tumours. Lower expression of SDC-1 was described in squamous cell carcinoma [8] colorectal and prostate carcinomas [35, 145]

resulting in the assumption that it could be a parameter utilized as a prognostic marker and to adjust therapy aggressiveness to patients' needs. The membrane SDC-1 expression level was inversely correlated with tumour progression in primary nonmuscle-invasive bladder cancer [107]. Importantly, the comparative scrutiny of bladder cancer syndecan-1 ectodomain concentrations in serum and in cancerous cells revealed that raise in serum SDC-1 correlates with syndecan shedding from the surface of malignant cells [193]. That would suggest specific role and hence applicability as a prognostic marker of stromal and membrane syndecan-1 in metastasis. Moreover, SDC-1 deficient NMuMG cells exhibit distinct morphologies depending on syndecan-1 concentrations. The clones that express more than 45% of normal SDC-1 levels cluster as expected from closely adherent epithelia, while over 90% reduction of membrane SDC-1 results in individual fusiform (i.e. fibroblastic type) cells that overlap each other [103, 176]. Syndecan-1 undergoes shredding upon the heparanase activity causing heparane sulphate fragments release from the membrane. Since intact HS acts as a physical barrier for ECM preventing tumorigenesis and migration, shedding can be a marker of cancer progression. Co-localization of SDC-1 and heparanase in the cells membrane region promotes multiple myeloma in bone marrow and breast cancer progression [225], in-vivo angiogenesis melanoma cells migration but had no impact on endothelioma cells behaviour [138]. This occurs due to heparanase role in growth factors and chemokines release and metastais progression in response to release of HS oligomers [138]. The HS chains have more complex function in cells. They also change conformation upon contact with divalent ions and together with heparin modify fibroblast growth factor and its receptor in the presence of either Ca^{2+} or Mg^{2+} [101]. Syndecan-4 is expressed ubiquitously and appeared to be significantly over-expressed in metastatic melanoma cells [140] that also justifies its possible significance in this research. Syndecan-4 acts as either a receptor or a co-receptor for variety of heparan binding growth factors and hence reorganize their distribution in cells environment. It modulates the effects of distinct extracellular signalling and adhesion molecules, which translates into regulation of attachment and hence adhesion. The proteoglycans spacial rearrangement has a crucial role in the signal transduction. Altogether, the broad variety

of interactions lead to SDC-4 documented participation in physiological processes including inflammation tuning, protection from endotoxic shock [95], blood pressure regulation [146], immunosupression [33]. Moreover, SDC-4 is an acclaimed key contributor to cell–ECM junction formation, and hence a prominent adhesion and migration regulator [135]. This yielded in the special interest in SDC-4 signalling pathways. Both syndecan 1 and 4 knockdown coincides with melanoma metastatic potential lowering in patients [140]. SDC-1 and SDC-4 appeared crucial also for the process of wound healing [68]. According to a Western-blot scrutiny conducted on bladder sections from patients, expression patterns of all four syndecans were statistically indistinguishable in proper-looking tissue (non-malignant), cancerous samples and controls. However, RT-PCR of SDC-1, -2 and -3 mRNA showed statistically significant raise in malignant tissues while SDC-4 mRNA difference was not significant [132]. This suggest that syndecans role in bladder cancer is more complex an should be examined with a different technique than simple expression assays. Due to practical reasons and the thesis volume limitations the syndecan-2 and syndecan-3 (N-syndecan), which are predominantly expressed in respectively neural and foetal tissues and the developing long bones proliferative zone, were not studied in this work. However, SDC-2 was found in the microvasculature of gliomas and takes part in angiogenesis by impacting endothelial cells which implies its significance in some types of cancers [57]. SDC-2 and -3 are also present together with SDC-1 and -4 in bladder tissue sections from both healthy and bladder cancer patients [132].

2.4 Synergistic control of cell adhesion by integrins and syndecans

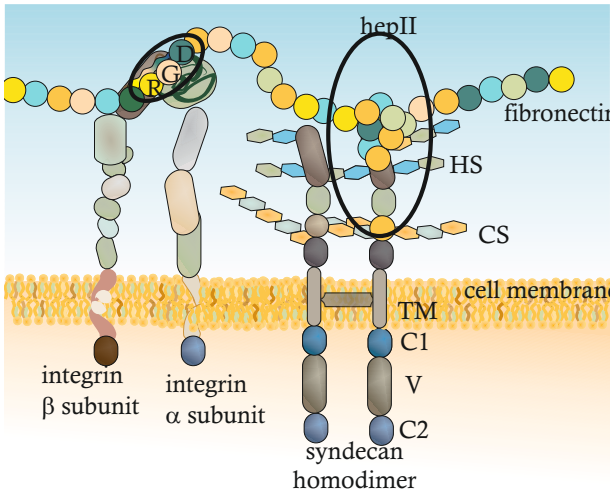

Figure 3: Scheme of an example of $\alpha_5\beta_1$ integrin and syndecan-1 binding to fibronectins distinct fragments. Importantly, syndecan-1 and -4 HS chains can also participate in complexes with integrins thus altering their function.

The cell can contain both integrins and syndecans simultaneously in their membranes. The choice of syndecan-1 and -4 as experimental models was dictaded not only by their association with metastasis but also by their association with integrins through their HS chains. Both syndecans and the β-chain of integrins contain small cytoplasmic domains of 34 - 47 amino acids [4, 197] that associate with the actin cytoskeleton as a result of the ECM ligands binding [26, 41, 157]. There are no visible similarities in the composition and structure of those domains suggesting their distinct functions. The syndecans are homodimers and integrins are heterodimers with each oligomer much larger than the single polypeptide of syndecan. Moreover, the presence of multiple HS and CS chains in each syndecan molecule could explain the three orders of magnitude greater affinity of syndecan than of integrin for collagen [19, 109]. Providing a similar number of membrane receptors, this suggests a higher physical stability of complexes including SDCs. The interactions with both the RGD fragment and heparin-binding fibronectin domain are

necessary for fully establishing of focal contacts and cytoskeletal organization of fibroblasts [217]. It is worth to notice that focal contacts do not form on substrates where the two domains are isolated [97]. That would suggest cooperation between integrins and syndecans to be possible only when binding the same ligand [7]. The claim is supported by the fact that HS causes a conformational change in native plasma fibronectin [143]. In 1988 Saunders and Bernfield proposed that "syndecan stabilizes cell interactions with fibronectin-containing matrices, whereas the integrins are involved in initial recognition and perhaps cell migration over such matrices" [175]. The thesis that seems to be confirmed by modern research. While cell spreading on fibronectin, integrin $\alpha_5\beta_1$ colocalize with SDC-4 in focal complexes at the leading edge of fibroblast movement [218]. Importantly syndecans not only colocalize with integrins. The extracellular SDCs -2 and -4 cell-binding domain also associates β_1 integrin and mediates mesenchymal cell adhesion [214]. SDC-1 ectodomain directly cooperates with $\alpha_V\beta_3$ integrin in the formation of a signalling complex that is negatively regulated by β_1 integrins [9]. The participation of both receptors is necessary to form a fully established vinculin-based adhesion [7, 217], and the disruption of SDC-4 is not lethal but significantly slows down the process of wound healing [51]. Lately proposed model assumes for syndecan-integrin cooperation being especially crucial for biological processes requiring directional migration regulation including angiogenesis and metastasis. Syndecan-4 can cause $\alpha_5\beta_1$ integrin endocytosis or activation depending on the type of protein kinase involved [135]. Syndecans are highly prominsing therapeutic targets of not yet fully understood mechanism. Another interplay may occur because syndecan-4 controls channels responsible for cytosolic calcium equilibrium [74] that may possibly have an impact on integrins MIDAS.

2.5 The development of force spectroscopy methods in cancerous cells and ECM proteins assessment

Atomic force microscopy is a unique technique providing an information about the topography and mechanical properties of biological material with the nanometre resolution enabling also maintenance of the physiological conditions. In ad-

dition, AFM is suitable to work in force spectroscopy mode. The method is introduced in chapter 3.1. Single molecule force spectroscopy (SCFS) is an AFM mode of operation executed by attaching a ligand to an AFM probe. A-C in the Fig. 4 are examples of single molecule force spectroscopy (SMFS) while D represents single cell force spectroscopy. The uniqueness of AFM based methods is their versatility in assessment of living cells and specific receptors close to their native condition and the capability to compare the results on isolated systems [84] with the biological samples of distinct level of complication (living single cells in this work, possibly tissues in further experiments). The special feature of living cells is that they express receptors in their native condition which can be altered by the cells themselves.

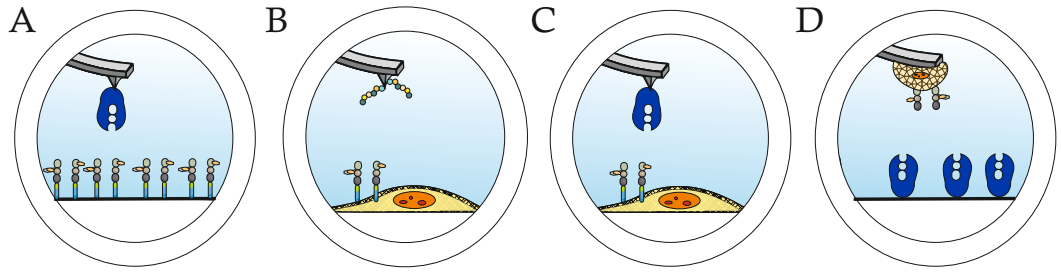

Figure 4: The possible modes of AFM spectroscopy operation: A. isolated system: a ligand or antibody decorated probe collecting curves on a functionalized flat, rigid surface, B. probing of receptors on the living cells with specific or semi-specific ligand on the probe tip, C. probing of receptors on the living cells with a highly specific antibody covered probe tip, D. probing with a cell attached to a cantilever against a surface covered with immobilized molecules of interest.

Dynamic force spectroscopy (DFS) is a SMFS based experimental procedure when a functionalized tip is repeatedly brought into contact with sample and subsequently retracted with different velocities (resulting in different loading rates) in order to obtain adhesion bond rupture force values. They are used to calculate the energy landscape parameters of a specific molecular interaction. It allows extracting deadhesion force values between the sample and substrate of choice. DFS is a type of single molecule force spectroscopy which allows quantifying ligand-

binding free-energy landscape. Thus, it is being used to probe the unbinding force, correspondent lifetime, and chemical reaction rate of single molecules' complex (wider discussed in chapter 3.1.4). The first historical study on specific unbinding using AFM was executed and published by Florin et al. in 1994 [58]. They have measured the unbinding force of avidin-biotin complex. The measurement was performed with commercially available AFM tips functionalized with avidin against agarose beads covered with biotin. Soon after that, the DFS experiments on avidin-biotin and streptavidin-biotin unbinding over the range of six orders of magnitude loading rates yielded in the result suggesting multiple barrier crossing mechanism. As DFS data are collected with a range of loading rates, they can suit to calculate the unbinding energy landscape parameters according to a given theoretical model. The described technique was used to calculate the energy landscape, the bond length of avidin-streptavidin [137], and to confirm molecular simulations based on historically the oldest Bell-Evans model [133]. Hinterdorfer et al. measured adhesion force of the human serum albumin (HSA) fragment with its antibody anti-HSA fragment complex [85]. Single molecule force spectroscopy was also applied in examining RGD containing peptide interaction with Cacao-2 colon adenocarcinoma cells surface. The scrutiny was performed with just one velocity, but included testing the impact of intercellular kinases, Ca^{2+} and Mg^{2+} for GRGDSP and RGE maximum unbinding force [147]. Another example may be a panel of single molecule experiments with different antimicrobial peptides against HeLa cells membrane. The experiment suggested the dependence of unbinding force between α-helical peptides and cancer cells was mainly in hydrophobicity [178]. The carbohydrates and lectins unbinding forces were studied with DFS technique on HeLa cancer and MDCK normal cells. The unbinding kinetics studies show that the carbohydrate–lectin complex is less stable in cancer cells in comparison to normal cells [232]. An interesting, novel approach was proposed lately. SCFS measurements of RGD containing molecules and integrin receptors on the surface of intact cells vary between 30 pN and 140 pN depending on the different loading rates, peptides, and experimental procedures applied [117, 147, 192]).

DFS was applied for example in G protein–coupled receptors imaging combined

with energy landscape parameters calculation. However, the sample was an artificial membrane with receptors reconstituted in lipoproteosomes, not living cells [2]. N-cadherin antibody unbinding properties were examined using DFS method on HCV29 and T24 cells incorporated in this work. The study revealed N-cadherin antibody most probable unbinding force to be over twice higher for transitional carcinoma than for non-malignant cells within the loading rate ranging from 2500 pN/s to 6600 pN/s. Simultaneously, almost no dependency of the unbinding force on applied loading rate was observed [119]. Another DFS measurements were performed on distinct melanoma lines with the use of concanavalin A functionalized probe [185] and with gonadotropin-releasing hormone Pseudomonas aeruginosa exotoxin 40 against the gonadotropin-releasing hormone on the surface of HeLa cells [228]. An important work was performed with DFS on artificial biomembranes with immobilized $\alpha_5\beta_1$ integrin against GRGDSP peptide in the range of loading rates significantly exceeding the range presented in this work (1-305 nN/s). The use of three different spring constants of cantilevers allowed to obtain data revealing two activation barriers with a border value at 59 nN/s loading rate. The low strength regime with forces around 20 pN corresponds to outer barrier at 2.77 nm bond length and a dissociation rate in the absence of force equal to 0.015 s^{-1} [110]. Wojcikiewicz et. al. performed an experiment comparing single cell and single molecule force experiments with 3A9 lymphoblast-like cell and ICAM-1 molecule approaching to provide an insight in the mechanism of cell adhesion. Moreover, they described the thermodynamic separation model of the complex and proposed the description of the mechanism on a cellular scale [216]. A very important study was performed with the CGG**RGD**S FNIII fragment and entire human FN conjugated to APTES coated AFM probes with malemide-PEG, malemide-PEG-NHS and PEG crosslinkers. Such prepared probes were used to perform SMFS experiments on the surface of *E. Coli* and DFS on CgsA covered substrate. The specificity of measurements was confirmed by a blocking experiment with the RGD containing peptide and revealed higher binding probabilities of short CGG**RGD**S sequence rather entire fibronectin. Then the Single Cell Force Spectroscopy (SCFS) experiment with either wild type, CgsA positive or negative

E. Coli on fibronectin was performed. Since CgsA is a bacteria pilli mediating protein, the research aimed to explain the curli mediate FN adhesion of bacteria [141]. Another experiment incorporating fibronectin was conducted on the isolated system of FN versus its monoclonal antibody. The DFS results fitted with Bell-Evans model (chapter 3.3) suggest the existence of the energy barriers to be overcame while complex unbinding. The border between barriers was observed at loading rate value slightly below 10^4 pN/s [112]. The other approach to interpret DFS data was presented on the example of experiment with cantilevers constructed of a micropipette and a sialyl Lewis^x covered bead brought into contact with its ligand (E-selectin) covered fibres. After fibre spring constant calibration, the sphere and the bead positions were traced as they were brought into contact and retracted in order to deconvolute the forces acting in the system. The specificity of experiment was confirmed with antibody interaction blocking, E-selectin chimera binding and replacement of E-selectin with bovine serum albumin. The experimental data were enriched with Monte Carlo simulations in accordance with Bell-Evans model and with hydrodynamic drag compensation. The DFS result of unbinding forces plotted against the loading rate (in the similar range as this study) was fitted with three separate straight lines. The authors point out that the unbinding force can be a good estimation for bond breaking force only for higher loading rates, thus they did not take in account loading rates lower than 200 pN/s in a system where off-rate is assumed approximately 1 s^{-1}. They argument this decision by the claim that in the lower range of loading rates the slope of the Bell fit function decreases to zero [202]. Instead of AFM, other techniques may be applied in an unbinding force spectroscopy measurements i.e. optical traps, tweezers etc. The $\alpha_{IIb}\beta_3$ integrin-fibrinogen complex characteristic for platelets underwent a series of thorough examination providing insight in platelet adhesion and aggregation in blood flow. The experiment with the use of constant pulling force revealed existence of the weaker and the stronger binding states, stronger of which characterized with around 8 k_BT unbinding energy for the case of 50 pN constant unbinding force. Additionally, the unbinding energy raised around 50% in the presence of Mn^{2+}. The authors hypothesized that they can correspond to two distinct interconvertible

functional states of the $\alpha_{IIb}\beta_3$ molecule [123, 124].

Single cell force spectroscopy is a method suitable to quantify the binding force of adhesion of single molecular complexes in living cells with the force resolution of several piconewtons. It can also provide information about work of adhesion of functionalized probe on the sample surface and for example length of a complex bond. Typically, SCFS incorporates AFM probe functionalized with specific ligand present on a tip against certain surface (for example living cell membrane). This can provide information about local binding forces of the assessed complex. Along with that, relatively new approach appeared to be very promising: instead of a silicon nitride tip there can be a living cell attached to the AFM cantilever so that it suit as an AFM spherical probe. Assessment is conducted against stiff surface or polymeric substrate of given elasticity functionalized with molecules of interest. Described approach offers two advantages. Namely, the result carries information about unbinding events averaged on the surface of a cell, still keeping possibility to extract the force of a single bond rupture. There is a possibility of surface rigidity selection so that it better mimics native conditions. There is a number of various studies conducted using SCFS against living cells surface [200, 229].

In 2003 Feiya Li et. al. published the results of interaction force measurements between $\alpha_5\beta_1$ integrin and fibronectin. The authors attached K562 chronic myelogenous leukaemia cells, which express the $\alpha_5\beta_1$ integrin but no other FN receptors [83], to a tipless cantilever and probed it against a rigid surface of culture dish functionalized with either human plasma fibronectin FN7-10 or FN7-10 with deleted RGD sequence, responsible for integrin-fibronectin complex binding. Atomic force microscope enabled application of force in a range of 100-500 pN exerted by cantilever, given contact duration, and probing velocity. Acquired data allowed calculation of detachment energy, unbinding probability and rupture force scrutiny under certain loading rates. The specificity of measurements was verified by a significant reduction in the frequency of unbinding events due to anti-α_5 antibody presence whereas integrin activation occurred due to addition of TS2/16 activating monoclonal antibody [122]. Described publication proved specific interaction between $\alpha_5\beta_1$ integrin and fibronectin. Another recent work from Ediz

Sariisik et al. focus on distinction between membrane- and cytoskeleton-anchored cancerous cells interactions. Prostate cancer cell line PC3 was coupled to the tipless cantilever. Measurements conducted with SCFS against rigid surface functionalized with collagen-1 and mesenchymal stem cell line SCP1 proved that β_1 integrin specific interactions are mainly anchored to the cytoskeleton. On the contrary, non-specific interactions are membrane dependent [174]. This research included mainly scrutiny of adhesive properties of $\alpha_1\beta_1$ and $\alpha_2\beta_1$ integrins, which GFOGER sequence binds to collagen and laminin [52]. While rigid surface functionalized with collagen was used to prove the assumptions, bovine serum albumin coated rigid surface stood for negative control. The versatility of SCFS in examining different aspects of cell adhesion was proven on the example of Madin-Darby canine kidney (MDCK) cells adhesion to collagen I normally mediated by integrins. Adhesion enhancement observed in the cells with depleted galectin-3 resulted in postulate that galectin-3 influences integrin-mediated adhesion complex formation [63,64]. However, not all the DFS techniques applied in protein-peptide interactions scrutiny require AFM. The optical tweezers DFS experiment incorporating latex beads covered with covalently attached dextran and cyclic RGDFK or fibrinogen γC-dodecapeptide (H12) on the platlet integrin $\alpha_{IIb}\beta_3$, suited to prove higher stability of RGDFK-$\alpha_{IIb}\beta_3$ in comparison to H12-$\alpha_{IIb}\beta_3$ complex [190].

3 The principles of Dynamic Force Spectroscopy

3.1 Atomic Force Microscopy method

Atomic Force Microscope (AFM) is a type of scanning probe microscope (SPM). Its main elements are:

- scanning and positioning system in three perpendicular directions
- elastic lever with a usually sharp probe
- lever deflection system

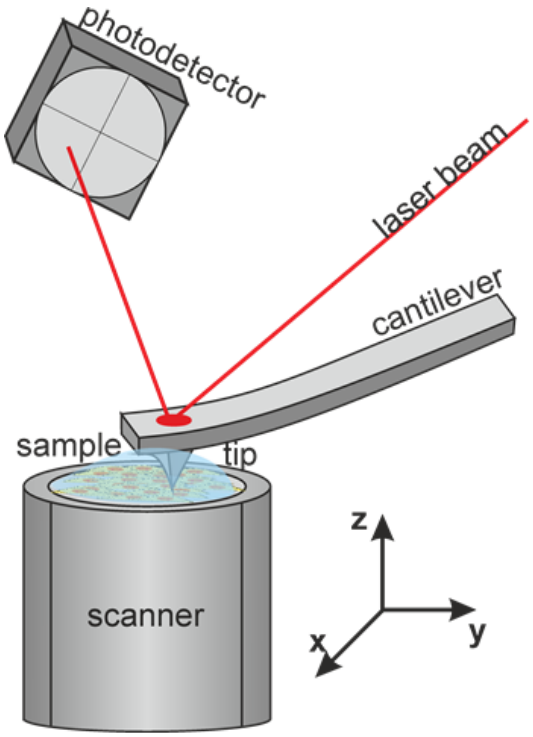

Figure 5: The construction scheme of the most common atomic force microscope capable to work with samples in liquid. The red line symbolizes laser beam reflected from the upper surface of cantilever above the tip position to the photodetector. The movement up and down is designated in z axis while xy plane holds the sample surface planar movements both executed with either step motors (less precise) or piezoelectric tube (highly precise).

In addition, AFM can be equipped with a system enabling work in liquid conditions, which are highly recommended for biological samples. In the majority of set-ups the positioning system consists of a piezoelectric scanner, step motors and electronic controller. The laser, the set of mirrors, and position photodiode detector suit as a detection system for the probe that is mounted on a cantilever on a holder. The scheme of a typical AFM is presented in the Fig. 5 while Fig. 6 presents a top view of sample containing cells on a surface of a Petri dish and AFM probe in the liquid conditions.

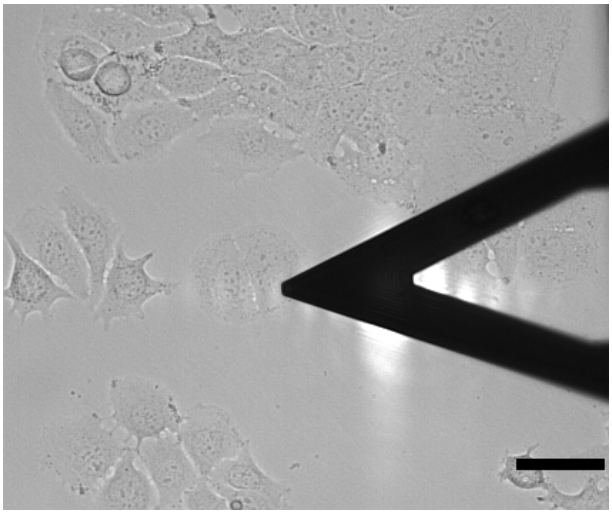

Figure 6: The 20x optical microscope preview of measurement in liquid conditions. The sample consists of living HT1376 cells seeded on a Petri dish for 48 h in EMEM medium enriched with 10% FBS. The black triangular lever is a 200 μm long OMCL TR400 PSA-1 cantilever with a positioning laser spot visible. The AFM tip present on the bottom side of a cantilever tip remains invisible. The scale bar represents 50 μm.

3.1.1 AFM operating principles

An AFM probe mounted at the very end of a cantilever (known also as microlever) is being moved over a sample. The cantilever deflection detection system senses forces present between a probe and a surface while they are in close proximity. Forces involved in the process may be either repulsive or attractive depending on the interaction type defined by the probe material, the surface characteristics and the distance between atoms of tip and sample surface. As it was initially introduced in 1986 [12], the device was applied for surface imaging with high spacial resolution. In such a mode it could provide high resolution topography of a sample by scanning line by line. However, replacing the continuous scanning in horizontal direction with collecting a set of single points vertically suited as a base for the force spectroscopy mode. It enriched the obtained information with sample mechanical properties. The force-distance (FD) curves are being collected in each point, hereby

representing deflection changes as a function of a cantilever separation. While collecting single FD curve, AFM probe approaches a sample in a vertical direction and then retracts. As a result, it provides the mechanical information only from the point of contact with a sample. The cantilever deflection needs to be detected, converted into electrical signal and further processed in order to result in either an image or a set of curves. Additional perk is a possibility to perform measurements in solution and in adjustable temperature. Moreover, AFM enables combination of three dimensional imaging with scrutiny of distinct nanomechanical parameters associated with cellular elasticity and adhesive properties. The most common AFM detection system is a position photodiode detector allowing optical lever method of cantilever deflection and torsion registration thanks to the four photodetecting quadrants. Such a method is widely used due to its simplicity and robustness. It is based on focusing a laser beam on the back side of a cantilever and subsequent measurement of reflected light beam using a position photodiode sensor in two perpendicular axes, thus registering both cantilever deflection and torsion. Among the advantages of the method is that it allows to sense even small changes in cantilever angle because they are translated into a measurably large displacement of the laser spot on the detector.

3.1.2 FD curves

During motion, the cantilever deflection is recorded as a function of relative sample position. Force-distance (FD) curve is a plot of tip-sample interaction forces versus relative tip-sample distance schematically introduced in the Fig. 7. In principle, it means a registration of elastic, flexible lever deflection upon interaction with the surface of an examined sample. FD curves static mode acquisition consists of discrete steps when the sample is displaced along the z axis perpendicular to the sample surface and interaction forces are registered using photodiode (see Fig. 5 in chapter 3.1).

FD curves collection always occurs in two steps: an approach (1-3 in the Fig. 7) and a retract (4-6 in the Fig. 7) of a tip from the examined sample surface. For the adhesion measurements particularly important is the point 5 in Fig. 7. Contact

point (2 in the Fig.7) represents the moment when a probe begins to touch and later indent the sample with the predefined force set-point.

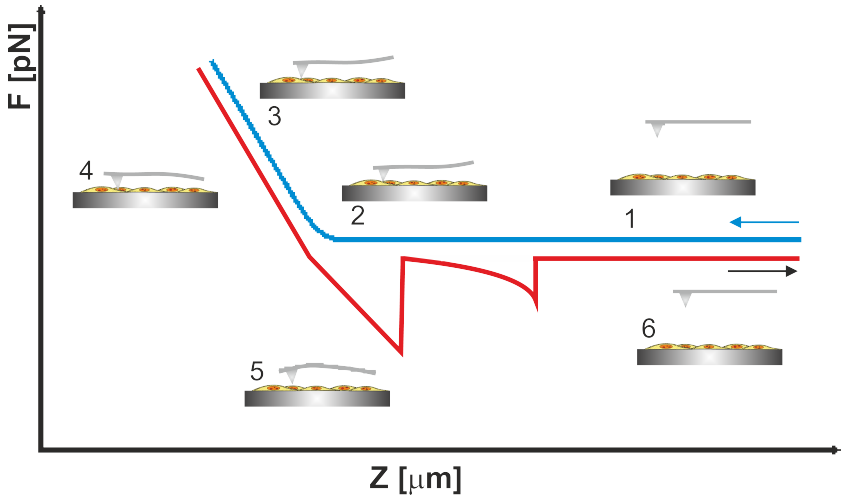

Figure 7: The representation of a typical FD curve with approach and retract segments in blue and red respectively (reprint with permission from my Master thesis). The numbers represent following steps of collecting every single curve: 1. Lack of contact between tip and sample 2. Contact point 3. Indentation of a sample with a tip. 4. Retract of a tip 5. Tip unbinding 6. Lack of contact between tip and sample, cantilever relaxation.

In the Fig. 7 point 5 symbolizes a discontinuity in the retract curve that pictures an unbinding event. It is possible that curve corresponds to a cantilever seemingly coming back to the rest position of no deflection, while there still is a remaining connection between tip and sample. Bonds can be stretched resulting in following specific deadhesion pattern as present in the Fig. 9. Then, the pulling force reaches the rupture value and actual specific unbinding event occurs. There is also a possibility that jump-off-contact and the specific unbinding may overlap resulting in the specific force being invisible due to much larger non-specific adhesion. Thus, minimization of non-specific adhesion is crucial for robustness of performed measurements. However, examination of living cells forces requires the use of culture medium. Therefore, it is better to eliminate FBS from medium which greatly increases the quality of collected curves.

Distance D and the rest position of a cantilever Z differ by a cantilever bending d_c and sample indentation d_i. The only parameter possible to control is Z since the sample deformation and cantilever bending are not known in advance. The scheme of described relations is presented in the Fig. 8. Calibration relates distance the sample moves thanks to the piezo stage deformation to cantilever bending and hence voltage registered on a photodiode. Knowing this, it is possible to relate deformation to applied force according to the Hooke's law. It states that elastic deformation force is proportional to a deformation, where the coefficient is known as a spring constant:

$$F_{Hook} = -k_{cant} z \tag{1}$$

where k_{cant} is a spring constant of a cantilever moving in z direction.

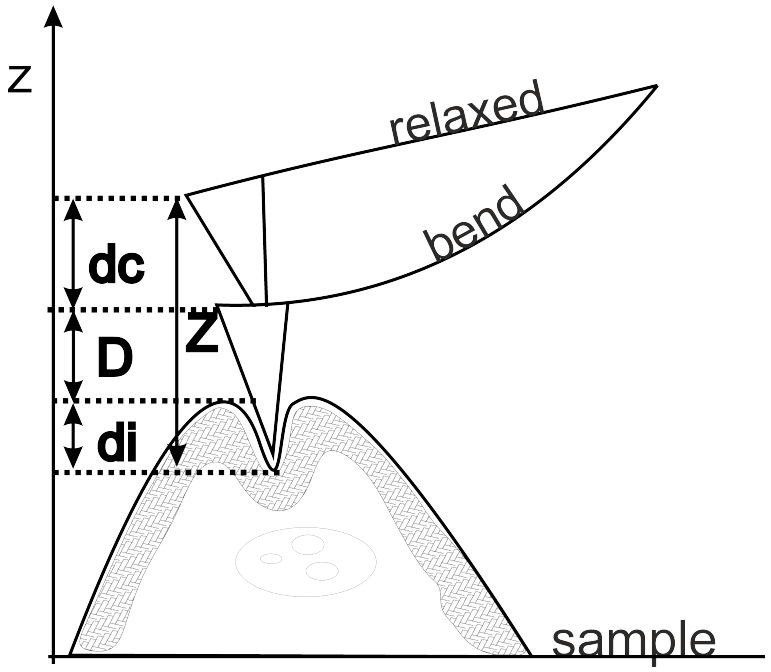

Figure 8: The schematic representation of sample and tip deformation under the mechanical force indenting in the z direction. D states for a distance between probe and a sample, d_i is the depth of indentation and d_c the cantilever bending.

Since we do not have control over number of ligands attached to the probing tip, the complementary molecules may be deposited in different locations dis-

tributed along the slopes of a tip. This leads to the possibility of detachment at different distances, and hence a specific force-displacement curve can present multiple unbinding events with different system constants k_{sys}. In case of probing cell membrane it is also possible to pull the elastic membrane surface contributing in all-over loading rate by lowering the value of k_{sys} and displacing unbinding event toward further parts of retract curve. The analysis of retract FD curves may lead to a set of distinct parameters [23]:

- the specific bond rupture force of single events denoted as unbinding force F_{unb}; it is not trivial to distinguish which event can be taken as specific; in this research I decided on the application of extensive WLC model (as described in 3.5) in order to state whether the event is specific or not;

- the unspecific bond rupture force F_{unsp};

- the work of adhesion W_{adh} - the area between force curve and the threshold denoting zero deflection; this value includes both specific and non-specific adhesion, but under the condition of proper normalization it may suit as a parameter of a general sample adhesion;

- the bond rupture distance, the value dependent on the use of linker, length of examined molecules and the characteristic of sample surface elastic properties;

- the stretching region elasticity and hence the unbinding system force constant;

- the unbinding probability under specific force, i.e. the ratio between the number of specific detachment events and the total number of collected FD curves.

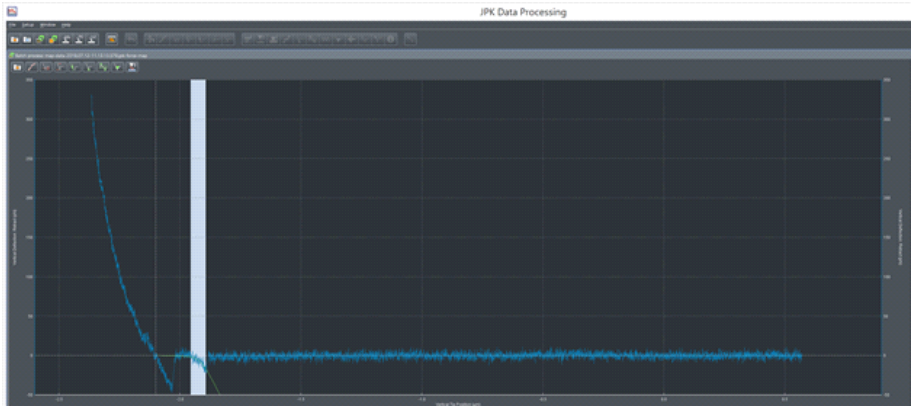

Figure 9: The example of a retract force curve registered during measurement of HCV29 collected within the DFS experiment using Nanowizard 4 AFM head and MabSDC-1 functionalized probe. The part of the curve that corresponds to specific unbinding event is marked in white (approximately 1.9 μm vertical tip position). The unbinding event around 2.1 μm vertical tip position denotes unspecific adhesion bond break. The green curve is fitted according to Extensible Worm-Like-Chaim model further described in the chapter 3.5.

In order to measure specific interactions by the means of AFM, it is required to functionalize the tips by covering them with a molecule of interest as described in 4.1.3. After the jump-off-contact characterized by a certain bond rupture force, the cantilever returns to the rest position of no deflection. Usually to functionalize a tip it is necessary to modify it with a cross-linker first. It allows to immobilize covalently a protein, an amino acid sequence or an antibody of choice on the glass, plastic, mica, or silicon nitride surface. Also gold nanolayer coverage helps to enhance ligand adsorption to the surface. To obtain the best possible results carrying the narrow uncertainty of bonds it is necessary to provide the high specificity of a ligand attached to an AFM probe and a proper linker. For example Hinterdorfer et al. measured adhesion force of the complex human serum albumin (HAS) fragment with its antibody anti-HSA fragment. They introduced 8 nm long polyethylene glycol (PEG) elastic spacer linker to distinguish between specific and non-specific adhesion between functionalized tip and sample. The rupture distance reaches 30 nm calculated as a sum of the lengths of HSA molecule, anti-HSA

antibody and two PEG linkers. The expected distance indicates that individual molecule-molecule bonds have been measured [85]. The method has additional advantage, when ligands are immobilized on the surface, it helps to reorient molecules so that they gain more degrees of freedom and they are more likely to bind to each other. Hence, it rises the binding and the following unbinding events probability. However, in case of transmembrane molecules of living cells, the method loses part of its robustness because of plastic elastic behaviour of the membrane. Since membrane is easily deformable it may take part in the bending length of a complex bond break deforming the corresponding retract curve. Thus, the sum of the combined lengths of spacers and ligands can act only as an indicator of a minimum rupture distance. Moreover, in case of a soft, elastic cell membrane, that can be pulled, also non-specific bonds might get shifted toward the other parts of the curve. Additional obstacle arise when we take in consideration not only the very end of a tip is functionalized and ligand molecules are present at the angled slopes of a tip as well. Then, the binding geometry is more complex and a long elastic spacer rises the risk of both the multiple binding and the bond rupture away from the axis normal to the sample surface. All the cases mentioned above may cause significant discrepancies in FD curves shape resulting in difficulties in theoretical model fitting. Foreseeing such situation, I decided on the use of more basic, simpler method of functionalizing tips with GA and APTES. The choice of the short linker eliminates the necessity to distinguish between specific and non-specific bond rupture events. However, elastic membrane of cells allows the molecules rearrangement in a parallel direction, so that the degrees of freedom number rises and force does not depend strictly on the relative positions. To overcome this obstacle, rather than using a spacer, I decided to distinguish specific from non-specific events basing on the analysis of a fragment of a curve right before the unbinding event using an ex situ algorithm implemented in data analysis. The example of FD curve collected upon the course of experiment is presented in the Fig. 9. The EWLC model and the analysis method are described in chapter 3.5.

3.1.3 Calibration procedures

All types of AFM measurements fundamentally require a robust and standardized force vs. distance calibration procedure to provide comparable results with force resolution getting down to around 5 pN and well characterized shape of force curves. Thus, it is necessary for one of the main purposes of this work i.e. description and optimization of cancerous cells and ECM proteins nano- and micro-mechanical adhesive properties examination. The general set-up calibration relies upon two major parts: piezo stack movement calibration and photodiode position detector calibration. The first of above mentioned is provided by the device producer prior to installation. Hysteresis and creep are piezo actuators artefacts leading to an incorrect determination of displacements. In particular, because of creep, the loading forces in the unloading curve for a given displacement may become bigger and finally overcome those of the loading curve. This phenomenon is called "reverse path effect" and require compensation. There are several methods developed in order to compensate for hysteresis and creep effects. Usually the scanner hysteresis and non-linearity is compensated on the hardware level. Scanner linearization is crucial for the sample movement control that needs to be not only well described but also applied with constant velocity since none of the models used in this work assume the impact of a probe acceleration. Moreover, liquid viscosity depends on the tip velocity which should be as close to constant as possible not to introduce additional errors. The second part of calibration procedure needs to be applied for each probe separately prior to measurement to fulfil the requirement of force vs. cantilever deflection calibration. The photodiode detector sensitivity and the AFM cantilever force constant (spring constant) k_{cant} are characterized prior to each measurement separately, since they are highly dependent on cantilever properties such as dimensions, Young's modulus etc. the position of laser spot at the end of the cantilever and mirror inclination. Even minor differences in any of mentioned values can be crucial for calibration parameters: sensitivity s and cantilever resonant frequency ω_0 [kHz] responsible for cantilever force constant k_{cant} [pN/nm]. The first method of cantilever constant determination is calculation

from known dimensions.

$$k_{cant} = k(E, w, L, h, \rho) \tag{2}$$

It requires knowledge of all cantilever dimensions h, w, L, its density ρ, Young's modulus E and resonant frequency in vacuum ω_{vac}. Young's modulus, density and thickness of a cantilever are difficult to measure directly especially in case of non-homogeneous cantilevers covered with reflective layer on one or both sides. Thus, this method should be qualified rather as approximation than actual determination of k_{cant}. Spring constant can be also measured with a great span of methods including the added mass method known as Cleveland method. It requires a determination of the cantilever fundamental mode resonant frequency as a function of a known mass added to a cantilever [34]. The opinions on whether mass of a range of several tenths of nanograms can be attached firmly enough with just capillary forces or whether method requires glue are divided. Adding glue is invasive for the cantilever and needs to be performed after measurements. Thus, introducing raised risk of cantilever destruction prior to calibration and does not allow full control over force applied to the sample. Another way to determine k_{cant} is the static method of reference cantilever. A reference cantilever of well-known spring constant is mounted upside down. The cantilever of interest needs to be used to obtain FD curve while touching tip-to-tip the reference cantilever. Every discrepancy between relative cantilever tips positions needs to be measured and taken in account to calculate the correction factor. Thus, the last method is slightly inconvenient and introduce additional cost of referential cantilevers. The most common method *in situ* and the one used while preparing this thesis, is the optical lever technique. It allows users to calibrate the probes' spring constants independently and routinely during DFS measurements. The laser light reflected from a cantilever freely oscillating in thermal equilibrium with its environment is registered by the photosensitive diode detector used also during the experimental procedure. Hence we need to keep in mind $\frac{dz(L)}{dx}$, not z(L), is measured in this technique. Registered thermal noise spectrum signal undergoes fast Fourier transform (FFT) from the domain of displacements to the domain of frequencies and following data analysis. There are two variants of optical lever method: contact based calibration (CBC)

and contact free calibration (CFC) briefly described below.

Contact based calibration (CBC) consists of two main steps. Initially, the sensitivity s of a cantilever is obtained from FD curve on a rigid substrate that can be approximated as non-deformable. It allows to determine how much does cantilever deflect upon a known change in current registered by a photosensitive diode detector. Namely, it translates difference in volts into height change in nanometers. After the contact point, the repulsive regime of interaction between a probe and a surface starts to dominate; the deflection of a tip rises linearly upon change of the surface relative position. Properly calibrated set-up can suit to sense the deflection of a cantilever pressed against a rigid surface as equal to sample height difference applied by piezo actuators. The value of sensitivity differs depending on the cantilever type, but also any displacement of a cantilever, laser spot position, mirror inclination angle, or medium that can cause a shift in photodetector sensitivity. The s value is a slope of a linear fit to the fragment of repulsive part of calibration curve. There were significant discrepancies of up to 10% in s value reported depending on a range on a calibration curve taken for the fitting procedure [177]. Thus, it is strongly advised to always set the same off-set in volts when obtaining a calibration curve and fit the same part of the curve every single time. When detector sensitivity is known, the force constant needs to be determined.

If we take in consideration rectangular cantilever of length L, width w, thickness h and Young's modulus E, then spring constant equals:

$$k_{cant} = \frac{0.25Ewh^3}{L^3} \tag{3}$$

Most commonly used cantilevers are composite because they have reflective coating on one or both sides making density of a cantilever difficult to measure experimentally. The physical basis of thermal tune method is the equipartition theorem which states that for each mode of cantilever vibrations separately the thermal equilibrium total energy has a mean value:

$$1/2k < X^2 >= 1/2k_BT, \tag{4}$$

where $< X^2 >$ signifies the time average mean square deflection of the cantilever caused by thermal oscillations, known also as a thermal noise; k_B states for the Boltzmann constant and T is a temperature assumed to be constant in this case. The deflection of cantilever is commonly measured using optical lever technique. Keeping in mind $\frac{dz(L)}{dx}$, not z(L), is measured directly. The relation is [20]:

$$z(L) = \frac{2L}{3}\frac{dz(L)}{dx} \tag{5}$$

When optical lever technique is applied for thermal tune, cantilever is away from the hard surface, so one is interested rather in $\frac{dz(L)}{dx}$. In case of cantilever supported by a hard surface, it is supposed to prevent vibrations and thermal fluctuations should reach zero. Yet there are thermal vibrations remaining in $\frac{dz(L)}{dx}$. Whether a cantilever is supported or not it defines boundary conditions determining the behaviour of a lever. Butt and Jaschke calculated thermal noise taking in consideration all the thermal vibrations' modes that are different when tip is free or supported by easily deformable, soft sample and when it is supported by a hard surface. For the successful calibration, there is a need to know at least one, preferably the basic (fundamental) mode. Upon actual measurements, the conditions depend on the ratio between cantilever spring constant and sample elasticity and are in between the two described model situations. The general assumption states that a cantilever is oscillating freely (in thermal tune) or being supported by for example a sample surface or glass surface during respectively measurement and sensitivity calibration. The liquid damping effects are neglected. Here, cantilevers are taken as harmonic oscillators characterized as multiple modes with at least one end immobilized:

$$\begin{aligned} z = \sum_{i=1}^{\inf} C_i \sin(\omega_i t + \delta_i) \left(\sin\alpha_i + \sinh\alpha_i\right) \left(cos\frac{\alpha_i}{L}x - \cosh\frac{\alpha_i}{L}x\right) - \\ - \left(\cos\alpha_i + \cosh\alpha_i\right) \left(\sin\frac{\alpha_i}{L}x - \sinh\frac{\alpha_i}{L}x\right), \end{aligned} \tag{6}$$

where $\alpha_i^4 = \frac{12\rho\omega_i^2 L^4}{E h_{cant}^2}$ states for a parameter dependent on vibrational modes and whether cantilever in immobilized at one end or both. The i letters represent

distinct modes of vibration. And x is a position along cantilever, ω_i is an angular vibration frequency of a cantilever with L, h_{cant}, dimensions. The eigenmodes of oscillator in described cases differ when cantilever is free on one end or when it is supported by a sample during DFS measurements, hence sensitivity value requires a correction factor kappa:

$$\kappa = \frac{s_{free}}{s_{fixed}} \tag{7}$$

$$x = \kappa d, \tag{8}$$

where d is a displacement. The equation 4 transforms into:

$$k_{cant} = \frac{k_B T}{\kappa^2 < d^2 >} \tag{9}$$

where the mean square displacement $< d^2 >$ multiplied by the square of κ factor replaces $< z^2 >$. $< d^2 >$ can be obtained by averaging over the deflection signal as a function of time. In case of thermal tune calibration it is integrated over a model function fitted to Power Spectral Density (PSD) over a specified bandwidth. PSD is a Fourier transform i.e. the frequency spectrum of vibrations registered by a detector in the domain of time. The natural choice of model function would be simple harmonic oscillator SHO. However, as it appears in liquids where quality factor Q defined as a ratio between energy stored and lost per cycle lowers due to strong damping, the Lorenzian model fits better. In liquids, like water or culture medium both effective mass of a cantilever and damping is increased resulting in low Q, resonant frequency lowering, and broadening of the resonance peak [151]. Another way to define quality factor is a ratio between fundamental mode resonance frequency and half width at half maximum of the peak. The solution of force constant equation changes from simple harmonic oscillator into an approximated spring constant:

$$k_{SHO} = \frac{2 k_B T}{\pi \omega_0 Q A_0^2}, \tag{10}$$

where ω_0 is a resonance frequency and A_0 is a respective amplitude of a Lorenzian

model:

$$k_{Lorenz} = \frac{k_B T}{\frac{c_1}{\sqrt{c_2}}[\frac{\pi}{2} + arctan(\frac{\omega_0}{\sqrt{c_2}})]} \tag{11}$$

The general rule applied here is to fit SHO model to PSD of cantilevers in air and Lorenzian model when calibration was performed in liquid. Calibration can be performed on many different modes requiring different correction factors. Typically fundamental mode of vibrations is used because it raises monotonically over the distance from a clamp.

Contact free calibration (CFC) is based on a method proposed by Sader [168] and later on enhanced with a set of correction factors. While thermal noise method bases on statistical mechanics, Sader method principle relies in fluid dynamics theory. The advantage of this method is its non-invasiveness and application *in situ*. It is especially important in case of the functionalized tips used in DFS and SCFS, where calibration of a cantilever would bring harm to the functionalization and significantly lower the performance. Another perk of the method is that it requires only prior knowledge about plan view dimensions of a cantilever and medium density ρ_m. Elimination of the necessity to know the thickness h of a cantilever, its density and Young's modulus makes it possible to calibrate even very demanding cantilevers in situ when they are mounted in their final operating position. The Sader method incorporate fundamental resonance frequency and Q factor (defined as a ratio between resonant frequency and FTT peak half width at half maximum) of an unloaded cantilever. They are determined from PSD, thermal noise spectra after FFT.

The aim of a method is to determine cantilever sensitivity and its spring constant as related to each other from the cantilever thermal noise spectrum without the necessity of collecting calibration curve. There are conditions that need to be satisfied according to the original procedure (1999):

- rectangular shape of a cantilever,
- length L of a cantilever greatly exceeding its width w (originally $L/w > 5$, later on minimum $L/w > 3$) ,

- quality factor $Q >> 1$ signifying low damping conditions,
- thermal noise spectrum obtained far away from the surface.

In case they are not fulfilled, additional corrections need to be implemented; for example in liquids where Q ≈ 1-5 or in case of another than rectangular shape of a cantilever [171]. Spring constant equals:

$$k = M_e \rho_c w h_{cant} L \omega_{vac}^2 \tag{12}$$

where M_e is a normalized effective mass of a cantilever in liquid, h_{cant} states for cantilever thickness and ρ_c is its density [169]. The disadvantage of initially proposed method was the necessity to measure the fundamental resonant frequency in vacuum ω_{vac}, which posed inconvenience especially in case of functionalized tips. The previous equation can be replaced with a semi-empirical formula:

$$k = 0.1906 \rho_m w^2 L Q \Gamma(\omega_0) \omega_0^2 \tag{13}$$

where ρ_m is a medium density, ω_0 is the fundamental mode resonance frequency of a cantilever and gamma states for hydrodynamic function dependent on ω_0. Nevertheless, this method still requires Q>>1, whilst in water problems arise quality factor equals usually 1-5 because of the viscous environment. Importantly, liquid environment drastically alters thermal noise spectrum.

Laser Doppler vibrometer is one more spring constant calibration method considered a robust referential solution to prove the accuracy of the other methods. Same like Sader and thermal noise methods, it is qualified as a dynamic deflection method. Despite its great disadvantage of not being available in situ in measurements solution and its requirement of laser diffraction vibrometer possession, laser Doppler vibrometer (LDV) can provide user with a series of the independent velocity measurements. Thus, it eliminates problems with tip-sample friction, uncertainty of laser spot positioning, and its finite size that are main sources of sensitivity uncertainty. Because cantilever constant is inversely proportional to the square of displacement in AFM thermal tune measurements, any

laser spot displacement results in twice higher uncertainty. That translates into the crucial impact of well collimated laser placement on cantilevers upper surface allowing precise placement and determination of cantilever velocity. The method measurement was developed on the basis of Brownian motion of the vibrating object in certain fluid environment. The equipartition theorem provides the connection between spring constant and the reverse of mean velocity square on just the same basis like in the thermal noise calibration method. The velocity power spectra obtained are later on fitted with a simple harmonic oscillator function that includes resonant frequency ω_0, quality factor Q and white noise A_{noise}. For the resonance A_0:

$$y(f) = A_{noise} + A_0 \frac{\omega_0^4}{(Q^2\omega^2 - \omega_0^2)^2 + \omega^2\omega_0^2} \tag{14}$$

and

$$k = \omega_0^2 \frac{k_B T}{< v_{cant}^2 >} \tag{15}$$

We obtain:

$$k_{cant} = 2\omega_0 k_B T \cdot \frac{Q}{\pi A} \tag{16}$$

Geometrical correction factors for optical lever methods All the presented methods have both advantages but also pitfalls. There are numerous works on establishing respective coefficients to correct for the angle between cantilever and the surface, recalculate free oscillations of thermal tune into supported cantilever vibrations, viscous liquid damping, different cantilevers geometries([111], [177]). The first phenomenon deserving notice is a distinction between spring constants of a microlever operating in two complementary modes: the static mode when the static deflection is measured upon force applied to a cantilever (obtaining curve for contact calibration and DFS measurement), and the dynamic mode where cantilever respectively either oscillates freely close to its resonance in liquid environment (when thermally calibrated or in non-contact mode). The difference in spring constants of those two modes originates from distinct functions describing cantilevers movements. The spring constant at any point of a cantilever along its length is defined as a second derivative of potential energy with respect

to vibrations amplitude. The correction factor κ was introduced before in equation 7. Numerical results proposed by Sader for the compensation of described phenomenon $\frac{k_{dyn}}{k_{stat}}$ equal 1.035 and 1.072 for BL and TR400 cantilevers respectively. Spring constant determination in viscous liquids i.e. water or medium are slightly cumbersome mainly due to the fact that damping coefficient depends on frequency. Pirzar and Hugel examined three different AFMs calibration procedures including JPK Nanowizard used to obtain data for this thesis. They claim the deviations from true spring constant in viscous environment can reach up to more than 100% [151]. The correction of a cantilever shape poses another obstacle to deal with when trying to determine the actual spring constants of AFM probes. Stark et al. took an effort to calculate a V-shape cantilever thermal noise using the finite element analysis combined with a thermal noise method and managed to obtain the first 10 eigenmodes of vibrating V-shaped cantilever. They compared the eigenmodes of a V-shaped and rectangular cantilever of 1 N/m spring constant. Presented thermomechanical noise of the tip deflection and photodiode signal values ratio equals respectively 0.997 and 0.967. It is advised to divide the values calculated by Stark et. al. by $\sqrt{k}$ to obtain the values for a cantilever of choice. Nevertheless, the ratio remains constant [187]. More extensive analysis of spring constant calibration of arbitrary shape cantilevers upheldby calculations on 12 probes of distinct planar dimensions and heights was published by Sader et al. in 2012. The scrutiny includes Olympus BL-RC-150VB L=100 μm trapezoidal and TR400 L=200 μm V-shape cantilevers applied in this work. The method compliments previously described Contact Free Sader calibration method formulating approximate hydrodynamic function for cantilevers of arbitrary geometry [168]. The standard CFC was proven to work well for rectangular cantilevers of L/w> 3.3 ratio (L/w>3.9 for slightly cleaved levers). The extension of a theory makes it applicable for all the elastic materials thus automatically including height discrepancies, tip placement, arbitrary shape and aspect ratio. The idea relies on the creation of a hydrodynamic function for an arbitrary shaped cantilever [170] under the condition that: the cantilever acts as linearly elastic solid, the energy of vibrating body dissipates in liquid, the lever generated fluid flow is incompressible.

In addition the assumption of small oscillations yields in neglecting all the body and liquid nonlinearities. Taking Q as

$$Q = 2\pi \frac{E_{stored}}{E_{diss}} \tag{17}$$

at $\omega = \omega_0$ where E_{diss} depends on the vibrations amplitude whereas the dynamic spring constant is independent of them. In addition, E_{diss} of each mode depends on ρ and η, geometry, especially length of a lever and the relevant oscillations frequency. Defining dimensionless parameter b:

$$b = \rho L \frac{\omega_0}{\eta} \tag{18}$$

termed inverse Stokes number, Sader introduces the equation for Reynolds number Re as:

$$Re = \rho w^2 \frac{\omega_0}{4\eta} = \frac{w}{2L_0}^2 b \tag{19}$$

where L_0 is a linear dimension length scale of the flow. Then:

$$k_{cant} = \rho w^2 L \Lambda(Re) \omega_0^2 Q. \tag{20}$$

Thus, the equation obtained for arbitrary shape is very similar to the one initially proposed for rectangular cantilevers. Crucial difference is exchange of constant value times $\Gamma(\omega_0))$ with $\Lambda(Re)$, hydrodynamic function dependent on Reynolds number Re of the flow. $\Lambda(Re)$ and $\Gamma(\omega)$ are related to each other by a constant factor. Because the load is caused mainly by hydrodynamic pressure rather than the shear stress, the impact of cantilever height can be neglected even for relatively high probes [18,40]. Thus, it is possible to assume that hydrodynamic function is dependent only on the plane dimensions of an examined cantilever and on its vibrational modes. Final form of Λ(Re) takes shape:

$$\Lambda(Re) = k_{cant}(\rho_w^2 L \omega_0^2 Q) \tag{21}$$

Sader et al. managed to prove the validity of their model thanks to the dependence

of resonant frequency ω_0 and quality factor Q on the surrounding gas pressure. They were changing gas pressure in a chamber thus changing its Re number. The complimentary k_d values were obtained with LDV. The general method is based on once determined $\Lambda(Re)$ function for all cantilevers of the same planar geometry. Once the $\Lambda(Re)$ function is established, there is no need to repeat the procedure.

Hydrodynamic drag correction The viscous friction of liquid environment of surrounding medium introduces another important phenomenon, namely the hydrodynamic drag force that always acts oppositely to the direction of cantilever movement. Therefore, DFS measured force is a sum of actual force and drag force that strongly depends on approach/retract velocity. For low Reynolds number Re<1

$$F_{drag} = \frac{6\pi\eta a_{eff}^2}{h + h_{eff}} v_{eff} \tag{22}$$

where h is a tip-surface separation a_{eff} is an effective tip radius, h_{eff} is an effective tip height, and v_{eff} is a cantilever velocity. However, the impact of tip geometry on the drag force remains unknown, it is easy to estimate an average drag force experimentally. The distance between approach and retract curves is a result of drag forces acting in opposite directions, hence half of the distance between curves can serve to quantify the drag force. According to the equation 22, the force depends linearly on the velocity of an AFM tip movement. The change of force translates into the change of actual force applied by the device to the sample i.e. there is smaller force than assumed especially upon higher velocities i.e. above around 10 μm/s. Moreover, the drag force changes with the tip-sample distance that leads to the effect enhancement upon small tip-surface separations. Another key element that needs to be assured is as linear as possible approach/retract velocity to eliminate tip acceleration effects. The practical hydrodynamic drag correction methods require determination of hydrodynamic force. The procedure includes allowing cantilever to move with different velocities and measuring the of hydrodynamic force for each velocity. Hydrodynamic force acts oppositely to the direction of cantilever movement and is proportional to the movement velocity. The method of drag correction was described in [53, 202].

Calibration methods applied The two possible calibration procedures available for JPK Nanowizard 4 used for AFM measurements include CBC (contact based calibration described in the paragraph 3.1.3) and CFC (contact free calibration described in the paragraph 3.1.3). CBC was invented earlier than CFC and it is based on first calibrating s sensitivity value by obtaining a force distance curve on stiff non-deformable material such as glass or plastic and then calculating resonant frequency basing on thermal fluctuations spectrum. The force constant of cantilevers was estimated using commercially available thermal tune software built in the Nanowizard 4 head JPK software. In case of GRGDTP functionalized triangular OMCLTR400PSA-1 (TR400) cantilevers, the probe calibration included the standard JPK software built-in contact-based calibration procedure. It consists of two steps: sensitivity determination basing on a linear regime of calibration curve on a rigid material and thermal tune spring constant determination. The calibration was performed on the surface of a plastic Petri dish in liquid to minimize the non-linearity and friction originating from capillary forces - an effect typical for calibration in air. This was especially important because of use of very soft cantilevers.The sensitivity s value was measured *in situ* in working medium environment with a consequently maintained value of 2 V offset. Knowing that s takes different values depending on the curve fragment used, the same part of every curve was linearly fitted to obtain the apparent set-up sensitivity expressed in nm/V. This, together with the choice of sharp tip, helps to minimize impact of systematic errors that are impossible to eradicate: non-linearity in piezo and deflection sensor, friction between tip and sample etc. It is proven that averaging several force curves does not improve the calibration accuracy [177]). The deflection calibration error tends to be the major source of the force measurements error [177]. The thermal tune spectrum at zero deflection was collected at least 300 μm away from the surface in measuring medium after a minimum of 40 minutes environment thermal stabilization. Fourier transform of obtained thermal oscillations spectrum suited for subsequent smoothing and SHO fitting resulting in ω_0, Q, A and η_{white} determination. The PSD spectrum region corresponding to the first oscillation mode

was chosen manually. The final value of cantilever spring constant:

$$k_{cant} = 0.817 \frac{2k_B T}{\pi A \omega_0 Q} \tag{23}$$

where an amplitude A, a resonant frequency ω_0 and a quality factor Q are the result of PSD numerical fitting [201]. All the BioLever cantilevers were calibrated using contact-free calibration procedure (JPK) in measuring medium in thermal equilibrium after at least 20 minutes of stabilization according to Sader calibration procedure as described in chapter 3.1.3. The environment of 25°C to 30°C translated in an approximate water density equal 996 kg/m^3 - 997 kg/m^3 and a viscosity 0.79 - 0.89 Pa·s. In each case a standard correction factor of 0.817 was applied (JPK manual available for users). Each BL cantilevers' plane dimensions were assumed 100 μm x 30 μm as claimed by the manufacturer. After an experiment the data were analysed and recalibrated. The cantilever recalibration based on the Sader method [168, 169] in an Internet applet [167]. The BL microlevers plane dimentions were were taken as rectangular shape 100 μm x 30 μm. In case of properly calibrated BL cantilevers the result of recalibration was approximately 0.97 of the original k_{cant} obtained from the JPK software. Since the result is very close and coherent with the original the recalibration of all the probes was performed on all the spring constant values with internet applet based on Sader method. This helped to fix the mistake to input incorrect value of cantilever width in the original calibration procedure of some BL cantilevers. It is important to note that the measurement of resonant frequency is independent from cantilever plane dimensions input in analysis software and did not have any impact on ω_0 and Q value. In that case the recalibration coefficient was in a range of 1.29-1.33. This method has both perks and significant disadvantages especially in liquid. As stated by an inventor [168] the method is robust only for rectangular cantilevers of ratio length:width higher than 3:1. Nevertheless, the error introduced is systematic and independent of the non-ideal PSD smoothing procedure that introduces significant errors in P value. Obtained k_{sys} does not scale linearly with cantilever approximated plane dimensions. They serve to calculate a characteristic linear dimension of a flow and hence a Reynolds number participating in the final shape

of hydrodynamic function.

3.1.4 Dynamic Force Spectroscopy

Dynamic Force Spectroscopy underlies on application of mechanical force in order to stretch a molecular bond resulting in bond rupture or protein unfolding under distinct loading rates. This may be executed by various devices applying a range of loading rates to break molecular bond or unfold a protein: AFM [23, 153, 163], micropipette aspirated vesicle [54, 154], optical [106], or magnetic tweezers. The current work is a result of AFM scrutiny as it provides high spacial and force resolution, allows a well localised probing limited to local cellular properties, and relatively easy, robust probe functionalization procedure. In case the energy landscape parameters of protein unbinding remain unknown, complexes' mechanical properties and unbinding forces cannot be derived by thermal nor structural analysis. DFS with a tip properly functionalized with one of complexes' ligands allows to obtain necessary data experimentally. Curve collection cycles are being repeated multiple times with functionalized tips accounting for the statistical nature of a single binding/unbinding event. The example of schematic system for DFS measurement is presented in the Fig. 10. The DFS technique requires measurement of a set of FD curves with different retract velocities. The most probable unbinding forces for each rupture events batch are plotted against the corresponding loading rates. The description of data obtained directly from an experiment requires a theoretical framework. George I Bell in 1978 was the first who provided an attempt to model unbinding events in AFM experiments. His original theory described in the chapter 3.3 models the separation energy between two living cells pressed against each other by the means of AFM. Cellular membranes are described as viscoelastic fluid mosaic bodies with a biphase plasma membrane and a known area concentration of transmembrane receptors of a certain mobility. DFS as a molecular recognition probing technique allows to manipulate and investigate single molecules or cells and describe adhesion processes in a way impossible to obtain by solution methods.

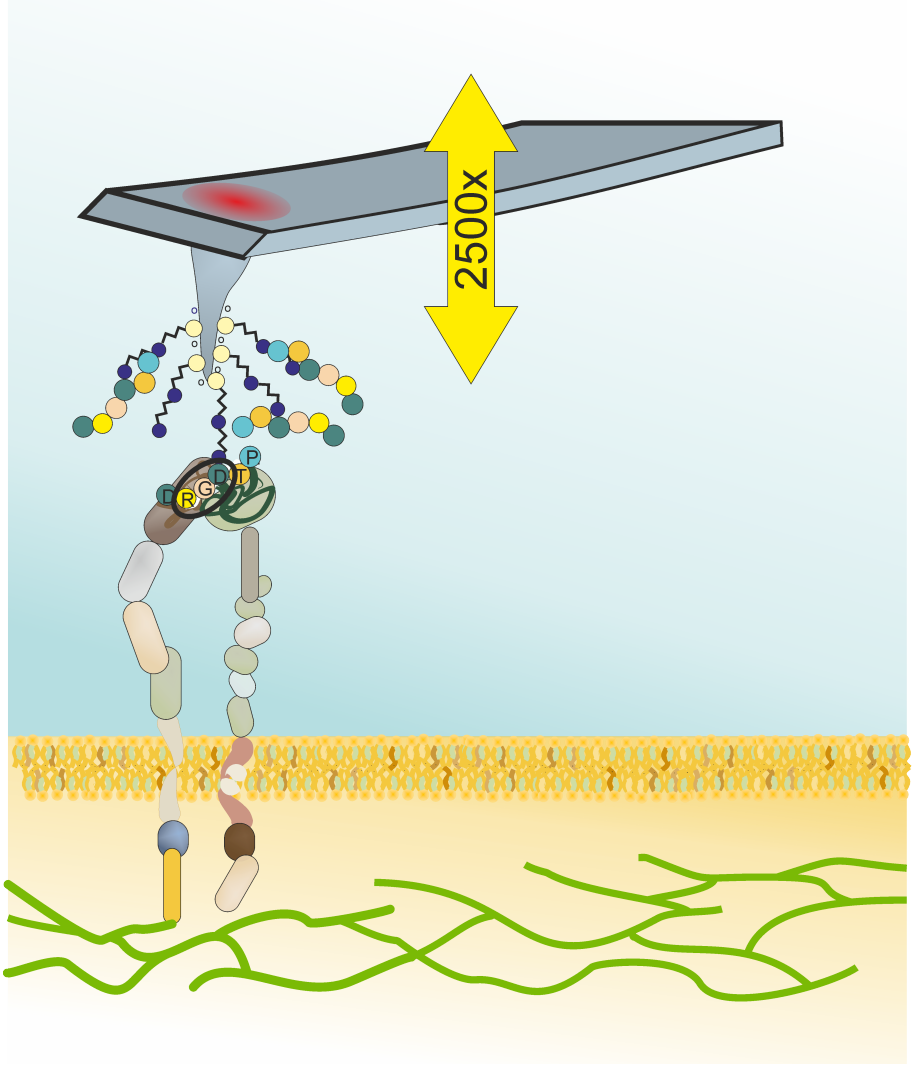

Figure 10: The out-of-scale scheme of DFS measurements system include flexible cantilever, in which functionalized tip with a ligand (GRGDTP) binds to cellular transmembrane receptor (integrin) connected with an actin cytoskeleton. The arrow symbolizes repeating measurement 2500 times for each probing velocity.

3.2 Brownian dynamics

In liquids, thermal vibrations that cause dissociation of complexes are dissipated due to viscosity of the surrounding medium. In such a case, off-rate[7] depends not only on the complex resonant frequency, but also viscous friction posing a damping agent. The famous theory by Krammers describes thermally driven escape of a molecule from a potential well over an energy barrier. The complex unbinding energy landscape is approximated as a constant flux of probability density along a certain pathway. It leads from a global energy minimum over a potential barrier with a saddle point. Many distinct trajectories of complex unbinding are allowed in the phase space. Pulling force applied along the reaction trajectory tilts the complex unbinding energy landscape. The DFS technique introduces the need to measure a set of FD curves with different retract velocities and plotting obtained unbinding forces for each rupture event against corresponding loading rates. A theoretical framework provides the description of data obtained directly from an experiment. In order to quantitatively describe data obtained from DFS measurements, there are specific models required. They bridge a gap between experimental data and theoretical description of molecular dynamics of weak non-covalent interactions. The single molecular bonds are supposed to get disrupted by any means of force pulling in a direction of reaction coordinate across the one dimensional energy barrier. The distance between bound and unbound state of a complex is denoted as bound distance x_b. The George Bell's original theory models the separation energy between two living cells pressed against each other by the means of AFM. Bell's theory aims to deduce bond formation and rupture rates from their elementary constant rates, the area density of receptors, and membrane mobility. It assumes individual antibody-receptor interaction to have known forward and reverse rate constants. The reaction follows:

$$A + B \leftrightarrow AB \leftrightarrow C \tag{24}$$

[7] The off-rate is a product of vacuum vibrational frequency and quasi-equilibrium possibility to reach the E_b energy barrier of a transition state lowered by applied force times displacement. It is known also as dissociation or unbinding rate.

reversible pathway upon which reactants firstly diffuse toward each other to form an encounter complex that permits second step of reaction. Due to the low concentration of AB complex it is allowed to assume that the described reaction is a first-order kinetics reaction and thus $\frac{d[AB]}{dt} = 0$. Bell concluded also that equilibrium constant of a described reaction does not depend on the diffusion constants. It is worth to notice, that diffusion constants may be limited for the cellular receptors in the contact. In principle, cells of the same type carry a similar electrical charge. However, they do not repel each other thanks to the ions present in culture medium that significantly screens electrostatic interaction. Then, Debye screening distance is assumed to reach around 1 nm. Additionally, van der Waals forces between cell membranes are supposed to be longer range and attractive. The effective unspecific energy separation landscape of cells detachment is expected to follow the path with a secondary minimum as shown in the Fig. 11.

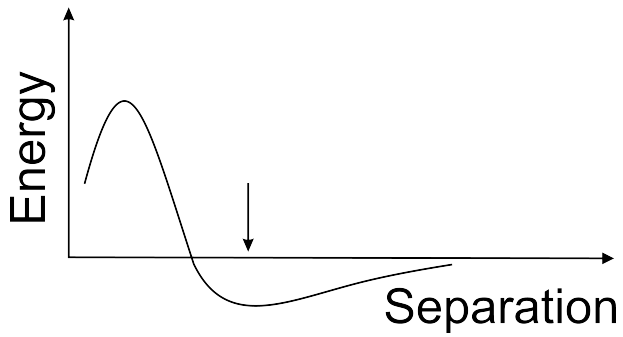

Figure 11: The energy versus separation dependence of two planar cell membranes interacting with each other. The energies are cumulative result of electrostatic and electrodynamic forces [10] with a secondary minimum indicating a moment of cells detachment indicated with an arrow.

A specific bond formed between a ligand and receptor derive their stability from multiple small free energy changes possibly associated with hydrogen, Van der Waals and electrostatic interactions. Considering each ligand-receptor complex in between two connected cells usually needs to be ruptured independently one of another, even despite each bond has a finite lifetime the probability of simultaneous cells detachment is estimated as incredibly low. However, each of the bonds is

reversible and can be ruptured under the force pulling ligands. Bond stretching and subsequent separation of the molecules is possible under applied pulling force exceeding critical force F_c. The force applied to rupture the bond diminishes the energy barrier up to causing its disappearance for the $F_c = \frac{G_0}{x_b}$ where x_b is a bond length and G_0 denotes bond free energy. According to a kinetic theory, the stretched bond lifetime τ equals:

$$\tau = \tau_0 \exp \frac{G_0 - x_\beta F}{k_B T} \tag{25}$$

where x_β is an empirical parameter dependent on the thermally averaged projection of the barrier along the direction of force, and τ_0 states for the bond lifetime and the natural frequency of atoms oscillations reciprocal. The $\tau(F = 0)$, namely in the absence of pulling force, would be a reverse rate constant.

Specific interactions originate in non-covalent forces generating relatively strong adhesion between molecular groups. The term "specific force" can refer to all types of interactions that are present only between a specific pair of molecules. Such interactions characterize with well described stoichiometry. Most of the biological interactions are results of specific binding. In principle, several non-covalent bonds such as hydrogen, Van der Waals or ionic bonds favoured by the conformation of the interacting molecules cooperate to lead to a specific bond creation. The specific interactions originate in:

1. The dispersion force that acts between all molecules and atoms at distance ranging around 0.2-10 nm. The interaction thus is the most important contributor to VdW forces. It can be both attractive or repulsive. The dispersion force is a dipole interaction of quantum-mechanical nature. The corresponding potential w_{VdW} expression takes shape of:

$$w_{VdW} = -\frac{3}{2} \frac{\alpha_1 \alpha_2}{(4\pi\epsilon_0)^2 r^6} \frac{(h\nu_1)(h\nu_2)}{h_P\nu_1 + h_P\nu_2} \tag{26}$$

where α_1 and α_2 are electronic polarizabilities of molecules, h_P is a Planck constant, ϵ_0 and ϵ are dielectric constants of vacuum and water, and $h\nu_1$ and $h\nu_2$ are ionization potentials of molecules.

2. The Keesom force being an angle-averaged dipole-dipole interaction between molecules or atoms:

$$w_K = -\frac{u_1^2 u_2^2}{3\left(4\pi\epsilon_0\epsilon\right)^2 k_B T r^6} \tag{27}$$

where u_1 and u_2 are dipole moments of the molecules

3. The Debye force being an angle averaged dipole induced dipole force of corresponding potential:

$$w_D = -\frac{u_1^2\alpha_2 + u_2^2\alpha_1}{(4\pi\epsilon_0\epsilon)^2 r^6} \tag{28}$$

Although Van der Waals forces may take part in specific binding, they are also the main source of non-specific adhesion force. The term of Van der Waals forces describes wide variety of interactions proportional to $\frac{1}{r^6}$, where r is a distance between atoms or molecules participating in bond formation [23] The great advantage of operating AFM in water solution is screening and subsequent minimization of VdW and elimination of capillary interactions forces. VdW interaction is greatly reduced in medium in comparison to vacuum, nevertheless it still remains the major force responsible for specific biomolecular interactions. It is worth to note that VdW interactions may be attractive, vanishing or repulsive depending on the molecules and their conformation. VdW forces are non-additive i.e. the other molecules act as if they were part of surrounding medium. Moreover, the VdW interaction is affected by retardation effects. The time a potential field of the first atom needs to reach the second one and back can be compared to the period of the dipole fluctuations. At large distance, due to the retardation effect, the power law index increases. For distances greater than approximately 100 nm, the dispersion force decays proportionally to -$\frac{1}{r^7}$. The described effect appears to be very important in liquids, due to lowering of the light speed. Then the effect appears to be relevant at distances smaller than 5 nm. Only the dispersion term gets retarded, while the polar remains not retarded at any distance. In a liquid solution, Van der Waals force has three distinct distance regimes. Small distances characterize with force dependence of $\frac{1}{r^6}$. Then the force law becomes $\frac{1}{r^7}$ at intermediate distances, where the retarded dispersion is dominant. Further, the never retarded polar inter-

action, turns out to be dominant and the force law comes back to $\frac{1}{r^6}$. Importantly, retarded VdW force involves a smaller effective volume than the non-retarded Van der Waals force because of its decay on smaller distances [94]. Thus, retardation is important for geometry of an AFM tip of choice. Another important feature of VdW interaction is its anisotropic character. The polarizabilities of the molecules take different values for distinct directions of the molecules. Thus, the dispersion force between two molecules depends on their relative orientation. However, the last of described effects plays important role mainly in solids due to the reduction of molecular thermal motion. The forces in between the cells are expected to be electrically repelling due to the negative charge of the membranes. However, in culture medium environment screening of the cells negative charge with bivalent cations occur. The Debye length takes value of around 1 nanometer. Additionally, Van der Waals forces between cell membranes are supposed to be attractive and ranging further than the electrostatic forces. The overall result is supposed to be an attraction between the cells' membranes.

3.3 Bell-Evans phenomenological model

The first historically relevant and still applicable Bell-Evans (BE) model describes dynamic strength of adhesion bonds for the DFS of single bonds purpose. It was developed by Evans and Riche [55] in 1997 basing on Bell's incorporation of Krammers theory of reaction kinetics in DFS data description. Kinetic model means that rupture force depends on a loading duration and value of force applied during the process. Evans and Riche introduce the stochastic nature of a rupture event resulting in the set of experimentally registered distributions of unbinding forces. The main observation of Bell-Evans model is that application of external mechanical force can change the energy landscape of a bond and cause its rupture i.e. applied force lowers the energy of a bond (dissociation upon the external force is a state far from equilibrium). The described model assumes bond rupture to proceed with constant velocity and no rebinding likelihood. External pulling force takes shape:

$$F = k_{comp}(x_b + vt - x) \tag{29}$$

Along reaction coordinate x, where k_{comp} is a ligand-receptor complex stiffness and v is a constant velocity applied in time t. The original idea incorporates Bells transition state theory to build a phenomenological model for the reaction off-rate k_{off}. The off-rate is a product of vacuum vibrational frequency and quasi-equilibrium chance for reaching the E_b energy barrier of a transition state lowered by applied force times displacement.

$$k_{off} = \omega_0 \exp E_b - \frac{F x_b}{k_B T} \tag{30}$$

$$= k_0 \exp F x_b k_B T \tag{31}$$

where applied force F pulls exactly along the bond coordinate axis; x_b is being reached exactly in the transition state and thus it is denoted as a bond length; k_B is a Bolzman constant and T is temperature. The model assumes the probability of a single complex rupture in the time interval dt:

$$P(t + dt) = p(t) \cdot (1 - k_{off}(t)dt) \tag{32}$$

The model by Evans and Riche accounts for an external force generated by AFM to be linearly changing with time under constant velocity conditions. Bonds would rupture in a finite time even in the absence of pulling force i.e. under zero loading rate, where loading rate l_r is defined as velocity v times system spring constant k_{sys} in N/s and it describes how fast an external force increase with time:

$$F(t) = k_{sys} \cdot v \cdot t \tag{33}$$

$$= l_r \cdot t \tag{34}$$

where k_{sys} is an effective spring constant of a system including an AFM cantilever and a receptor molecular complex with a ligand deposited on the stiff surface or on a membrane. Moreover, l_r is responsible not only for the shift of force toward

higher values, but also distribution broadening.

$$p(t,F) = \frac{k_0}{l_r} e^{\frac{x_B F}{x_b l_r}} e^{\frac{k_0 k_B T}{x_B l_r}} e^{\frac{x_b F}{k_B T} - 1} \tag{35}$$

The theory assumes bond breaking upon probe pulling force to be time and loading rate dependent within three dynamic regimes of loading rate. Initially, the bond strength emerges at a rate of loading allowing spontaneous dissociation and distribution peak remains zero. Further in a slow loading regime strength rises proportionally to the loading rate to reach a stage in which unbinding force rises with a loading rate logarithm for many ranges of magnitude independently of the type of attraction. This last regime is the only one available experimentally. The main observation of BE model is that application of external mechanical force can change the energy landscape of a bond and cause its rupture i.e. applied force lowers the energy of a bond. Dissociation upon the external force is a state far from equilibrium. The described model assumes bond rupture to proceed with constant velocity and no rebinding likelihood. External pulling force takes shape following equation 29 along reaction coordinate x. When applied force F pulls exactly along the bond coordinate axis; x_b is being reached exactly in the transition state and thus it is denoted as a bond length. The specific unbinding force, the bond rupture force corresponding to a maximum of unbinding probability distribution, depends linearly on the natural logarithm of loading rate:

$$F_{unb} = a \cdot \ln(l_r) + a \cdot \ln\left(\frac{1}{a k_{off}}\right) \tag{36}$$

where $a = k_B T / x_b$ and k_{off} is a dissociation rate of a complex. Thus, it is easily visible that unbinding force F_{unb} is a linear function of loading rate logarithm [133]. The function can be rewritten once more as:

$$F_{unb}(l_r) = aln(l_r) + b, \tag{37}$$

where $b = aln(\frac{1}{ak_0})$. The final relation can be fitted with a straight line taking

shape:

$$F_{unb} = aln(l_r) + b, \tag{38}$$

where a, b can serve to decode the off-rate at zero force k_0 value being a reverse of bond lifetime τ_0. Such a dependence is characteristic for a wide variety of antigen-antibody complexes, particularly specific monoclonal antibodies against a corresponding receptor. The described course of reasoning assume only for a single energy barrier, while there are multiple barrier crossings possible. More complex energy landscape may originate in complex unbinding sites, that result in multiple local potential maxima and minima of unbinding. Such a case was described for $\alpha_5\beta_1$ integrin for instance [122]. Thus, the description of a single experiment involves multiple linear fits resulting in a corresponding number of bond lengths and dissociation rates, each separate for a single energy barrier. It is necessary to evaluate based on a stoichiometry and ligands conformations, whether multiple barriers are feasible in a particular case[8].

Since dissociation under force in dense liquid solution is slowed down by viscous damping, many thermal impulses sum up to cause one potential barrier escape event. The external force is described as stationary over the time scale of complex unbinding. Thus, it is allowed to assume velocity distributions to be almost Maxwellian and states thermalized. The flux of the states through the potential barrier in the direction of x takes shape:

$$J(x) \approx D_{dif}\left(\frac{-\partial E}{\partial x)}\rho - \frac{\partial \rho}{\partial x}\right) \tag{39}$$

where ρ is normalized to 1 local density of states and D_{dif} states for a local diffusion rate being limited by viscous damping. The latter one unifies two cases: when fast relaxation process causes dissipation directly and when the outer environment causes way slower conformational fluctuations. Force application in AFM is executed in a time scale significantly longer than thermal impulses relaxation times. Usually in AFM techniques probe is retracted with a constant velocity in respect

[8]Side note: ln(lr)+ln($\frac{1}{ak_0}$) can be rewritten as ln(l_r/ak$_0$), where $\frac{l_r}{ak_0}$ reduces to a dimensionless quantity. Thus, it is allowed to write ln(l_r) as if it were a dimensionless value.

to a rigid substrate on which the sample is attached. This assumption neglects the impact of elastic deformation and inhomogeneous character of for example cellular membranes. Thus, bond load increases linearly with time. Then, rupture of a bond spans around 1 ms, the value dramatically exceeding thermal impulses time that is of a range of picoseconds. The bond survival probability is more complex than simple exponential decay characteristic for a constant off-rate revealing the limits of applied model. Nevertheless, Monte Carlo simulations performed by Riche and Evans prove applicability of Krammers Brownian dynamics with a constant loading rate in liquid environment to experimental Biotin-Avidin DFS data [96]. Still, there is a restriction that rupture forces derived from molecular simulations are higher than the actual data obtained with an AFM probe [55].

3.4 Dudko-Hummer-Szabo stochastic model

Firstly, Hummer and Szabo proposed a simple stochastic model with a pulling spring that allows to extract kinetic information of a system to obtain a more exact kinetic information than from the phenomenological Bell's model. The model is also based on Krammers theory with molecules undergoing Brownian motion. The free energy, the bond length, and dynamics represented by k_0 are characterized.

The DHS model was originally proposed to describe an irreversible single molecular transition, such as a molecular complex dissociation, unwrapping of a higher-order structure, or polymer chain unfolding experiment [48, 49, 91]. According to DHS model, based on the seminal work of Jarzynski (1997), mechanical single receptor-ligand complex unbinding is a stochastic event, i.e. it depends on the retract velocity in contrast to BE theory implying phenomenological approach. Therefore, a mechanical bond rupture event is a kinetic process away from equilibrium. Hence, the DFS experiment may provide information about the unbound complex energy landscape parameters including the height of free energy barrier. The more sophisticated DHS model introduces possibility to calculate the different shapes of energy barrier crossing landscape. It provides more realistic description of bond breaking energy barrier shape than the Krammers derived BE model of molecular bond rupture under mechanical pulling force. However, the DHS model

also relies on Krammers theory, it takes in account simple free-energy surface model as well. It assumes bond length in the absence of force described also as a distance along the pulling direction between the free-energy minimum and the transition state x_b dependence on pulling force. Energy landscape is described by three parameters: unbinding rate (off-rate) k_{off}, x_b, and the Gibbs free energy denoted as the height of the energy barrier ΔG^*. According to DHS model, the complex diffuses on a harmonic free-energy surface with a single sharp barrier while it is pulled with a constant velocity v by a harmonic spring. The DHS model for high forces provides also the critical force F_c value at which the barrier ΔG^* vanishes, the apparent activation free energy, and a parameter proportional to a diffusion constant. The molecule pulled by a soft spring with a force acting along the x direction moves on a combined free-energy surface:

$$U(x) = U_0(x) - Fx \tag{40}$$

U(x) is specified by the Krammers theory free energy surface so that:

$$U(x) \approx U_0(x) - 1/2k_{sys}(x - vt)^2 \tag{41}$$

Then

$$k_{off} = k_0 \left(-\frac{vFx_b}{\Delta G^*} \right)^{\frac{1}{\nu}-1} e^{\Delta G^* \left[1-(1-\nu F x_b/\Delta G^*)^{1/\nu}\right]} \tag{42}$$

where ν is a factor responsible for free-energy surface shape. If it gets replaced with 1, the phenomenological BE model is restored. In opposition to BE, DHS model predicts that force does not depend linearly on $\ln(l_r)$, but with a power of 3/2 or 1/2 for paraboloid and cusp-like shape of unbinding landscape respectively. It is worth to note that according to DHS the pulling force also changes the bond length, which makes the model greatly more realistic (Fig. 3.4). The rebinding is assumed to occur within a time scale of microseconds, which makes it irrelevant from a point of current scrutiny.

For irreversible complex rupture upon an external pulling force F(t) increasing monotonically with time i.e. applied with constant velocity, the distribution of

rupture probability under pulling force is related to the probability that complex remains unbound after time t.

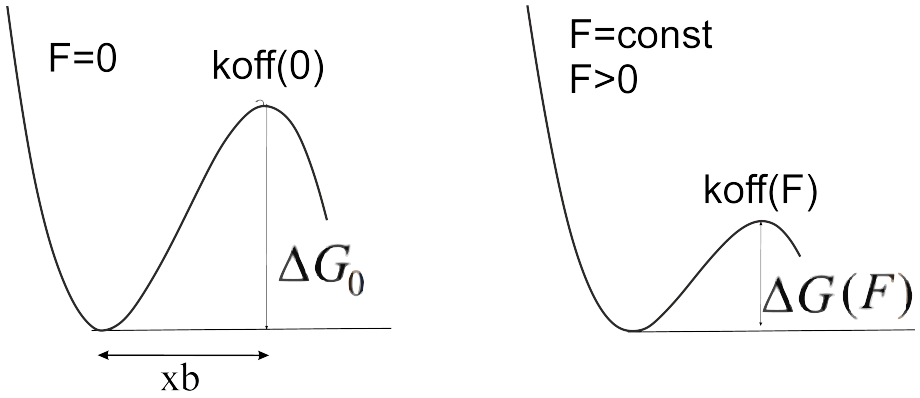

Figure 12: Single well free energy dependence on applied pulling force schematic representation. A. The intrinsic free energy in the absence of pulling force. B. The lowered upon a constant pulling force free energy.

Then the DFS data provide F_{unb} understood as an asymptotic expression for a mean rupture force under the condition of constant pulling velocity. The equation that suits to deconvolute ΔG_0 the free energy of activation in the absence of eternal forces known also as energy barrier height:

$$F_{unb} = \frac{\Delta G_0}{x_b \nu}\left[1 - \left(\frac{1}{\Delta G_0} ln \frac{k_0 e^{\Delta G_0 + \gamma}}{x_b l_r}\right)^{\nu}\right] \tag{43}$$

The value of ΔG_0 is expressed in $k_B T$ units. The fit provides also the value of $k_0 = k_{off}(0)$ intrinsic rate coefficient and the distance between free energy minimum and the transition state in the absence of force x_b known also as bond length. γ is Euler-Mascheroni constant and ν represents free energy shape coefficient that equals 2/3 for linear cubic and 1/2 for cusp like shape of energy barrier. When γ is set to zero, it gives the maximum of the rupture-force distribution to a good approximation.

3.5 Worm-like Chain model

The Worm-like Chain (WLC) model is traditionally used in polymer physics to describe the semi-flexible polymers unfolding [129,163,198]. It assumes persistence length within a few orders of magnitude of the polymer length and that a molecule can be described as continuously flexible elastic rod of a constant maximum length L_c known also as contour length. The molecule bending energy in temperature T takes shape:

$$E = \frac{1}{2} k_B T \int_0^{L_c} L_P \left(\frac{\partial^2 \vec{r}(s)}{\partial s^2} \right)^2 \tag{44}$$

where L_P is the polymer's persistence length, $\vec{r}(s)$ is a position vector along the chain: s$\in (0, L_c)$, k_B is the Boltzmann constant. At finite temperature, the molecule end-to-end distance is significantly shorter than the maximum length L_c due to thermal fluctuations, which result in a polymer coiling. L_P is characteristic of a specific molecule at constant temperature. It describes the distance over which the chain orientation is lost and the rigidity of the molecule [184][9]. Dudko et. al postulated, on the base of unzipping of DNA hairpins in a nanopore experiment, that WLC model can suit for the description of single-molecule force-distance (FD) curves obtained from DFS experiments with constant pulling velocity [50]. If flexible molecular linkers are present, system can be treated as a harmonic spring. Then, the flexible linker can be described by a worm-like chain. Such approach to FD curves analysis not only provides information about the unbinding force value but also about the location of force-induced structural transitions within the molecule and system elastic properties. The next generation of WLC - Extensible WLC (EWLC) takes in account the elastic response of a polymer undergoing stretching by an external force. It allows to obtain the information about increase in peptide length upon stretching. Traditionally, WLC model describes a molecule as a semi-flexible chain of rods characterised with a bending energy. Molecule stretching energy is then described as a line integral of chain resistance and stretching upon a force. Extensible WLC model takes in account the impact of elastic stretching of each segment thus adding new degrees of freedom. In a typical protein unfolding

[9] presented for freely-joint FJC

experiment characteristic sawtooth pattern on FD curve representing unfolding is considered a stepwise increase in the polymer contour length whose elastic properties are described by the WLC model [163]. In those experiments a force applied for example by AFM is responsible for gradual polymer chain unfolding resulting in a sawtooth FD curve profile. In this thesis, the EWLC model (black curve fitted to experimental data in the Fig. 13) was applied in order to distinguish specific binding events.

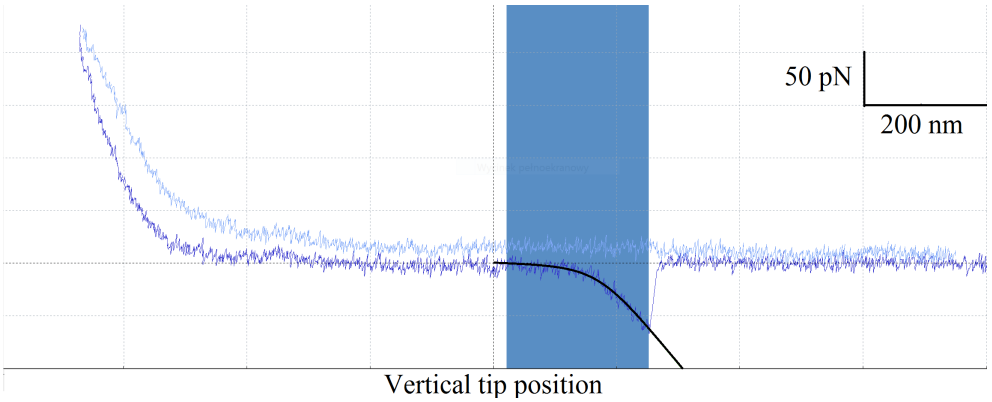

Figure 13: An unsmoothed FD curve collected with 10 μm/s velocity on the surcafe of HT1376 cell. The tract segment presented in light blue, the retract in navy blue, the EWLC fit in black. Dark blue region signifies part of curve EWLC model was fitted. The rupture force equals 63.83 pN with residual RMS 4.56 pN and the loading rate 1.43 nN/s.

The model describes the force F_{EWLC} of stretching a molecule in the x direction as:

$$F_{EWLC} = \frac{k_B T}{P_L}\left(0.25\left(1-\frac{x}{L_c}\right)^2 - 0.25 + \frac{x}{L_c} - 0.8\left(\frac{x}{L_c}\right)^{2.15}\right) \tag{45}$$

L_c denotes contour length (the length of a polymer after full extension), P_L is a persistence length, a property of a polymer describing its bending stiffness normalized by $k_B T$ - a Boltzmann constant multiplied by temperature. The applicability of some polymer chain models in DFS data description was already tested. For example the application of WLC, FJC and their modification to force-distance

curves of $\alpha_5\beta_1$ integrins versus GRGDSP peptide suggested that modified WLC model fits data the most robustly [110]. The Fig. 13 shows also the significance of EWLC model application for the identification of specific bonds by their shape. In isolated system as opposed to cells, the bond length is up to an order of magnitude shorter. The tract part of curve in Fig. 13 shows how easily deformable is the cell surface. Such a soft material is reflected also in the shape and length of unbinding profile. Thus, the cell surface mechanical parameters have significant impact on system spring constant and should be taken in account. The EWLC model fulfils this need by providing a spring constant value that includes the impact of probe, antibody-receptor bond, and elastic membrane.

4 Materials and methods

4.1 Materials

4.1.1 Cell lines

Studies within the thesis were carried out using the following bladder cancer cell lines:

- HCV29 - non-malignant cancer cell of ureter (developed at the Institute of Immunology and Experimental Therapy PAS, Wroclaw, Poland),
- 5637 also known as HTB-9 - urinary bladder carcinoma, grade 2 (5637, LCG Standards, Manassas, Virginia, USA, ATCC cell line),
- HT1376 - urinary bladder carcinoma, grade 3 (CRL-1472, LCG Standards, Manassas, Virginia, USA, ATCC cell line),
- T24 – transitional urinary bladder cell carcinoma, grade 3, (HTB-4, LCG Standards, Manassas, Virginia, USA, ATCC cell line),
- TCCSUP also known as HTB-5 - urinary bladder transitional cell carcinoma, grade 4 (TCCSUP LCG Standards, Manassas, Virginia, USA, ATCC cell line).

The ATCC stands for American Type Culture Collection (Manassas, VA, USA). The cell lines were cultured at the Department of Biophysical Microstructures at the IFJ PAN in an CO_2 incubator (Nuaire) at the 5% CO_2 concentration in 95% air atmosphere at the temperature of 37°C. HCV29, HTB-9 and T24 cells were cultured in RPMI-1640 (Sigma Aldrich). In case of HTB-9 cells, culture medium was supplemented with 10 mM HEPES (Sigma Aldrich). The HT1376 and HTB-5 cell lines were cultured in EMEM (LCG Standards). All the culture media contained foetal bovine serum (FBS; Sigma Aldrich) at the final concentration of 10%. Cells were passed after they reached confluency level of 85-90%. Prior to AFM measurements, cells were cultured for 2-3 days in complete culture medium that was being replaced with measurement medium lacking FBS. This procedure limited the impact of the non-specific AFM probe adhesion to the cell membrane

raised in the presence of FBS. The growth of HTB-9, HT1376, T24 and HTB-5 cells in culture was characterized by mixed epithelioid-fibroblastoid morphology while non-malignant HCV29 preserved epithelial morphology.

Cell passage was performed according to a standardized procedure for 25 cm^2 culture flasks at the subsequent steps:

1. Medium removal.
2. Rinsing cells with clean medium without FBS and incubation for 4' in 37 °C.
3. Cells' incubation with 2 ml trypsin PBS solution for 3' in 37 °C.
4. Checking if all the cells detached from plastic surface, if not application of a delicate mechanical stress and point 3 repetition.
5. 4' 1800 rpm centrifugation of cells suspension with 4 ml medium enriched with 10% FBS.
6. Supernatant removal.
7. Passing cells 1:3 or 1:4 depending on needs into the new culture flasks with 10% FBS medium.
8. Passage repetition every 3-4 days or after cells reach 85%-90% confluence.

4.1.2 Fluorescent staining

Fluorescent microscopy was used as a tool complimentary to the AFM to visualize cytoskeleton components and test the presence of β_1 integrin in HCV29 cells. To visualize cellular components, mainly actin filament organization, fibronectin, β_1 integrin subunit and cell nuclei, fluorescent microscope was employed (inverted Olympus, IX53). All the images were collected with XC10 digital camera providing a resolution of 1376 x 1038 pixels and subsequently analysed with CellSens Dimension Desktop software (Olympus). Human bladder cancer cell lines were cultured in the Petri dishes prior to fixing them with 3.7% paraformaldehyde for 20 minutes at room temperature. Then, the standard staining protocol for Alexa Fluor 488 phalloidin (Invitrogen) for actin staining and Hoechst (Invitrogen) for

Table 1: Standardized nominal parameters of used probes according to a producer, the f_{rez} is a nominal resonant frequency and k_{cant} a cantilever spring constant as claimed by the manufacturer.

Probe	Shape	Width [μm]	Length [μm]	f_{rez} [kHz]	k_{cant} [pN/nm]	Tip angle	Tip height
TR400	triangular	27.9	200	11	20	25° - 45°	2.9 μm
BL	rectangular	30	100	13	6	<45° side <90° front	7 μm

nuclei staining were employed. Coverslips were rinsed with the phosphate buffered saline (PBS, Sigma) and their membrane was permeabilized using 0.2% solution of TRITON X100 (Sigma Aldrich) for 5 minutes. In order to visualize β_1 integrin prior and after incubation with 200 μl solution of 50 μg/ml monoclonal antibody against β_1 integrin (anti-β_1 Mab, Sigma Aldrich), cells were thoroughly rinsed with the PBS buffer. Afterwards, cells were incubated with mouse monoclonal antibody conjugated with tetramethylrhodamine (TRITC) conjugated secondary IgG antibody (Invitrogen) for 30 minutes (1:64 in PBS), and then again rinsed several times with PBS. All the stained samples were rinsed with PBS and imaged afterwards.

4.1.3 AFM probes and functionalization

Force distance curves were collected using triangular OMCL TR400PSA-1 (Olympus) and semi-rectangular BioLever BL-RC150VB-C1 (Olympus) 100 μm silicon nitride cantilevers with sharp respectively pyramidal 20 nm tip set back to the cantilever end and V-shaped depression in the silicon nitride 30 nm tip. The use of sharp tips allowed to minimize the Coulomb forces between tip and surface. TR400 cantilevers characterize with the nominal force constant of 20 pN/nm [38], and BL with 6 pN/nm [37]. Additionally cantilevers were covered with gold layer to enhance laser spot reflection. The standardized parameters of levers provided by a manufacturer are presented in Table 1.

The use of 7 μm high BL tips prevented touching sample with the cantilever base and limited the probe edges-sample contact. Moreover, BL cantilevers ensured

lower spring constant than TR400 cantilevers. Gold cover on both sides allowed stable signal detection, thus BL cantilevers are described as a low noise cantilever. There are two common approaches to AFM tip chemical modification. One of them is to functionalize probes using a relatively small molecule like for example 3-amino-propyltriethoxysilane (APTES, Sigma Aldrich) and then glutaraldehyde (GA, Poch S.A., Poland) carrying NH_2 group. The other is a choice of long polymer spacer linker. The spacer is a molecule few nanometers long, which is stretched during the unbinding event making the rupture of the bond occur at distances greater than characteristic for non-specific bond breaks. Both methods have certain perks but also carry some risk. The APTES linker cannot be considered as a spacer as it is a small aminosilane molecule immobilizing ligand on the surface of the tip. The tips were functionalized using firstly APTES 90' incubation in desiccator followed by 20' immersion in 2.5% GA solution in water. Later on cantilevers were rinsed thoroughly in PBS and incubated for 30' with a ligand of choice:

1. GRGDTP (Sigma Aldrich) specifically recognizing RGD-binding pocket in VN, FN and OPN binding integrins 0.01 mg/ml PBS solution (TR400),

2. FN4-12 (kind gift from P.Marszałek (Duke University)) recognizing FN binding integrins 0.1 mg/ml solution (BL),

3. MabSDC-1 recognizing 82–256 amino acids sequence of human syndecan-1 extracellular domain (A-6 Santa Cruz Biotechnology, Inc.) 0.2 μg/ml PBS solution (TR400, BL)

4. MabSDC-4 recognizing 93–121 amino acids sequence of human syndecan-4 extracellular domain (Santa Cruz Biotechnology, Inc.) 0.2 μg/ml PBS solution (BL),

and thereafter rinsed with PBS prior to measurement. The use of sharp tips al-

lowed to minimize the Coulomb forces between tip and surface and thus multiple binding. Since there is no control over the number of ligands attached to the tip, the complementary molecules may be attached and randomly distributed over the tip. Thus, this leads to the possibility of detachment at different distances, and hence a specific force-displacement curve can present multiple unbinding events. In case of probing membrane of cells not having well established actin cytoskeleton, it is also possible to pull the elastic membrane surface. This contributes in all-over loading rate by lowering the value of k_{sys} and displacing unbinding event toward further parts of retract curve. A few nanometers long spacer, stretched during the detachment, suites to enforce the rupture of the specific bond at distances greater than those characteristic for the non-specific events. However in case of soft elastic cell membrane, that can be pulled, also non-specific bonds might get shifted toward other parts of the curve. The use of a short linker immobilized ligands better than an elastic spacer. Then, the specific events were distinguished from non-specific events by the shape of a curve right before the unbinding event.

4.1.4 Blocking experiments

The interactions blocking experiments are necessary to confirm ligand specificity in the DFS based experiments [85]. For example Tees et. al. performed dynamic force spectroscopy with a bead attached to a micropipette and a glass fiber to check the interactions between E-selectin and sialyl Lewis^x sLe^x. To confirm the specificity of a set-up they run three separate experiments: without E-selectin on a fiber, with Le^x a trisaccharide similar to sLe^x but not binding to E-selectin and in the presence of blocking antibody. All the blocking experiments confirmed specificity of examined interaction [202]. There are several approaches available: either cell transfection blocking the expression of a cellular ligand, blocking specifically the binding site with its ligand, changing the conformation of at least one of the complex reagents so that the complex cannot be created even if ligands come into contact, or blocking the tip. Some experiments were performed blocking the tip functionalization with a specific antibody or using not functionalized probe. In case of this study, such a blocking experiment is not necessarily robust due to ability of

some of HCV29 cells to produce fibronectin [120]. Experiment performed with a 15 μm - 25 μm bead without functionalization on the surface of silicon wafer covered with IgG antibodies resulted in several times higher unspecific adhesion force than the results obtained for a bead covered with corresponding molecule [189]. The non-functionalized probe does not assure that a probe is perfectly clean (especially in the presence of living cells medium), nor that electrostatic interactions between probe and surface are eradicated. Because of that reason, blocking experiments with not functionalized probe are difficult to perform and to assure their robustness. However, the most certain - the transfection procedure is costly and requires sophisticated biological methods and legal permissions. Hence, in the course of this thesis preparation, it was necessary to use rather chemical or physical interactions blocking agents. In case of measurements with a GRGDTP and FN4-12, GRGD (Sigma) - a short sequence containing RGD binding site was incubated with cells to block the free RGD binding sites on the cells' membranes without a risk of attachment to the tip surface. The intact VN (Sigma) suited to block the VN binding sites on integrins. The blocking experiments included incubation for 60' with either 25 μM of GRGD peptide or 25 μM VN. For EDTA experiment cells were incubated for 30' with 1 mM EDTA in 10 mM HEPES in PBS and assessed as fast as possible before they detached from the surface. The EDTA was in the solution was chelating divalent ions thus, removing them from cells memebrane. EDTA is a common agent added to trypsin in order to facilitate cells deadhesion by blocking integrins and cadherins interactions and removing divalent ions from membranes. However, sometimes it is also used to block the interactions that specifically demand divalent ions in AFM experiments [78]. The α subunit, responsible for integrins ligand specificity, contains MIDAS necessary to bridge ligand binding in presence of Mg^{2+} ions [115]. Moreover, it forms salt bridges that determine the conformation and subsequently α subunit activity. The experiment on $\alpha_5\beta_1$ integrin GRGDSP peptide unbinding showed the raise of unbinding force value upon Mn^{2+} concentration raise and drop after addition of Ca^{2+} and EDTA. The error values do not allow statistically significant conclusion [110].

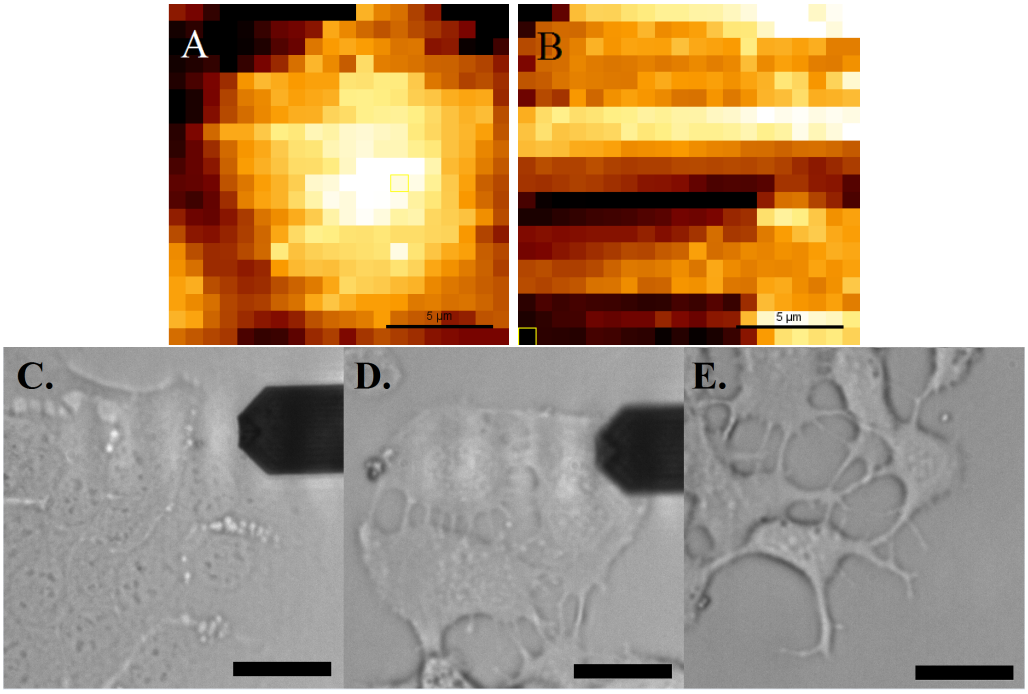

Figure 14: Approximated height AFM image of HT1376 cells collected on a surface of A. firmly attached cell, B. not fully attached cell. Image was constructed basing on 20x20 points measured every 800 nm. Scale bar in the images A-B corresponds to 5 μm. Optical images of cells: C. in pure EMEM medium, D. firmly attached cells in 1 mM EDTA solution, E. almost detached cells in 1 mM EDTA solution. Scale bar in the images C-E represents 30 μm.

EDTA is commonly used in order to facilitate cells trypsynization and (in several tenths times higher concentrations) to prevent blood components from agglutination. Actin molecules responsible for cytoskeleton stability and shape of a cell contain ADP or ATP in the cleft between the domains binding Ca^{2+} [100], thus removal of divalent ions by EDTA strongly impacts the shape of cells. Hereby, it is a potent reactant limiting cellular adhesion also to the surface on which the cells are seeded. Procedure is performed relatively quickly and undergo further evaluation if cells were fully attached to the surface of Petri dish during the whole course of the experiment. The example of evaluation criterion is presented in the Fig. 14.

In case of syndecan-1 and -4 monoclonal antibodies interactions, the chemical blocking agent was 12.5 μg/ml CASK peptide. The interactions in 1 mM EDTA in 10 mM HEPES in PBS were also performed. The Ca^{2+}/calmodulin-associated Ser/Thr kinase (CASK peptide), was isolated thanks to its ability to bind to the neurexins in yeast [79]. However, CASK can bind directly to EFYA sequence, the COOH-terminal tail of the syndecans incorporating its PDZ domain [89, 90] and takes part in epithelial polarity and synaptic assembly. CASK regulates proliferation and adhesion when it is present in nuclei of newborn rats epidermal keratinocytes. Relocation of CASK into the membrane correlates reversibly with differentiation. The turn-over in keratinocytes occurs as a result of serum starvation [142].

4.2 Data processing

The DFS experiment requires very careful data analysis with an awareness of possible error sources. The analysis needs to focus on several crucial points. As the experiments with PEG linkers showed, the specific unbinding event is characterised with a well-defined profile of force vs. distance interaction. The characteristic non-specific unbinding FD curve is a straight line or an irregular profile followed by the point denoting a rupture event. In case of specific unbinding, a cantilever can snap back to its relaxed position resulting in a sudden, straight line force drop. The curve profile in the last phase before unbinding can be described with a Worm-Like Chain (WLC) model or its modification Extensible WLC (EWLC)(Fig. 13). EWLC model takes in account the impact of elastic stretching of each segment of a polymer chain thus adding new degrees of freedom to a traditional WLC model. The EWLC model (black curve fitted to experimental data in the Fig. 13) in section 3.5 was applied in order to distinguish specific binding events. Thus, it allowed to resign from a PEG linker and to obtain the actual value of loading rate. The commercially available JPKSPM Data Analysis (JPK Instruments AG, Berlin, Germany) software includes built-in WLC and EWLC analysis applet generating not only a bending length and a rupture force, but also a loading rate as a probe retract velocity multiplied by a complex system constant k_{sys} determined from a

part of curve used for EWLC fitting (blue area in the Fig. 13).

During DFS measurement cantilever is continuously approached and retracted from a surface at the constant speed with a piezoelectric actuator. For the sake of a scrutiny of proteins immobilized on the flat, rigid surface like for example mica it was enough to assume system constant k_{sys} as dependent only on cantilever constant k_{cant}, receptor and bond stretching properties. However in case of living cells, multiple factors like a deformability of cell membrane outer layer alters significantly the k_{sys} value and thus the complex extension length before bond rupture event. The baseline fitting and hydrodynamic compensation, EWLC model fitting and the determination of loading rate and unbinding force were performed in JPKSPM Data Processing verion 6.1.96, a commercially available software by JPK Instruments AG. The process used included built in chain of predefined functions: Smooth Data, Switchable Baseline Operation, Vertical Tip Position, Linear Fit Height, Adhesion, Curve Statistics, Area Under The Curve, Chain Model Fit. Smoothing was usually set to 0 on the arbitrary scale. In case of TR400 cantilevers it was set to 1 for curves collected with velocity 0.5 μm/s and 1 μm/s while for BL only for 0.5 μm/s. The setting were accepted after confirming that they do not change the value of unbinding force, but only lower RMS and facilitate finding candidates for unbinding events. Switchable Baseline Fit was always set to treat retrace curve, fit baseline to a manually determined linear part of a curve and tilt helping to compensate hydrodynamic drag. Vertical Tip Position suited to correct the height for the bending of the cantilever and to calculate the vertical tip position. The cantilever deflection in units of length was subtracted from the piezo height. Adhesion and Area Under The Curve provide information about maximum unspecific adhesion and work of adhesion respectively. The Chain Model Fit allowed choice of EWLC model type and a standard smoothing of 4 points. Its changes in a range 0-5 did not affect the value of unbinding force. The contact point had to be set every time manually and was considered the first point when the retract curve crossed with the baseline indicating zero force with the user defined accuracy of 0.1 μm. The information obtained from the function were: breaking force, loading rate. and RMS of the part of a curve used to fit EWLC model. The obtained data

underwent further analysis. The unbinding probabilities were calculated as a ratio of unbinding events to the total number of curves collected in the sample. The graphs picturing the unbinding probability and distributions of single unbinding events were executed in Origin Pro 8. The histograms generation and BE model and DHS fitting was performed using self-written code in Python 3.7.3 with the use of SciPy, Numpy libraries. The fitting procedure of choice was Orthogonal Distance Regression (ODR) using ODRPACK 2.01 [13]. It minimizes the sum of the squared weighted orthogonal distances from a set of observations to the curve determined by the model equation with parameters of choice. The use of ODR instead of the least squares method was dictated by the significance and a broad distribution of loading rate errors. For example the standard errors corresponding to loading rate values of around 10 000 pN/s were several fold greater than the values of mean loading rates of the histograms corresponding to the lowest loading rate values. After the values of x_b, k_0, τ_0, and in case of DHS also ΔG were fitted, they were compared to the correspondent values for HCV29 (or HTB-9). The statistically different result was assumed if

$$|x_i - x_j| > \sqrt{(dx_i^2 + dx_j^2} \tag{46}$$

where x_i, x_j are values of a parameter and dx_i, dx_j are corresponding error values. The curves were fitted in accordance with BE and DHS described in 3.3 and 3.4 respectively. Each time the color code of HCV29 blue, HTB9 green, HT1376, T24 red, and HTB-5 purple corresponds with the malignancy grade of a cell line.

5 Dynamic Force Spectroscopy as a tool to characterize binding of fibronectin fragment (RGD) to integrin receptors

5.1 Objectives

The Dynamic Force Spectroscopy (DFS) allows to examine the molecular complexes unbinding force dependence on loading rate. Since the AFM probe may be functionalized with a wide variety of distinct ligands, it appears possible to assess the interactions between the more complex proteins fragments and the simpler, smaller binding domains of proteins. Thus, it allows to decode the molecular fragments complexes impact on protein binding energy landscapes. This chapter focuses on binding of fibronectin fragment to receptors present on the surface of bladder cell lines, i.e. on non-malignant HCV29 and malignant HT1376 cells. These two cell lines differ in integrin superfamily receptors members present on their surface(private communication, unpublished data). The DFS measurements were performed with a tip functionalized with either GRGDTP peptide containing the RGD sequence responsible for predominant fibronectin, vitronectin, and osteopontin binding or with FN4-12 large fibronectin fragment containing also a synergy binding site in FN9 domain. The use of short GRGDTP hexapeptide resulted in the determination of energy landscape parameters of RGD unbinding complex with the semi-specific integrin binding site. The bond is characterised with a statistically different lifetime and length according to the BE model. Distinct cell lines expressing different integrins resulted in altered bond energy landscape parameters. Parameters reconstruction was particularly important because the relations were not clearly visible when comparing data points by eye. Although similar character of bonds resulted in energy landscape parameters that differ sometimes by only 10%, it was possible to evaluate which bonds are more stable. In case of FN4-12 experiment the HT1376 show significantly smaller values of bond lifetime τ_0 for BE analysis and free energy ΔG for DHS model respectively. Both models predict slightly ($\approx 10\%$), but significantly longer bond length for GRGDTP bind-

ing to the surface of HT1376. Simultaneously, no difference in bond stability was detected. The scrutiny sheds light on the topic of complexity of energetic parameters dependence of the larger molecular complexes. Important part of a chapter is also devoted to establishing a protocol for efficient and reliable dynamic force spectroscopy data collecting and analysis procedure. In recent years, DFS becomes more and more popular technique, though in case of by nature more demanding biological samples it was still lacking error analysis and robust data normalization. However, the EWLC (Extensible Worm-Like-Chain) model application in the living cells data analysis was recommended for DHS model due to its construction [50]. It also significantly rises the quality of obtained results by limiting system spring constant, and hence a loading rate error. In spite of the mentioned advantages, this method was rarely applied in live cells' measurements.

5.2 Materials and methods

Cell lines The cell lines incorporated in this chapter measurements were non-malignant HCV29 (control sample) and grade 3 bladder carcinoma HT1376. Cells were cultured for 48-72 h prior to measurement as described in the section 4.1.1.

Probes The OMCL TR400PSA-1 (TR400, Olympus) 200 μm long triangular cantilevers with pyramidal tip and 100 μm long silicon nitride gold coated BioLever cantilevers with V-shaped cleaved tip (BL, Olympus) were used. Tips were functionalized according to standardized procedure described in 4.1.3 with GRGDTP and FN4-12 respectively.

The calibration of cantilever spring constant All the callibration procedures were performed as described in 3.1.3. In case of GRGDTP functionalized triangular OMCLTR400PSA-1 cantilevers, the probe calibration included the standard JPK software built-in contact-based calibration procedure (paragraph 3.1.3). It consists of two steps: sensitivity determination basing on a linear regime of calibration curve on a rigid material (Petri dish surface) and thermal tune spring constant determination. The sensitivity value was measured in situ in working medium environment with a consistently maintained value of 2 V offset. The same part of every curve was linearly fitted to obtain the apparent measuring set sensitivity expressed in nm/V. The thermal tune spectrum at zero deflection was collected each time at least 300 μm away from the surface in measuring medium after a minimum of 40 minutes environment thermal stabilization. The PSD spectrum region corresponding to the first oscillation mode was chosen manually. The contact free calibration of FN4-12 decorated 100 μm long BioLever BL-RB150VB (BL) was also performed in a measuring medium and temperature at least 300 μm away from a Petri dish surface. The cantilever recalibration based on the Sader method [168, 169] in an Internet applet [167] was applied.

DFS measurements The Nanowizard 4 JPK (Berlin, Germany) AFM head is equipped with the standard AFM detection system: position photodiode detec-

tor. The four photodetecting quadrants allow optical lever method of cantilever deflection and torsion registration. This widely used, robust method is based on reflecting laser spot from the back side of a cantilever tip and subsequent measurement of the position of reflected light beam using a position photodiode sensor in two perpendicular axes. The more detailed description of the system functioning principles is included in 3.1 whilst the Dynamic Force Specctroscopy technique is described in 3. Each DFS scrutiny included at least 3 repetitions with different probes against a surface of distinct cell culture merged in order to provide reliable statistics and fitting data points count. Each blocking experiment consisted of 2 or 3 repetitions. HCV29 cells were immersed in standard RPMI-1640 medium without FBS for the time of measurement while the HT1376 measurement was performed in standard EMEM without FBS. The blocking experiments with GRGD, VN, and EDTA were performed as described in 4.1.4. In each medium the collected grids of points denoted as a "map" were 8 x 8 points (10 μm x 10 μm) in case of GRGDTP peptide decorated probe and 10 x 10 points (8 μm x 8 μm) for FN4-12 resulting in 800 nm distance between probing points. The average BL tip radius declared by the manufacturer is 30 nm. The rise of points count per map was possible due to higher stability of FN4-12 functionalized BioLever cantilevers in liquid medium. Maps were collected over the same area for the set of velocities. TR400 probing was executed with 0.5 μm/s, 2 μm/s, 5 μm/s, 10 μm/s, 15 μm/s and 20 μm/s. Additionally, FN4-12 scrutiny was enriched with 1 μm/s, 3 μm/s and 7 μm/s. This range translated into loading rates in a range 20-30 000 pN/s. Half of the measurements was performed ascending velocity and half descending to make up for the possible scanner drift.

The specific unbinding events The image of β_1 integrin, one of the most common integrins in epithelial cells stained in HCV29 cells is presented in the Fig. 15. The distribution of β_1 integrin is approximately even in the whole cell body with possible aggregations around the centres of adhesion and lower concentration around nuclei. The actin cytoskeleton characterizes with organization of stress fibres.

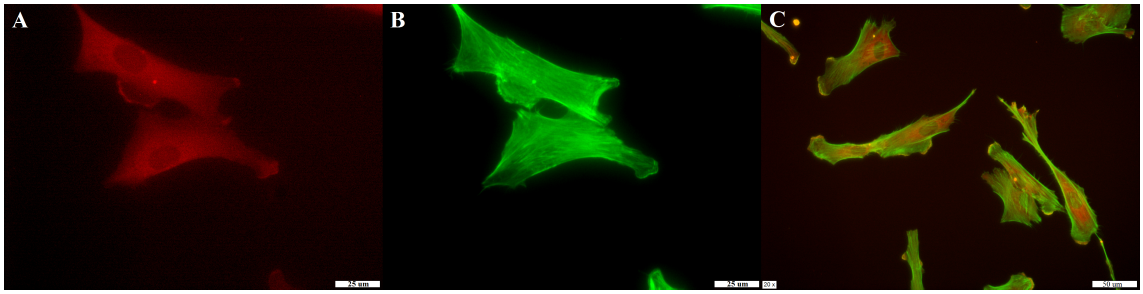

Figure 15: A. The β_1 integrin (red) and B. the f-actin cytoskeleton (green) structure revealed by immunofluorescent staining in HCV29 cells. C. the merged image of β_1 integrin (red) and f-actin (green) in smaller magnification.

Since the unbinding process has a stochastic character, the unbinding forces differ from one FD curve to another and require a statistical analysis of F_{unb} distributions. The important part of data analysis takes in account a realistic value of system constant and the robust error analysis.

The Residual RMS of a curve fragment representing a moment before the rupture event is taken as a primal unbinding force error source under condition that it cannot be smaller than the cantilever force detection limit calculated as $\sqrt{k_{cant} \cdot k_B T}$ (for the BL 100 μm cantilever approximately 5 pN and for TR400 200 μm approximately 8 pN in 25°C-30°C). A distribution of results for GRGDTP probing including the unbinding forces with root mean square (RMS) as force error value is presented in the Fig. 16. It pictures the expected tendency of mean unbinding force and RMS values rising and distribution broadening for higher loading rates. Simultaneously, Fig. 16 presents overlapping data points for different probing velocities. Measured values of unbinding force were merged for each sample type, ordered by ascending value of corresponding EWLC derived loading rate value and divided into sets of 150-200 data points. In case the sample consisted of data points number that modulo 200 was a value lower than 150, the pre-last data set was enlarged by remaining points. Otherwise, the new data set of 150-199 points was created and taken in account for future analysis. Each unbinding force data set underwent frequency count with bin size determined by mean RMS.

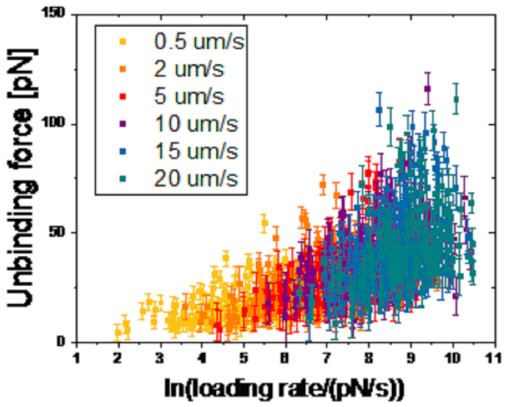

Figure 16: The results of a DFS experiment with GRGDTP decorated TR400 against HCV29 cells. Unbinding forces with RMS derived error bars are plotted against natural logarithm of loading rates. The probing velocities ranged between 0.5 μm/s and 20 μm/s.

It is worth to notice that with the rise of loading rate also the RMS value increased. Thus, this leads to higher uncertainty of unbinding force values for higher loading rates. Fitting theoretical model with weighting by error values obtained according to the presented method allows statistical incorporation of aforementioned phenomenon.

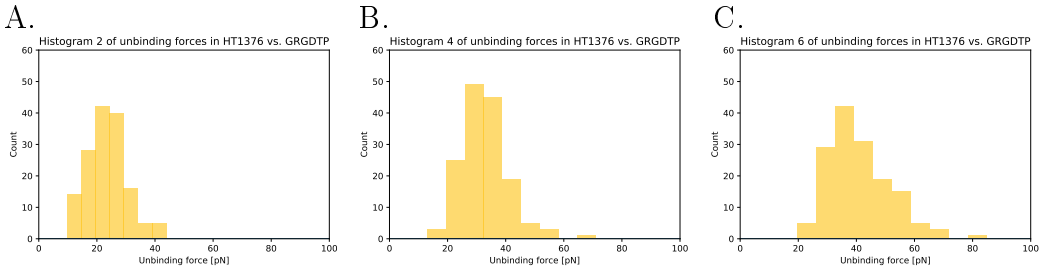

Figure 17: Three typical histograms of 150 unbinding forces values correspondent to loading rates of A. 400-1236 pN/s B. 2515-4248 nN/s C. 6335-9580 nN/s. The result of DFS experiment with GRGDTP decorated TR400 against the surface of HT1376 cells.

Then the Gaussian function with zero offset was fitted to each of the histograms

in order to calculate the most probable unbinding force for each batch of data. The distribution mean value was assumed to be a result of the most probable unbinding force of the data set with an error value taken as $\frac{3SD}{\sqrt{N-1}}$ where SD is a mean standard deviation and N points count (typically 150-200). Most probable unbinding forces obtained this way were plotted against the mean value of natural logarithm of corresponding loading rates with standard deviation error values. Thus, the obtained plot of most probable unbinding forces against loading rates natural logarithms was enriched with a robust error analysis. Force histograms corresponding to lower loading rates are narrower than those corresponding to higher loading rates because of logarithmic of force-loading rate dependence. This is in agreement with the fact that histograms of unbinding force are way broader for high values of l_r than those for lower loading rates. Additionally, the first and the last histogram always broaden as a result of outliers impact.

5.3 The energy landscape parameters according to Bell-Evans model

The DFS measurements retract velocity range of 0.5 μm/s to 20 μm/s was proven to be optimal from the point of specific unbinding probability observation as shown in the Fig. 18. Moreover, the multiple bonds, which occur more frequently upon the low loading rates, stabilise the adhesive contacts and hence cause the overestimation of the unbinding force. Very low force of 0.25 nN (BL) to 0.35 nN (TR400) was applied on the surface of examined cells causing no deterioration nor disassembly of the structures during multiple measurements in approximately the same spot. Most often the approximated height image of cell surface was maintained during measurement and specific adhesion events were occurring in the same or nearby pixel of an AFM force map. Each time the environment temperature of approximately 300 K was assumed for the sake of energy landscape parameters calculation. Then k_BT was approximated as 4.14 10^{-23} J.

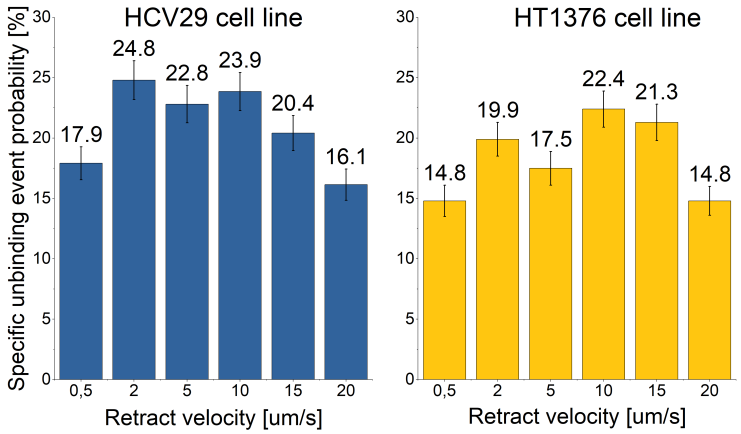

Figure 18: The specific unbinding probability for GRGDTP functionalized TR400 probe for different probing velocities ranging from 0.5 μm/s to 20 μm/s.

Fig. 18 presents a statistically significant decrease in unbinding probability for the 20 μm/s and 0.5 μm/s tip retract velocities. This might occur due to the contact time insufficient to establish a fully formed complex between ligand and receptor in case of 20 μm/s probing velocity. Regarding 0.5 μm/s probing velocity, the lowering of unbinding probability may be a result of the system force resolution limit. Some of the unbinding force values may be below the error value. The unbinding force value was not taken in account in case when its value was smaller than the error. The error was calculated as RMS value of EWLC analysed part of curve or a cantilever force resolution calculated as $\sqrt{k_{sys}k_BT}$. The last value equalled 5 pN for BL probe and 8 pN for TR400 probe. The data obtained in described way were subsequently fitted with two distinct theoretical models. Namely, the Bell-Evans model (BE) and Dudko-Hummer-Szabo model (DHS) introduced in chapters 3.3 and 3.4. The BE model allows more than one linear fit denoting the count of energy barriers necessary to cross in order to rupture complex. In the DFS scrutiny of FN7-10-$\alpha_5\beta_1$ integrin complex unbinding, it was assumed that bond rupture energy landscape consists of two barrier crossing events [122]. This approach was also common in experiments not including living cells like biotin-avidin complex examination [53,96]. Development of x and y error analysis allowed

to establish an arbitrary criterion of bimodal energy landscape without the need of taking in account *a priori* assumptions requiring for example exact knowledge about bound ligands conformations. Initially the linear function y=ax+b was fitted with a confidence bands of 95%. The two energy barriers were assumed if there was a certain point on linear fit line before which all the points were below curve and after which - above the fit plot. The BE fit results in the robust determination of time average distance between molecules of a complex bond length x_b and off-rate in the absence of pulling force k_0. Off-rate is an abstract value hard to imagine and estimate its robustness. The more intuitive bond lifetime $\tau_0 = \frac{1}{k_0}$ in seconds values were also compared.

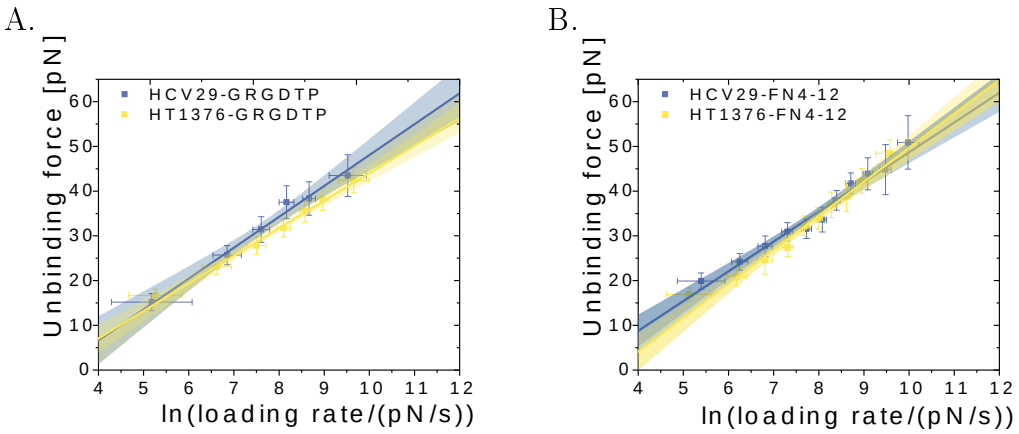

Figure 19: The BE model fit to the DFS data obtained using A. TR400 probe functionalized with GRGDTP hexapeptide sequence and B. BL probe functionalized with FN4-12 peptide for non-malignant HCV29 cells and grade 3 HT1376 cells. The data were measured and analysed according to the procedure presented above. The linear fit corresponds with $F_{unb}(ln(l_r)) = aln(l_r) + b$.

The results presented in the Fig. 19 and in the table 2 imply relatively small, yet statistically significant difference in the energy landscape parameters of RGD site binding rupture depending on bladder cancer cell line. All the length of a bond x_b was approximately 10% lower for HCV29 as compared to HT1376. The other parameters were not significantly different. This can be explained by a small size of binding domain making it independent of conformational changes of RGD

Table 2: Comparison between HCV29 and HT1376 parameters derived from BE model linear fit to the DFS data obtained with the TR400 probe functionalized with GRGDTP peptide and BL probes functionalized with FN4-12. The a and b denote the linear fit parameters. The x_b, k_0 and τ_0 parameters characterise the energy landscape according to Bell's model (3.3).

cell line vs ligand	a	b	x_b [pm]	k_0 [1/s]	τ_0 [ms]
HCV29-GRGDTP	6.90 ± 0.51	-20.9 ± 4.0	600 ± 44	2.98 ± 0.48	336 ± 53
HT1376-GRGDTP	6.15 ± 0.30	-17.5 ± 2.4	673 ± 33	2.78 ± 0.31	360 ± 41
HCV29-FN4-12	6.65 ± 0.43	-17.8 ± 3.3	623 ± 41	2.17 ± 0.31	461 ± 64
HT1376-FN4-12	7.59 ± 0.48	-26.2 ± 3.7	567 ± 38	4.96 ± 0.68	202 ± 28

receptor and corresponding glycation process. For example RGD sequence is known to bind to a wide variety of integrins that are either specific for RGD sequence of fibronectin, vitronectin, osteopontin, or two of those listed. A probe functionalized with a short sequence eliminated the impact of fibronectin conformational changes, steric barriers and other complimentary binding sites like PHSRN or syndecan binding site both present on FN mode III9 and III12-14 respectively. The next step was to measure the unbinding force and calculate the unbinding energy landscape parameters of a larger and more complex fragment of a protein responsible for integrin receptors binding. The fragment of choice was FN4-12 present on mode III fibronectin. It contains both RGD and PHSRN sequences but no HepII domain as shown in the Fig. 1. The PHSRN motif is complimentary to the main RGD binding site and necessary to provide the full adhesion of fibronectin to its specifically binding integrin $\alpha_5\beta_1$ [162]. In addition, the chosen fragment is lacking a syndecan binding site for integrin specificity of interactions. The results in case of FN4-12 are very much ifferent. The bond length x_b is also 10% shorter for HT1376 cells but that is not enough to state statistically significant difference. The τ_0 is significantly shorter for grade 3 HT1376 suggesting less stable bond in the equilibrium state. The reason of changes may lie in the impact of additional LDV and PHSRN sites supporting the RGD in full adhesion or in the impact of conformational changes of a bigger FN fragment but also the fact that longer fragment is more conformational changes dependent. The results are presented in table 2.

The relevant difference is visible in the table 2 in case of complex bond length when cells were probed with GRGDTP probe and in dissociation constant and hence bond lifetime when FN4-12. However, the difference between statistically significant and insignificant complex bond length change is minimal. The bond lifetime drops almost twice in case of FN4-12 binding to HT1376 cells as opposed to HCV29 cells. This may suggest that larger fragment of fibronectin has properties that suit malignant cells to facilitate detachment and hence migration. Simultaneously, the effect is not visible for GRGDTP hexapeptide. The data appear robust and fit the linear regression very well (R^2 on the level of at least 0.98). Nevertheless, the mean unbinding forces obtained using BL probe are influenced by the smaller errors in comparison to those of TR400. Another important possible error source that determines the unbinding force of a molecular complex is the pulling geometry. The mechanical properties of a complex are anisotropic, correlated to the topological and tertiary ligand and receptor structure, and ligand distribution on a tip surface enlarging the measured unbinding force error. The effect is the more pronounced, the longer, and the more complex a molecule of interest is. In both situations obtained loading rates are similar. The simple intuitive approach would suggest that on stiffer cells loading rates should be higher than on more elastic surfaces. The experimental results of this study contradict initial intuition. The HCV29 cells were proven to have significantly higher Young's modulus measured by the means of AFM than the malignant bladder cancer cell lines HTB-9, HT1376 and T24 [155]. This occurs due to HCV29 cells highly developed actin cytoskeleton and stress fibres making them greatly stiffer. The scrutiny was confirmed with the fluorescent imaging of actin cytoskeleton proving higher level of fibrillar actin in stress fibres in non-malignant HCV29 than in the other mentioned cell lines. The explanation of mismatch between the two results is that in case of Ramos et al. studies they were performed with an indentation force 1 nN greatly exceeding the one applied in this experiment. The 1 nN force indentation corresponded to 500-1000 nm indentation depth where actin mechanical properties are dominant while in the case of a current study, the membrane deformation was around one order of magnitude smaller. The main ingredients having impact on the

loading rate values are the ligand and the receptor stiffness, membrane receptors concentration, and deformations of cells' phosphate lipid membrane. Nonetheless, the indirect impact of actin cyoskeleton on the receptor conformation cannot be excluded. Integrins are interconnected with the cytoskeleton structure that can stabilise them and anchor in the membrane. However the bonds between integrins and actin cytoskeleton have less pronounced impact on the loading rates range. Thus, the k_{sys} taking part in loading rate value depends only on the condition of a very local fragment of membrane closest to the surface. The differences in actin cytoskeleton structure, however significant from the nanomechanical point of view, do not have impact on the loading rate value.

5.4 The energy landscape parameters according to Dudko-Hummer-Szabo model

Dudko-Hummer-Szabo model largely differs from the BE model that assumes infinite energy barrier. It does not explicitly provide the bond free energy value. The more complex DHS model, which assumes for an finite energy barrier of a certain shape, was incorporated. The significance of energy landscape parameters calculation lies in the understanding that it provides an information of how free energy changes upon molecule stretching, unfolding, and eventually ligand-receptor bond breaking in the bond coordinate. On the example of protein unfolding: shallow potential will lead to smaller unfolding or unbinding forces than the sharp potential of the same depth. That is why the same energy of protein folding can possibly lead to distinct unfolding properties depending on the length over which the energy is distributed. Thus, mechanical properties examination provides information that other biological techniques such as unfolding under changing pH, temperature, and denaturation agents do not provide [164]. Analogously, receptor-ligand unbinding properties described in this thesis are fully characterized when the free energy of unbinding, bond length[10] and lifetime are determined simultaneously. The DHS model was constructed to provide all of the parameters mentioned

[10] understood as activation barrier length

above accounting for a specific shape of an unbinding potential. However, the information regarding binding remains unknown, the unbinding properties of cell membrane receptors are crucial for the deeper understanding of such processes as migration and metastasis.

Table 3: Comparison between HCV29 and HT1376 parameters derived from DHS model fit to the DFS data obtained with the TR400 probes functionalized with GRGDTP peptide and the BL probes functionalized with FN4-12. The ΔG, x_b, k_0 and τ_0 parameters characterise the energy landscape according to DHS model (3.4.)

cell line vs. ligand	ΔG [k_BT]	x_b [pm]	k_0 [1/s]	τ_0 [s]
HCV29-GRGDTP	9.24 ± 0.63	840.0 ± 66.0	0.52 ± 0.13	1.93 ± 0.47
HT1376-GRGDTP	8.93 ± 0.23	944.0 ± 42.0	0.63 ± 0.11	1.58 ± 0.28
HCV29-FN4-12	8.98 ± 0.27	835.0 ± 42.0	0.66 ± 0.14	1.52 ± 0.32
HT1376-FN4-12	8.49 ± 0.23	831.0 ± 39.0	0.79 ± 0.15	1.26 ± 0.23

The results shown in table 3 correspond with parameters fitted to the same set of experimental data as BE model in table 2. In this case, the model was fitted to the points representing single specific unbinding events under the loading rate. This approach partially originated in the fact that for the histogram derived points the initial fitting parameters could dramatically change the final fitting outcome without significant changes in the fit goodness. Moreover, as the DHS model authors suggest, fitting the mean rupture forces is insufficient to determine all the three unbinding parameters including ΔG. They advise at minimum to include variances but better to use the Bayesian approach to data fitting. A robust analysis and ODR method requires both x and y errors: the x error was calculated with the derivative method from equation 45 in chapter 3.5, while y error was the RMS value taken from the last part of the curve before unbinding jump. It was calculated as $\frac{RMS}{F_{unb}} l_r$ because loading rate depends only on the persistence length value. The ODR method was chosen because of the logarithmic data distribution and loading errors of a significant value especially for the higher loading rates. The

authors suggested that for the sake of regime of AFM experiment where the barrier is high and the intrinsic rate is slow, the energy barrier shape should be assumed as linear-cubic with a corresponding ν parameter equal 3/2 [49]. The procedure of choice allowed to lower the fit parameters errors in some cases by even an order of magnitude.

5.5 The unbinding probability and supporting methods

Unbinding probability, defined as a ratio between the number of curves showing specific unbinding events in the overall count of force curves recorded, denotes how many specific unbinding events occur in a semi-quantitative way. To assure robust scrutiny, the experimental conditions must be maintained including probe type, coating, applied force, and retraction velocity. Since the operator does not have a direct impact on the loading rate values, the unbinding probabilities need to be compared for the same probe velocity. Nevertheless, for example measurements with the same velocity on cells treated with EDTA usually correspond to lower loading rates because the system spring constant changes when the sample gets more elastic. The cells naturally soften and become more circular in the presence of EDTA after a long term incubation. However, maintenance of constant probing velocity, number of curves collected per sample, cell line and passage is expected to provide robust results. The unbinding probability around 30% ensures that there is an 86% chance that the measurement reflects a single receptor-ligand unbinding according to Poisson distribution and 14% of double bonds [202]. In this work the unbinding probability was kept even lower to minimize the impact of double bonds while keeping it significantly higher than the non-specific adhesion rate. The blocking experiments and the previous works in the field suggest that the unspecific adhesion rate varied around 2.5-4%. The choice of a blocking agent is crucial for the success of a scrutiny. Not always blocking with the ligand used to functionalize tip is the first choice. The trials of blocking experiments with FN (not presented) resulted in high occurrence of curves exhibiting unspecific adhesion. Such shape of AFM curves makes analysis more difficult and lowers its robustness significantly. In this work the GRGD peptide was incubated with cells to chemically block the

free RGD binding sites on the cells' membranes while vitronectin suited to block the VN binding sites on integrins. The use of GRGD was dictated by the fact that the smaller the molecule is, the lower the likelihood that it can cause additional unspecific interactions. Additional GRGD assets included the availability and the low price of the peptide. GRGDTP peptide chosen to decorate probes was slightly longer, which provided chance to attach it to a glutaraldehyde crosslinked aminosilanized surface. In case of a blocking agent this feature was neither necessary nor appreciated. The similar reasons suggested the choice of 75 kDa 459 aa vitronectin rather than approximately 440 kDa fibronectin that additionally has a strong tendency to identical protein binding [183] and aggregate in temperatures around 36°C. Another blocking factor VN was chosen in replacement for fibronectin fragment. The whole fibronectin could not be possibly used due to FN tendency to create highly stable dimers composed in fibres. The nonspecific adhesion of FN molecules contaminating probe would then give fake positive result. Moreover, fibronectin has multiple biding sites while VN was proven to be highly dependent on RGD sequence. Replacing RGD with either RGE or RAD on vitronectin fully abolished $\alpha_V\beta_3$, $\alpha_V\beta_5$ and $\alpha_{IIb}\beta_3$ driven adhesion [29]. Importantly, VN also contains RGD motif and hence is expected to bind in the same pocket as fibronectin, GRGDTP and GRGD peptides, but does not contain PHSRN motif present on FN4-12 required for full cellular adhesion [206]. Thus, using VN as a blocking agent does not assure blocking of all the integrins responsible for fibronectin binding. It was expected to block the interactions with integrins shared by FN and VN under the assumption that there is no α_5 integrin present in bladder epithelial cells [215]. Then, according to the Fig. 2 scheme, VN should block most of the RGD based interactions. The blocking experiment using AFM probe functionalized with both GRGDTP and FN4-12 have both proven the applicability of proposed approach. In the other blocking experiment medium was exchanged into 1 mM EDTA in 10 mM HEPES in PBS as described in 4.1.4. The EDTA containing medium was chelating divalent ions and removing them from cells membranes. The α subunit, responsible for integrins ligand specificity, contains MIDAS necessary to bridge ligand binding in presence of Mg^{2+} ions [115].

A

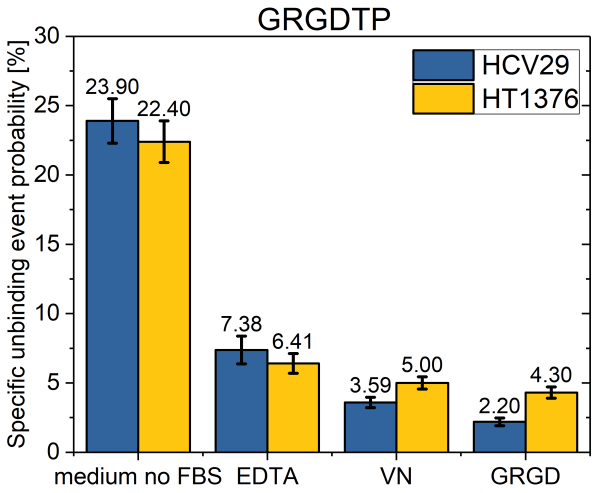

B

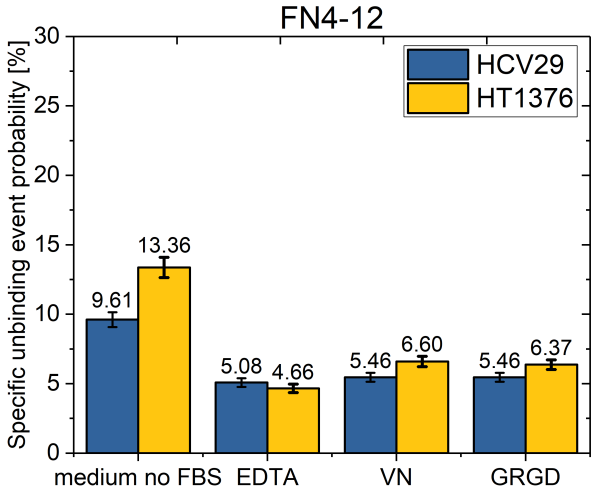

.The specific unbinding events probabilities blocking experiment for a probe functionalized with either GRGDTP A. or FN4-12 B. against HCV29 and HT1376 cell lines. EDTA means 1 mM EDTA in 10 mM HEPES in PBS. The concentrations of both VN and GRGD were 25 μM. Medium denotes a standard culture medium lacking FBS for HT1376 it means EMEM and for HCV29 RPMI-1640.

Moreover, it forms salt bridges that determine the conformation and subsequently α subunit activity. Assayed β_1 integrin subunit is known to anchor integrins to actin cytoskeleton [148]. Its AMIDAS region contains inhibitory Ca^{2+} site that allosterically affects ligand binding [136, 144]. Fig. 5.5 shows the results of blocking experiment for GRGDTP peptide and FN4-12 FNIII fragment. The data show a statistically significant decrease in unbinding probability in case of each sample.

Different cell lines exhibit distinct levels of β_1 expression. That is particularly important due to the fact that normally there is an excess of β subunit in the cell, which translates into α subunit determining the amount of particular type receptors on the cell surface [173]. The β_1 integrin subunit is known to anchor integrins to actin cytoskeleton [148].

However, the knowledge of concentrations of integrin subunits in not enough to state clearly which integrin is the most abundant and which of the present dimers would have the greatest specificity to the ligand binding. The adhesion regulation depends also on the endo-egzocytic transport of integrins between membrane and cells' inside [99] and on ECM proteins interactions specificity. For example GRGDTP peptide half maximal inhibitory concentration IC50 values are: 423 nM $\pm$ 65 nM for $\alpha_V\beta_5$ integrin (VN binding), 84 nM $\pm$ 12 nM for $\alpha_5\beta_1$ integrin (FN binding), 28 nM $\pm$ 5 nM for $\alpha_V\beta_3$ integrin (VN binding). The respective values for GRGD are: 580 nM $\pm$ 23 nM for $\alpha_V\beta_5$ integrin, 137 nM $\pm$ 14 nM for $\alpha_5\beta_1$ integrin and 55 nM $\pm$ 7 nM for $\alpha_V\beta_3$ integrin. Thus, the $\alpha_V\beta_5$ integrin has the greatest VN binding specificity. They were both not specific at all to $\alpha_V\beta_6$, $\alpha_V\beta_8$, nor $\alpha_{IIb}\beta_3$ integrins. This assay was impossible for $\alpha_V\beta_1$ integrin since it is not specific for FN only but also VN [102]. Nevertheless, the experiment with CHO-2B α_5 knocked out cells proved that $\alpha_V\beta_1$ integrin has fourfold less affinity to VN than to FN. Moreover, $\alpha_V\beta_1$ expressing CHO-2B cells were incapable of migration on fibronectin. Restoring α_5 subunit expression resulted in recreation of fibronectin matrix assembly and cell migration [230]. The determination of specific biological role of one particular integrin receptor is a cumbersome procedure due to common cross-talk between different superfamily members. The residual effect

of another closely related, possibly even unknown, RGD binding integrin can never be fully excluded. Thus, in the case of high uncertainty of the exact member of potential complex ligands subset, the stochastic physical method as DFS, which automatically includes the statistical analysis of data population, seems to be a promising solution for complex biological systems like cells and in the future perspective maybe even tissues. Importantly, it also mimics the natural environment conditions way better than the artificially isolated, simplified systems.

Prior publications on integrins expressions stated for example overexpression of $\alpha_V\beta_3$ integrin in cancerous melanoma cells [130] and bladder tissues [215]. The expression of the integrins is often regulated by external factors and $\alpha\beta$ heterodimers pair together in endoplasmatic reticulum. The non-paired monomers are retained in the reticulum. The FN binding $\alpha_5\beta_1$ integrin is expected to have higher impact on the HT1376 cells than on HCV29 behaviour. The finding is supported by the ratio of specific GRGDTP blocking in HCV29 and HT1376 cells where VN blocked 60% and 32,5% of specific interactions respectively shown in the Fig. 5.5.

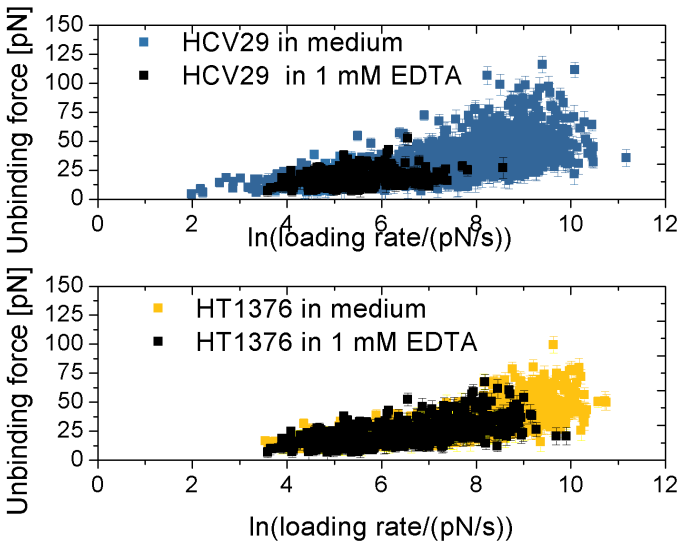

Figure 20: The unbinding forces for GRGDTP peptide retracted from the membrane of HCV29 and HT1376 cells either in culture medium or in 1 mM EDTA solution in 10 mM HEPES in PBS.

However, the GRGDTP peptide unbinding force value correspondent to the same range of unbinding forces does not change upon the divalent ion removal from the solution, the loading rate range changes significantly. The probing velocity in case in the Fig. 20 was 10 μm/s for EDTA treated sample and full range of velocities 0.5 μm/s - 20 μm/s for sample in medium. There is a visible shift in loading rates values due to membrane, cytoskeleton and their connection destabilization in a response to removal of divalent ions. Despite the shift in loading rate, corresponding values of unbinding force remain in the same range as for the not blocked interaction. The alteration introduced by divalent ions elimination is a conformational change in integrins. EDTA chelates and hence facilitates removal of divalent ions from both MIDAS and AMIDAS ion binding sites.

The topic of integrins affinity and avidity changes in response to conformational transitions is widely discussed. The bent conformation of $\alpha_V\beta_3$ integrin is believed to correspond to a low affinity. Extended conformation with an open headpiece would then be responsible for moderate affinity and open headpiece for high affinity [221]. As mentioned in chapter 2.2, integrins can exist in three different conformations: bent with low affinity headpiece, extended with high, and extended with low affinity headpiece. The low affinity extended conformation may become an interesting target for cancer research since it was proven to support rolling, but not full adhesion in neutrophils [113, 116], the feature very important for cancerous cells. The probe was a fibronectin functionalized bead attached to a red blood cell aspired by micropipette. That system was approached and retracted from expressing $\alpha_V\beta_3$ target cell. The authors concluded that bending and stretching of integrins with FNIII7-10 proceeds under around 30 pN forces [28]. Thus, it would imply that AFM probe can bend and stretch integrin molecules disregarding divalent ions impact on the final result of unbinding force measured by the means of DFS. This can explain why blocking with EDTA was significantly less effective than GRGD tetrapeptide that occupied binding sites and blocked the possibility of interaction between the receptors and the ligand immobilized on a probe surface. The short peptide GRGD is a robust blocking agent also due to the fact that this peptide is too short to be sterically impacted by the removal of divalent ions.

5.6 Chapter summary

This chapter addresses the problem of performing complex semi-specific interactions scrutiny with AFM based dynamic force spectroscopy. The aim was to obtain a robust characterization of kinetic profile of molecular complexes present between FN4-12 and GRGDTP binding distinct integrins on the surface of living bladder cancer cells. The research bridges a gap between the DFS experiments on isolated, highly specific complexes *ex-vivo*, and expression assays that do not always reflect the physiological relevance of a molecule of interest. Sacrificing the full specificity of single integrin interactions gives broader insight in collective kinetic properties of RGD binding integrins in the concentrations, clustering level, and affinities as they impact each other in intact cells. Simultaneously, DFS technique allows to probe the single molecules interactions, thus reaching a level deeper than a traction scrutiny or immunochemical assays. Such an analysis comes across many obstacles and difficulties such as inhomogeneous membrane surface, fragile and elastic probed surface, and a threat of cell membrane composition changes in response to mechanical stimuli. The range of solutions was applied to address these problems. The probes functionalization was performed using APTES dessication and subsequent incubation with 5% glutaraldehyde. Since APTES linker is a small aminosilane molecule immobilizing ligand on the surface of the tip, it is too short to be considered a spacer and does not provide additional degrees of freedom. The impact of multiple binding and the ligands deposited away from the direction of minimum separation force axis was eradicated as much as possible by limiting the number of ligand movement degrees of freedom, by application of the lowest experimentally available force and hence indentation of a sample. However, the choice of the short linker removes the possibility to distinguish between specific and non-specific bond rupture events by the linker extension length examination in a way it was proposed earlier [85]. For many years elastic linkers functionalization was the most commonly applied method. The experimental results published in 1994 clearly stated that stiff functionalization with a small molecular crosslinker did not result in registration of specific unbinding events between antifluorescyl IgG molecules immobilized on a silicon wafer and fluorescein functionalized probe. A

silicone 15-25 μm bead was glued to the tipless AFM cantilever and approached for different contact times. The authors discussed different aspects of measurements including the large discrete cantilever tilt that was the more visible, the bigger probing bead was. They concluded that immobilized antibodies without elastic spacer could not orientate properly to satisfy the steric conditions of specific bond formation. The adhesion forces they recorded were of a range of 3 nN so two ranges of magnitude larger than registered in this research. The probe-surface contact was estimated so that 14 000 IgG antibodies molecules were available to form bonds with a surface and the contact time was 1 minute. The scrutiny did not include measurements performed with probe functionalized using an elastic crosslinker in the same experimental conditions [189]. Thus, the experimental conditions were very different from modern standards. The large surface contact and the contact time exceeding examined complex lifetime effectively prevent the possibility of specific unbinding events registration due to very high unspecific adhesion occurrence in the force-distance curves even if molecules were orientated properly and specific binding was possible. Simultaneously, an experiment on biotin-avidin adhesion force performed with stylus probe (radius unknown) functionalized with avidin against the surface of a soft agarose bead decorated with biotin or iminobiotin resulted in a registration of respectively 160 pN $\pm$ 20 pN and 85 $\pm$ 15 pN unbinding forces. The definition of unbinding force in that case was the last discontinuity on the retract curve before reaching the baseline level [58]. Even such a simple analysis method resulted in convincing results when the rules of a soft substrate, a sharp tip, and low applied approach force were maintained. Usually for biological samples the value of force applied to the sample varies from a fraction, up to several tenths of nanonewtons depending on the aim of performed measurements and required indentation depth, the pressure tolerance level of distinct cell lines, and limitations originating in the tip functionalization and the force constant. The choice of a cantilever is always dictated by a compromise between better stability of higher spring constant cantilevers and the top force resolution provided by low spring constant cantilevers only. The low stiffness probes are subjected to higher thermal fluctuations in a position. Thus. they may react slower in the high damp-

ing water solution environment. However the stiffer cantilevers are less susceptible to thermal fluctuations, their force resolution is limited. Thus, it is possible to adjust the interaction force between a probe and a sample according to preference. The final choice of certain constant cantilevers is a result of compromise between the two described factors. In this work two types of soft and very soft cantilevers were tested for their applicability in cell culture DFS examination. The registration of specific unbinding forces reaching down to 8-10 pN was feasible with both TR400 and BL cantilevers. The BL cantilevers were more stable and resulted in lower force error values. The Single Molecule Force Spectroscopy in a Dynamic Force Spectroscopy mode applied in this work required the use of very low forces on the border of currently available devices' capabilities. Low force off-set of 0.25 - 0.35 nN enables DFS measurements focusing directly on the surface of the cells. Application of low force to the cell surface is crucial for an outcome of the experiment since it prevents the destruction of a tip and the molecules immmobilized on its surface, along with the rupture, or destruction of membrane receptors in cells. As low as possible force off-set value helps also to limit the dispersion of specific adhesion force results. When indenting cells on very low depths it is possible to limit both the multiple binding events and not specific adhesion to the steep edges of a cantilever tip. The interactions between GRGDTP peptide and FN4-12 fibronectin fragment and integrins on the surface of either HCV29 or HT1376 cells were measured within the range of loading rates from several pN/s up to 20 000 pN/s. The velocities were chosen to correspond to the previously described in literature loading rates. Studies based on optical gradient trap of beads covered with FN7-10 revealed that integrin-cytoskeleton linkage strength depends on matrix rigidity and composition [32]. Thus, on one hand ECM condition impacts how well integrins are anchored in the cell membrane, but also cells actively regulate their environment by secreting specific ECM compounds. The final outcome is visible in loading rate values. Unlike most of elasticity measurements aiming to reach actin cortex at the depth of 200 nm and below cell surface, loading rate reflects the condition of a membrane, which is dependent on but not indistinguishable from cytoskeleton.

The obtained data provide important quantitative and qualitative characteristics of integrin-ECM unbinding that underlie the dynamics of cancerous cells adhesion. Blocking experiments confirmed binding specificity. The use of very short peptide GRGD, assured blocking independent of conformational changes within a blocking agent and divalent ions concentrations. The EDTA blocking provided an important insight into integrin complex formation in the absence of divalent ions. The removal of divalent ions impacts the whole cell and hence the experiments need to be performed within a limited time frame. Shift in loading rates values suggests softening of the most outer layer of cytoskeleton and membrane as a result of their connection destabilization. If not the DFS measurment this result could lead to an incorrect conclusion that EDTA cause change in GRGDTP-integrin binding energy landscape. Despite lowering the value of loading rate, respective values of unbinding force remain in the same range as for the interactions measured in medium. Way higher values of binding/unbinding probability for GRGDTP can be explained by the higher binding probability of smaller, less sterically constrained peptide. Moreover, the concentration of 0.01 mg/ml GRGDTP corresponds to higher molar concentration than 0.1 mg/ml FN4-12, which has significantly higher molar mass. To ensure that the majority of the registered unbinding events were representing single bonds, surface-coating conditions were tuned to keep ligand density low in order to adjust it to the level of integrins present in cells. This reflects in the unbinding probability always kept below 30% in order to assure predominantly single bond creation. Balancing on the border of minimal effective concentrations was necessary in order to assure the domination of single unbinding events [202]. The proposed EWLC model application to distinguish between specific and unspecific binding was applied only when the discontinuity signifying single unbinding event lead to the baseline level. Additional unspecific adhesion could significantly lower the unbinding probability by masking specific events. The longer and the less specific ligand on the probe, the higher chance of this type error occurrence. The GRGD peptide was slightly more efficient in blocking GRGDTP-integrin complex interaction than vitronectin most probably due to either the impact of blocking the interactions of exclusively FN binding integrins or lower affinity of VN rather than

GRGD to membrane integrins. Usually blocking experiments include the RGD containing short sequence instead intact VN or FN [70]. This experiment shows that VN can successfully lower the unbinding probability of RGD-driven integrin interctions in DFS experiments. Simultaneously, way lower efficacy of FN4-12 binding blocking by VN and RGD may lead to the conclusion that in case of FN4-12 binding experiment, the PHSRN synergy site also had an impact on final result of experiment. When interpreting data from a semi-specific single molecule force spectroscopy experiment, it is worth to remember that integrins composition may vary between cell lines. For example β_3 subunit has two distinct sites binding either α_V or α_{IIB} subunit [125]. Different structures are expected to yield in distinct affinities of α and β subunits. Whereas $\alpha_5\beta_1$ is known as the most prominent RGD binding ligand of fibronectin, it is not guaranteed that β_1 integrin would predominantly create a complex with α_5. The RGD sequence binding is directly dependent on the α subunit binding mode. Among them possible are: side-on binding ($\alpha_V\beta_3$), end-on binding ($\alpha_{IIB}\beta_3$) or both combined ($\alpha_5\beta_1$) [102].

The unbinding energy landscape parameters determined within this chapter can suite to understand better the physical character of a chemical bond of the examined system. For example very strong, covalent biotin-avidin complex characterizes with a large value of the unbinding free energy. Simultaneously, an interaction potential spans from the entrance of the binding pocket up to the full depth of a binding pocket [137]. This results in a large value of bond length. Oppositely, the short value of x_b combined with low binding free energy value can imply a flat surface of the ligands contact and notable impact of of van der Waals interactions as expected between actin monomers. Such kind of complexes is easier to break but still ensuring certain level of dynamic stability and at the same time the system molecular plasticity, the mechanism found in most of biological interactions. The results obtained from DHS and BE models fitting would suggest the second type of interaction to be predominant in integrin binding to RGD containing ligands. Also the BE model does not provide the value of unbinding free energy but it resulted in statistically significant differences of x_b values between HCV29 and HT1376 cell lines in case of GRGDTP study. The DHS model gives more detailed insight in the

nature of this phenomenon while not preserving the same relation between reconstructed x_b values as BE model. In case of FN4-12 decorated probe HCV29 there were no significant differences in k_0 and τ_0 between cell lines. The HCV29 ΔG differ significantly from the corresponding value for HT1376. The more complex model provides deeper insight in the parameters of unbinding energy landscape but subjects to the problems originating in higher complexity of a model. The bond lifetime values derived from the DHS model bond lifetimes are one order of magnitude longer than those taken from BE model but the differences between HCV29 and HT1376 were prest only in case of FN4-12 binding according to BE model. The DHS model appears to be more restrictive than BE model and more exclusive in terms of differences identification between two data sets. The DHS model allows to conclude that HT1376 binds less tight to a ligand on probe in case of FN4-12 due to lower value of unbinding free energy. Simultaneously, the BE model predicts in this case way shorter bond lifetime that can lead to the same conclusion. The two models agree in terms of x_b changes tendency, but not according to its value. It is worth to note that the force required to bend the $\alpha_5\beta_1$ integrin value about 30 pN. The forces exerted by AFM probe are an order of magnitude larger. It is likely that every approach integrin was bent and every retract it was forced to straighten. This is an important quality of the device that should be taken in account in all the future experiments.

6 Evaluation of Bell-Evans and Dudko-Hummer-Szabo models in Syndecan-1 and Syndecan-4 DFS

6.1 Objectives

The mechanism of cell adhesion undergoes extensive studies over past years because of a great span of distinctions between cancerous cells adhesion to the ECM proteins causing differences in invasiveness and anchorage. The growing body of evidence suggests that altered adhesive properties are a fundamental property of malignant transformation in cells [8, 29, 35, 39, 105]. Despite plethora of mainly biological experiments, the theoretical framework for the physical base of complex cellular adhesion mechanism remains unclear. This chapter focuses on comparison between two theoretical models for the specific binding energy landscape parameters of syndecan-1 (SDC-1, CD138) and syndecan-4 (SDC-4) receptors to their monoclonal antibodies. The experiment set-up incorporated monoclonal antibodies of confirmed receptor specificity. It suited to calculate the energy landscape parameters of syndecan binding on living cells. It provides the solution for living cells DFS data interpretation. The receptor family of choice: syndecans are abundant transmembrane polysaccharides responsible for distinct cell types anchoring in surrounding ECM. The SDCs interactions are hypothesized to depend on composition of attached saccharides, which affect the complex conformation [72, 95]. To calculate the energy landscape parameters of ligand-receptor binding i.e. energy barrier height, most probable unbinding force, dissociation rate, and complex lifetime, one has to collect single unbinding events in wide range of loading rates. Two models were applied to calculate the energy landscape parameters: the most common thanks to its accuracy and simplicity is Bell-Evans [10,56], followed by the more complex Dudko-Hummer-Szabo model assuming more realistic energy barrier shape [48, 49, 91]. This chapter is devoted to the analysis of SDC-1 and SDC-4 receptors' interactions with their monoclonal antibodies, and the comparison of BE and DHS models when such interactions occur. It results in the unbinding energy landscape parameters determination and models evaluation.

6.2 Materials and methods

Cell lines All of the used cell lines and cell culture procedures were maintained as in 4.1.1. The scrutiny was performed for the whole panel of available cells, namely: HCV29 (non-malignant), 5637 known as HTB-9 (grade 2 carcinoma), HT1376 (grade 3 carcinoma), T24 (TCC, grade 3) and TCCSUP known also as HTB-5 (TCC, grade 4) ordered according to a rising malignant potential.

Probes and functionalization The TR400 and BL probes were functionalized according to a standard protocol as in 4.1.3 with 0.2 μg/ml MabSDC-1 and 0.2 μg/ml MabSDC-4 respectively as described in 4.1.3. In addition, the HTB-5-MabSDC-1 interaction measurements were performed with both TR400 and BL probes functionalized with 0.2 μg/ml MabSDC-1 in order to compare results obtained with different probes. The functionlization with a specific antibody binding to the epitope of a membrane receptor, namely syndecan-1 or syndecan-4 assured high binding selectivity.

DFS experiments The DFS experiments were performed with The Nanowizard 4 (JPK Instruments AG, Berlin, Germany) AFM head in standard culture medium without 10% FBS for each cell line respectively as described in 5. As previously, each scrutiny included at least 3 repetitions with different probes against a surface of distinct cell cultures merged in order to provide reliable statistics. Each blocking experiment consisted of at least two repetitions. It included 30‘ incubation of cells with 12.5 μg/ml of CASK peptide (abcam), that was confirmed to bind to amyloid precursor protein, neurexins and syndecans in medium without FBS. Subsequent measurement was performed in the culture medium without FBS, with 6.25 μg/ml for each cell line to assure effective syndecans blocking over the whole course of experiment. Probes were calibrated as described in chapter 3.1.3. The divalent ions role in binding process was, as previously, examined with 1 mM EDTA in 10 mM HEPES in PBS. In the EDTA experiment, cells were incubated for 30’ with 1 mM EDTA in 10 mM HEPES in PBS and assessed as fast as possible before they begin to detach from the surface. In each medium the collected grids of points denoted

as a "map" were 8 x 8 points (10 μm x 10 μm) in case of TR400 probe and 10 x 10 points (8 μm x 8 μm) for BL. Maps were collected over the same area for the set of velocities: 0.5 μm/s, 1 μm/s, 2 μm/s,3 μm/s, 5 μm/s, 7 μm/s, 10 μm/s, 15 μm/s and 20 μm/s. This range translated into loading rates in a range from tenths to tenths of thousands pN/s. Half of the measurements was performed ascending velocity and half descending. The range of 0.5 μm/s to 20 μm/s was proven to be optimal for the GRGDTP unbinding experiment and for the sake of consistency was maintained as in chapter 5. Very low force of 0.25 nN (BL) to 0.35 nN (TR400) was applied on the surface of examined cells causing no visible deterioration nor disassembly of the structures during multiple measurements in approximately the same spot.

Data analysis The EWLC model (3.5) derived system spring constant k_{sys} significantly rises the robustness of scrutiny due to receptor immersion in an elastic membrane resulting in altered system spring constant. Moreover, it was recommended by O. Dudko in her work to use WLC model since the DHS model is based on WLC model derived system constants [50]. However, the EWLC model application in living cells data analyse itself significantly rises the quality of obtained result by lowering systematic errors. The syndecan (like any other membrane integral receptor) is not infinitely small object on a flat surface, but has its dimensions, conformation and localization in a membrane, which also vary and thus may impact the effective k_{sys} value. Thus, the procedure of data analysis is exactly the same as in previous chapter 5 for the BE model fitting. Then, the unbinding forces were plotted against the corresponding loading rate values and the equation 43 was fitted in self-written Python program using ODRPACK [13] for the DHS anlysis. The merge of all three probes for each sample is justified because data overlap so well that in some cases the points corresponding to first and second probe are barely visible in figures 21 and 22 because they are covered with data collected with the third probe. Figures 21 and 22 show also higher discrepancies in data points obtained for the TCC cell lines T24 and HTB-5.

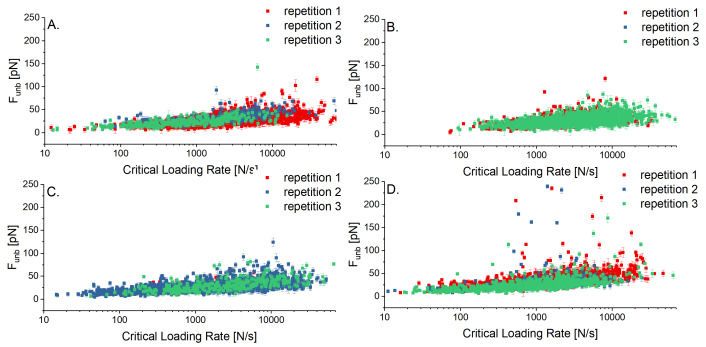

Figure 21: The specific unbinding events collected with TR400 probes functionalized with MabSDC-1 against A. HTB-9, B. HT1376, C. T24, and D. HTB-5 cell lines and corresponding loading rates. The three repetitions are showcased.

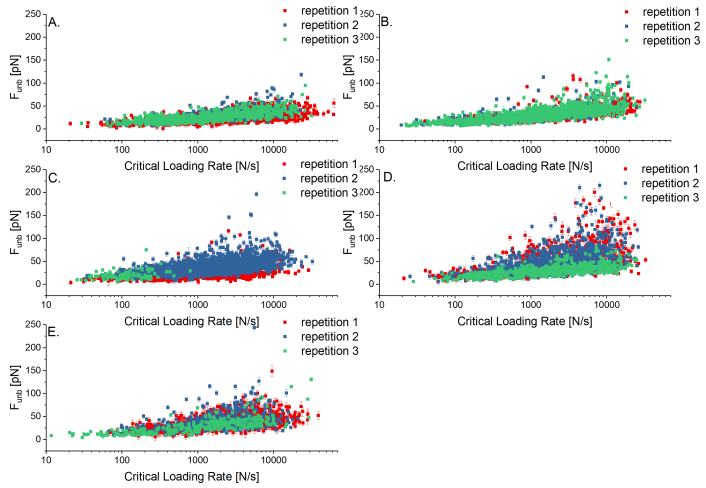

Figure 22: The specific unbinding events collected with BL probes functionalized with MabSDC-4 against A. HCV29, B. HTB-9, C. HT1376, D. T24 and E. HTB-5 cell lines and corresponding loading rates. In case of repetition 3 for HT1376, the measurements were performed only with 0.5 μm/s velocity for the sake of keeping consistently 25 maps per velocity.

6.3 Monoclonal antibodies unbinding energy landscape parameters determination

Bell-Evans model The DFS data require specific processing in order to obtain the full information about energy landscape parameters and not only a comparison between the adhesion forces. The Bell-Evans and Duko-Hummer-Szabo are two models proposed to describe force spectroscopy data. The BE model was examined firstly. Henceforth, they are compared and evaluated as the possible descriptors of highly specific monoclonal antibodies interactions with intact living cells on the example of MabSDC-1 and MabSDC-4 and distinct bladder cancer cell lines. Importantly, the data provide information about the nanomechanical characteristic of syndecans monoclonal antibodies interactions with cell lines of choice.

The results of experiments performed with either TR400 or BL functionalized with MabSDC-1 against the surface of HTB-5 cells show that distinct applied force values, mechanical parameters of probes and their geometries make it impossible to robustly compare results obtained with two distinct probes types. The fitting results are significantly different as presented in Table 4 and in the Fig. 23.

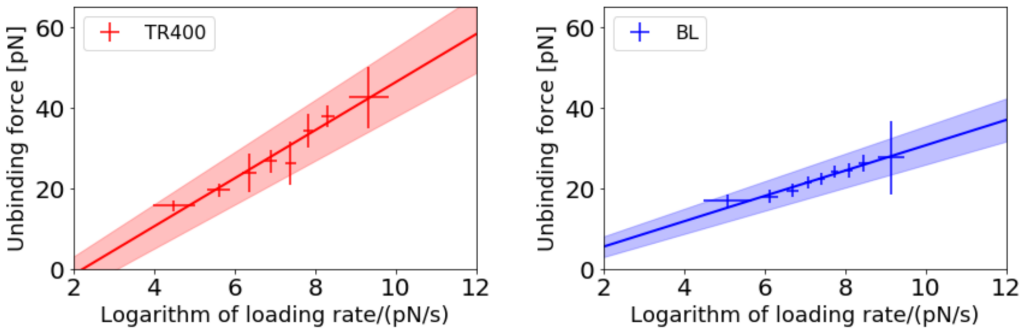

Figure 23: The BE model fit to the DFS data obtained using TR400 and BL probes functionalized with MabSDC-1 against the surface of HTB-5 cells.

Table 4: The parameters derived from BE model fit to the DFS data obtained with the TR400 and the BL probes both functionalized with MabSDC-1. The x_b, k_0 and τ_0 parameters characterise the energy landscape parameters according to Bell-Evans model.

probe type	a	b	x_b [pm]	k_0 [1/s]	τ_0 [ms]
TR400	5.96 ± 0.52	-13.3 ± 3.5	694 ± 61	1.55±0.29	640 ± 120
BL	3.14 ± 0.28	-0.78 ± 2.1	1320 ± 120	0.41 ± 0.13	2450 ± 750

In liquids the hydrodynamic drag on the pulling spring affects the probes motion and, hence the values of obtained unbinding forces. Probes may have distinct response to loading with constant velocity due to different off-set forces (250 pN by BL and 350 pN by TR400), hydrodynamic drag acting on a distinct shape of a cantilever (rectangular 100 μm BL or triangular 200 μm TR400), and differences in response to thermal fluctuations [128]. The BL is best suitable for obtaining a weak force in a small-loading rate measurement, while stiffer like for example TR400 is better for a measurement of stronger force with larger loading rate [128, 199]. Additionally, the BL probe was shaped in a form of cleavage being an integral part of a cantilever. Such approach allowed to minimize hydrodynamic drag in a system. Thus, the comparison between MabSDC-1 decorated TR400 and MabSDC-4 functionalized BL were excluded from this work. The result of DFS experiments performed on four distinct bladder cancer cell lines are presented in the Fig. 24 and in the Table 5. None of the obtained values of x_b, k_0, τ_0 for the probe functionalized with MabSDC-1 are significantly different between HTB-9 and HT1376 The parameters are all significantly different for T24 and HTB-5 while T24 shows way better pronounced differences. Both T24 and HTB-5 characterize with longer bond lifetime, but the direction of bond length changes is different for those two cell lines. The HCV29 cells were not taken in account for this comparison because the unbinding probabilities revealed in the next section suggested that the concentration of SDC-1 in HCV29 cells is too low to assure a robust energy landscape parameters calculation.

Table 5: The fitting parameters derived from BE model linear fit to the DFS data obtained with the TR400 probes functionalized with MabSDC-1. The a and b denote the linear fit parameters. The x_b, k_0 and τ_0 parameters characterise the energy landscape according to Bell-Evans model. The values marked with an asterisk (*) are not significantly different from the values obtained for grade 2 HTB-9 cells.

cell line	a	b	x_b [pm]	k_0 [1/s]	τ_0 [ms]
HCV29	— ± —	—— ±—	—— ± —	— ± —	— ± —
HTB-9	5.07 ± 0.45	-12.7 ± 3.2	817 ± 73	2.40 ± 0.51	416 ± 89
HT1376	5.29* ± 0.23	-12.9* ± 1.8	783* ± 34	2.15* ± 0.24	465* ± 50
T24	3.97 ± 0.18	-3.88 ± 1.3	1043 ± 47	0.668 ± 0.086	1496 ± 192
HTB-5	5.96 ± 0.52	-13.3* ± 3.5	695 ± 61	1.55 ± 0.29	644 ± 120

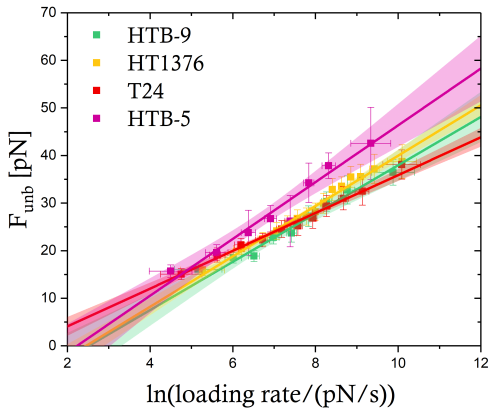

Figure 24: The BE model fit to the DFS data obtained using TR400 probe functionalized with MabSDC-1 against the surface of malignant HTB-9, HT1376, T24, and HTB-5 cells.

In case of MabSDC-4 functionalized probe, the values of x_b, and τ_0 for the probe functionalized with MabSDC-4 present more complicated pattern as shown in Fig. 25 and table 6. The x_b value is significantly different from HCV29 only for T24 cell line, whilst the cell lines of a significantly longer bond lifetime are grade 2 HTB-9 and grade 3 HT1376.

Table 6: Comparison between the parameters derived from BE model linear fit to the DFS data obtained with the BL probes functionalized with MabSDC-4. The a and b denote the linear fit parameters. The x_b, k_0 and τ_0 parameters characterise the energy landscape according to Bell-Evans model. Values that are not statistically significantly different from respective values for HCV29 are marked with an asterisk (*).

cell line	a	b	x_b [pm]	k_0 [1/s]	τ_0 [ms]
HCV29	6.33 ± 0.27	-19.5 ± 2.1	654 ± 28	3.42 ± 0.33	293 ± 28
HTB-9	6.56* ± 0.24	-17.3* ± 1.8	631* ± 23	2.12 ± 0.17	473 ± 37
HT1376	6.62* ± 0.27	-14.0 ± 2.0	625* ± 26	1.24 ± 0.11	804 ± 70
T24	7.92 ± 0.41	-25.5 ± 2.9	523 ± 27	3.14* ± 0.31	319* ± 32
HTB-5	6.82 ± 0.41	-19.4* ± 3.1	659* ± 43	3.47*± 0.50	288* ± 41

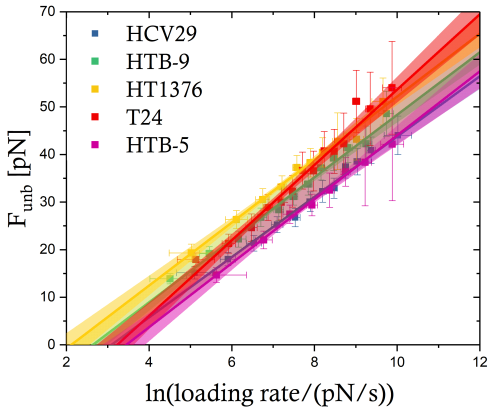

Figure 25: The BE model fit to the DFS data obtained using BL probe functionalized with MabSDC-4 to the surface of non-malignant HCV29 cells and malignant HTB-9, HT1376, T24 and HTB-5 cells.

According to the BE fit results, T24 has longer bond lifetime. Surprisingly, HTB-5 cells energy landscape parameters do not differ from non-malignant HCV29 according to BE model. This tendency is exactly opposite to the one observed in

case of SDC-1 study. The x_b value here again is within the Ångstrom order of magnitude. The k_0 and hence τ_0 are of the order of magnitude previously published and widely acclaimed.

Dudko-Hummer-Szabo model Subsequently, the DHS model was fitted to the same data as described in the previous paragraph in order to compare the results of Bell-Evans model and Dudko-Hummer-Szabo model fitting to experimental data. The model was fitted to the single points for each cell line after merging points obtained in the course of all three repetitions without any previous pre-processing (i.e. the data were not collected in histograms).

Table 7: The parameters derived from DHS model fit to the DFS data obtained with the TR400 probes functionalized with MabSDC-1. The ΔG, x_b, k_0 and τ_0 parameters characterise the energy landscape according to Dudko-Hummer-Szabo model. Values that are not statistically significantly different from respective values for HTB-9 are marked with an asterisk (*)

cell line	ΔG [k_BT]	x_b [pm]	k_0 [1/s]	τ_0 [s]
HCV29	—- ± —	— ± –	— ± —	— ± —
HTB-9	10.18 ± 0.26	1203 ± 43	0.43 ± 0.08	2.34 ± 0.42
HT1376	10.19* ± 0.57	1066 ± 65	0.44* ± 0.10	2.27* ± 0.48
T24	11.85 ± 0.53	1398 ± 85	0.14 ± 0.04	7.34 ± 2.15
HTB-5	9.32 ± 0.45	889 ± 59	0.46* ± 0.11	2.16* ± 0.50

The results suggest that HTB-5 and T24 TCC cell lines have significantly different ΔG and x_b but HTB-5 does not characterizee with altered lifetime related parameters: k_0 nor τ_0. All the malignant cell lines characterize with other x_b than HTB-9. What important the relations between parameters for HTB-5 grade 4 and T24 grade 3 are exactly opposite suggesting different adaptation mechanisms in distinct TCC cells.

Table 8: Comparison between the parameters derived from DHS model fit to the DFS data obtained with the BL probes functionalized with MabSDC-4. The ΔG, x_b, k_0 and τ_0 parameters characterise the energy landscape according to Dudko-Hummer-Szabo model. Values that are not statistically significantly different from respective values for HCV29 are marked with an asterisk (*).

cell line	ΔG [k_BT]	x_b [pm]	k_0 [1/s]	τ_0 [s]
HCV29	9.69 $\pm$ 0.32	980 $\pm$ 44	0.67 $\pm$ 0.13	1.49 $\pm$ 0.29
HTB-9	8.70 $\pm$ 0.22	860 $\pm$ 34	0.60* $\pm$ 0.09	1.67* $\pm$ 0.25
HT1376	10.40* $\pm$ 1.50	768 $\pm$ 80	0.39 $\pm$ 0.12	2.55 $\pm$ 0.77
T24	8.05 $\pm$ 0.30	656 $\pm$ 38	1.03 $\pm$ 0.20	0.97 $\pm$ 0.19
HTB-5	10.62 $\pm$ 0.53	663 $\pm$ 78	0.98 $\pm$ 0.25	1.02 $\pm$ 0.26

In the case of MabSDC-4 studies the ΔG value of HTB-9, T24, HTB-5 that are significantly different from non-malignant cells and HT1376 are not due to the high value of error. Simultaneously, x_b systematically lowers with the metastasis progression and τ_0 is raised in the case of grade 3 and lowered for transitional cell lines. What important there are no statistically significant differences between T24 and HTB-5 cell lines x_b, k_0, and τ_0, the difference between the lines lied in the value of ΔG. The bond lengths range between 6 and 14 Å. The standard van der Waals interaction between two single atoms is between 4-6 Å. Since examined bonds characterize with more complex nature the value appears to be reasonably acceptable and in most cases more probable than in case of BE model, for which the x_b varies around 5-6 Å. Also the value of ΔG equal to several k_BT suggest reasonable result for the case of antigen-antibody binding. The DHS model resulted in significantly higher bond lifetimes however it is hard to predict which values are more reasonable in case of an interaction, which parameters are examined for the first time in living cells. The interactions energy landscapes can be reconstructed schematically according to Krammers theory [80, 84, 118] as shown in Fig 26.

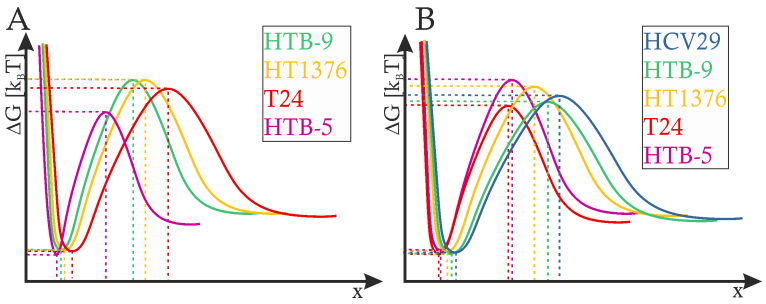

Figure 26: Schematic illustration of reconstructed energy landscapes for the: A. MabSDC-1 and B. MabSDC-4 binding based on DHS energy landscape parameters.

6.4 Interactions blocking and the role of divalent ions in examined interactions

Blocking experiments were performed as described in section 4.1.4 for all cell lines to confirm the specificity and ion dependence of syndecans interactions with their corresponding monoclonal antibodies functionalized probes. The results of a blocking experiment are shown in the figure 27 Aditionally, for MabSDC-4 experiments were repeated twice for HCV29 and HT1376 cell lines in presence of 1mM EDTA in 10 mM HEPES in PBS.

A. B.

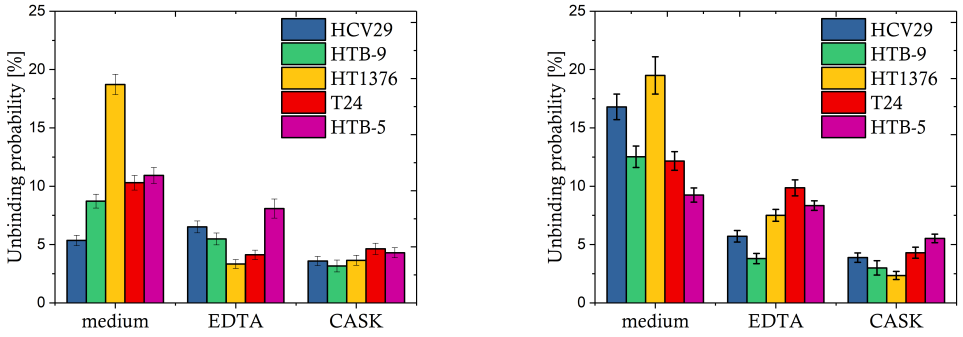

Figure 27: The specific unbinding events probabilities blocking experiment for a probe functionalized with A. MabSDC-1 B. MabSDC-4 to HCV29, HTB-9, HT1376, T24 and HTB-5 cell lines.

Normally the specific antibodies binding probabilities range between 15% up until 30% or in some cases even 50% of all interactions in isolated molecule-antibody DFS conditions [14, 202]. However, the unbinding probabilities of approximately 10% - 20% are fully justifiable due to the steric hindrance of the binding process, and to the low flexibility of the molecules attached to the probe. In the conditions of molecular crowding on the cellular membrane, assuring no additional contact time[11] and low antibody concentration is necessary to maintain high rate of specific to non-specific unbinding events. The specificity of the measurement was confirmed using blocking experiments with CASK peptide. Additionally, there was an approach to block the interactions between syndecans and their monoclonal antibodies by removing divalent ions form the medium. The results of blocking experiments suggest division of malignant cells in two groups depending on unbinding probability changes upon addition of CASK peptide: that of low unbinding probability, that does not change more than 20% after adding CASK peptide and that of high unbinding probability that drops significantly (≈70-80%) upon CASK peptide.

The surprising result of EDTA significantly blocking the syndecans interactions but with distinct efficacy for different cell lines inspired additional, out-of-scope measurement. The DFS experiment with MabSDC-4 on the HTB-5 surface was repeated in the presence of 1 mM Ca^{2+} addition in order to check the impact of divalent ions excess in the process of SDC-4 monoclonal antibodies unbinding. As shown in the Figure 28, there were no significant discrepancies between the two samples. The calcium ions were the ions of choice due to calcium significant role in syndecan function. It is worth to note that after 1 mM Ca^{2+} addition, the histograms of measured unbinding force broadened. This preliminary research can suit as an inspiration for further research.

[11] The time probe is remaining in contact with a surface before retract phase.

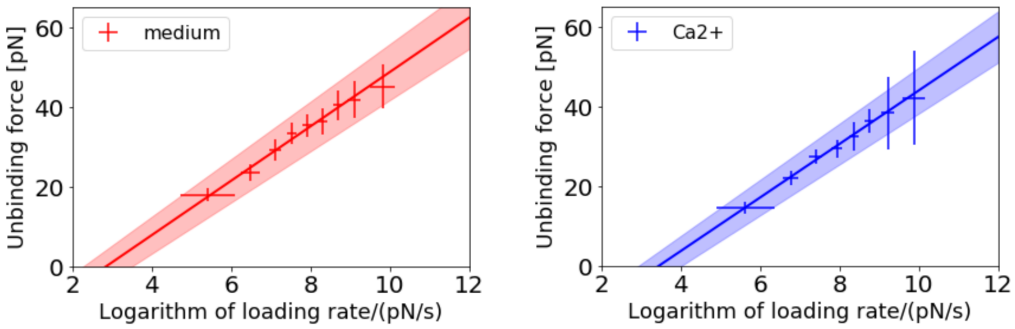

Figure 28: The result of DFS measurements on HTB-5 cells in either pure EMEM or EMEM supplmented with 1 mM Ca^{2+} ions with MabSDC-4 functionalized BL probe. The lines correspond with BE model fit.

6.5 Chapter summary

This chapter addresses the problem of the kinetic of SDC-1 and SDC-4 interactions with their monoclonal antibodies and to what extent the syndecans are force-dependent and force-responding machineries, and how well can they be described by BE and DHS models. The use of monoclonal antibodies highly specific against respectively syndecan-1 or -4 allowed to determine the parameters describing the unbinding energy landscape with high specificity. The measured forces are in a range of 10-150 piconewtons. The antibodies recognition sites bind relatively small amino acid sequences of 50-200 aa as compared to the entire syndecan size.

The data analysis was performed as introduced in previous chapter 5. More specific ligand did not change much in the regard of analysis performance. The additional scrutiny comparing TR400 and BL cantilevers results proved previous assumption that the DFS technique requires careful conditions management [177][12] and the samples measured with distinct cantilevers should not be compared if their geometry and mechanical characteristics differ significantly . Simultaneously, the DHS reconstruction method was applied same as in 5 to the whole spectrum of unbinding forces without prior binning them in histograms. If done otherwise, the results of ΔG for HT1376 and HTB-5 probed with MabSDC-4 decorated probe

[12]Supplementary materials

would value around 9 k_BT with an error of approximately 44 k_BT (results not shown). This confirmed the higher applicability of proposed approach as suggested by Humer and Szabo [91].

There are reports claiming two-fold barrier crossing mechanism in case of binding SDC-1 to MabSDC-1 [84]. The inner barrier is associated with data corresponding to loading rate above 200 nN/s, which was impossible to obtain on the soft surface of intact cells. The above mentioned work also implies the differences of around an order of magnitude in k_0 values between the parameters derived from BE and DHS models. The strong covalent bond lengths range between an order of magnitude of a single C-H bond ($\approx$ 1.09 Å) and C-C bond ($\approx$ 1.54 Å) [209]. The single hydrogen bonds in coiled proteins are expected at the distances of 2.7-3.3 Å [188]. In this work, x_b values vary between 5.5-10.5 Å for BE model and 6.6-14.0 Å for DHS model in living cells. The values of ΔG are lower in case of this study but similarly as in [84] within a range of k_BT that is a reasonable result considering how different is the environment of the two experiments and possible electrostatic impact of other membrane ingredients.

The two examined syndecans have distinct extracellular domains and attach different ligands. Syndecan-1 contains chondroitin (CS) and heparan sulphates (HS) while syndecan-4 is shorter and contains only HS. The details of syndecans role and binding is wider described in section 2.3. Syndecan-4 monomers dimerize or polimerize creating a zone of negative charge on the membrane and thus facilitate interactions with positively charged ligands [73]. Importantly, HS plays crucial role in this process hence being responsible for development, proliferation, cell migration, homeostasis, and involved in disease. CS and HS participate in providing mechanical strength to tissues, since it absorbs water and fill up the space between other ECM proteins. Their properties make them also a potent factor associated with cell adhesion and wound healing. The changes in HS and CS are, together with shredding and syndecans internalization in transitional cells, possible explanations of the distinctions in adhesive energy landscape parameters in different grades of malignancy bladder cancer cells. However, to state it clearly the panel of biological experiments is necessary. The highest unbinding probability

observed in both cases for the grade 3 HT1376 cell line suggests that malignant cells that are not transitional may have developed additional mechanisms rooting them stronger in the surrounding ECM. This particular cell line developed also over twice higher MabSDC-4 τ_0 than the other cell lines according to both BE and DHS models. While interpreting the data it is important to remember about the grade 3 HT1376 cells tendency for clustering and tumourigenesis [159]. In addition, growth factors absorption is highly dependent on SDC-4 - heparan sulphate interaction [25]. For transitional cells the crucial capability is migration through a host system, and henceforth tumorigenesis. These two actions may require opposite mechanisms: one of them loss of ECM adhesions and another better rooting in surrounding ECM. This feature is clearly visible in significant lowering of free energy of MabSDC-1 unbinding in grade 4 transitional HTB-5 bladder carcinoma and MabSDC-4 unbinding in transitional T24 bladder carcinoma. On the other hand, the tendency for T24 binding SDC-1 and HTB-5 binding SDC4 is opposite that suggests more complex relation than just a grade of malignancy dependence. Conformational and/or CS and HS reorganization may occur in distinct cell lines. That leads to preferential unbinding energy lowering for different syndecans. This is also reflected in the results obtained from BE model τ_0 and k_0 parameters, where the tendency of bond lifetime changes is opposite for the two syndecans. The two tested models sometimes result in contradictory conclusions. For example DHS model suggests that for MabSDC-4 x_b consistently lowers with the rise of malignancy while BE results suggest x_b to be altered only for T24. The chnges in x_b can also be a result of HS and CS composition alterations that may affect sterical shape of binding socket. The malignant cells are a difficult, highly inhomogeneous samples to examine. That is also visible in the Figs. 21 and 22 that show higher data dispersion for TCC cell lines.

Nonetheless, monoclonal antibodies characterize with high ligand binding specificity, the nonspecific interactions must be always taken in consideration. The confirmation of measurements robustness is achieved by blocking experiments. The blocking experiments results show that both EDTA and Calcium/calmodulin-associated serine kinase (CASK) peptide lower the unbinding probability for all of

examined cell lines apart from the case of HCV29-MabSDC-1 interaction blocked with EDTA. Additionally, HCV29 characterize with only approximately 5% unbinding probability that suggests very low concentrations of the receptor in non-malignant cells. CASK interacts with syndecans and blocks their functionality [90]. It was originally described as a guanylate kinase however it is a pseudokinase with roles at the cell surface and in the nucleus, where it interacts with the transcription factor TBR1. Syndecans may regulate the balance between the cytoplasmic and nuclear pools of CASK peptide [142]. In general the syndecan-antibody interaction was not confirmed to be dependent on divalent ions in living cells. Another research confirmed in parallel to this one that EDTA can be used as a syndecan interaction blocking agent in isolated systems [84]. There were indications that syndecans and intracellular Ca^{2+} level impact each other. Syndecan-4 controls channels responsible for cytosolic calcium equilibrium in fibroblasts [74]. As proven on the example of *Caenorhabditis elegans* due to being activated with protein kinase C α (a family of serine - and threonine - specific protein kinases activated by calcium) [73]. The dependence between unbinding probability and malignancy grade was varying for a panel of different grade cells. However, the grade 3 HT1376 characterize with the highest both SDC-1 and SDC-4 monoclonal antibody unbinding (and hence binding) probability. The previously reported claim that SDC-4 concentration correlates with the density of stress fibres [214] was not confirmed for the examined bladder cancer cell lines especially in case of SDC-1 in HCV29 cells. Simultaneously, data show a strong drop in unbinding probability as a result of CASK blocking experiment. It was way less pronounced in case of TCC in comparison to non-malignant, grade 2 and grade 3 cells. That would suggest possible mechanisms in transitional cells protecting them from the impact of for example density dependent external regulation [36]. Heparan sulphate conformation is regulated upon contact with divalent ions [101]. That can be a reason of EDTA induced drop in unbinding probability for most of the cell lines but also for an unevenly distributed blocking effectiveness. The research underlines the crucial impact of measurements performed in living structures (cells, tissues) that may impact receptors conformations as opposed to isolated systems. However, it has been

reported that the presence of divalent ions like Mg^{2+}, together with heparan sulphate chains, could maintain appropriate conformation of CS and HS chains, and thus it might increase their accessibility [101]. The adhesive interactions forces depend on conformational state, steric hindrance, geometric factors, and environment ionic force. Metastasis and tumorigenesis are good examples of how the mechanical and kinetic properties of single molecules determine the characteristics of cell adhesion to their environment. Expected reasons of distinct physical parameters of syndecan-4 binding properties include differences in HS structure of membrane syndecan-4. SDC shredding is a potent factor known to regulate tumorigenesis and angiogenesis through growth factors release, impact on the interactions between cancerous cells and blood vessels endothelium and host organ cells. Enzymes cutting HS like for example heparanase may facilitate or block metastasis depending on HS structure and fragments size. In parallel transcriptional regulation of the variety of sulfotransferases post translational editing by 6-O-sulfatases at the cell surface [61]. Until now, the heparanase impact on tumorigenesis studies mainly focused on syndecan-1. However, heparanase has impact on both syndecan-1 and -4 HS shredding[13] [77].

While in human syndecans normally bind to predominantly fibronectin and create complexes with for example $\alpha_5\beta_1$ or $\alpha_V\beta_3$ integrin, the study on artificial antibodies can be relevant in the process of cancer therapies development [7,9,214]. Currently the most important direction in cancer research focuses on improving the safety and comfort of life of treated patients by limiting the outrageous side effects of traditional chemotherapy. The study importance lies also in the direct membrane approaching unavailable for techniques such as Western Blot that give information about the whole volume of cells. The syndecans can be endocytozed from the membrane into the cells where they are unavailable for ECM to bind. These pool of molecules can be detected by expression experiments but are not possible to probe by AFM. This chapter helps to clarify the distinctions between different grades of malignancy bladder carcinomas and poses an inspiration for future biological research in the field. It is also an invaluable example of an impor-

[13]the process of loosing extracellular domain

tance of research on the mechanical functions of highly complex living systems. The final outcome of conformational, compositional and clustering changes that result in altered mechanical parameters occur in the living cells even despite the fact scrutiny was performed on seemingly highly specific system of monoclonal antibody and its ligand. Up to the authors knowledge, there is no procedure developed to mimic these alterations in isolated systems. Thus, it is important to stress that many proteins such as syndecans have a mechanical function so that their kinetics and mechanical stability examination is crucial to fully understand their role.

7 Conclusions

The main research hypothesis of the thesis stands that AFM based DFS energy landscape parameters determination is feasible for cancer cells undergoing malignant transformation. The receptors physical interactions with extracellular matrix (ECM) proteins such as fibronectin and vitronectin in human bladder carcinoma lead to discrepancies in various histological grades of malignancy. These alterations are manifested in distinct cellular adhesive properties, and are strong enough to be measured using single molecule dynamic force spectroscopy on cells cultured *in vitro*. The cells interact with ECM mainly through the nanomechanical interactions governed by a sequence of single ligand-receptor binding and unbinding events rooted in membrane and sub-membrane machinery [44, 86, 105, 149]. Hence, the capability of the DFS to scrutinize complex unbinding forces with resolution down to several pN offers the chance to assess nanomechanical basis of specific recognition. The single molecule force spectroscopy in DFS mode allows to quantify a relation between the most probable unbinding force of a single molecular complex unbinding and the loading rate. It provides data for energy landscape determination. The thesis was confirmed under the condition of careful sample preparation, measurement and data analysis procedure as presented in this work. Simultaneously, observed changes are not simply proportional to the malignancy grade of examined cell lines. Robust, systematized ,and quantitative energy landscape parameters analysis of integrins' and syndecans' of choice interactions on the surface of different grades of malignancy bladder cancer cells was performed in order to test the hypothesis. The HCV29 non-malignant cells of ureter suited as a control sample. The aim of this work was obtained in several steps. Firstly, the technique of systematic and robust measurements included measurement in medium without FBS, specific procedure of tip functionalization, and very low indentation force that greatly limited the procedure impact on cells. Possible scanner thermal drift and sample ageing related effects were compensated by performing measurements from the highest to the lowest probing speed, and oppositely in turns. The functionalization of a probe with glutaraldehyde, a short molecule not qualified as a crosslinker, provided lowering in degrees of freedom

number. The ability to recognize specific events without an elastic crosslinker was restored thanks to the use of EWLC model. It also provided an exact information about local elastic properties of a system in each point and allowed more reliable loading rates determination. This was beneficial due to the great plasticity and anisotropy of cellular membranes. The blocking experiments verified and confirmed the specificity of measured unbinding events. Simultaneously, blocking experiments suited to obtain additional information about distinctions between different cell lines behaviour. Henceforth, the two potent theoretical models were fitted to the experimental data in order to provide the complex analysis of obtained result and energy landscape parameters calculation. All the procedures were performed on two cell lines: HCV29 and HT1376 probed with GRGDTP hexapeptide containing RGD binding motif and FN4-12 module containing LDV, PHSRN and RGD binding sites but lacking syndecan binding HepII domain. In that case, blocking experiments were performed with GRGD peptide in medium, vitronectin in medium and EDTA in HEPES in PBS. The comparison of GRGDTP unbinding forces distributions before and after interactions blocking with EDTA suggest that despite the unbinding probability drops over fourfold, the mechanical unbinding energy landscape parameters remain unchanged. The BE and DHS results showed significantly distinct nanomechanical unbinding properties of both the GRGDTP peptide and FN4-12 from the integrin receptors present on a membrane of both studied cell types. The second panel was performed with monoclonal antibodies against syndecan-1 and syndecan-4 on five cell lines: HCV29, HTB-9, HT1376, T24 and HTB-5 originating from different stages of progression from non-malignant epithelium (HCV29) up to transitional grade 4 carcinoma (HTB-5). The blocking experiments were performed with CASK peptide in medium blocking syndecans activity and EDTA in HEPES in PBS chelating divalent ions. The EDTA experiments allowed to obtain an insight in the behaviour of cells in the absence of divalent ions in the membrane. This scrutiny was limited to 10 μm/s retrct velocity due to reasons associated with cells partially detaching from the Petri dish surface in the absence of divalent ions. This enforced resignation from significantly more time consuming blocking experiments with 2 μm/s velocity. The scrutiny was

each time performed on the surface of living cells in their optimal medium as suggested by provider and without FBS. The valuable results were obtained in course of the blocking experiments. Although blocking experiments with CASK peptide are highly effective in case of non-transitional cells, the TCC blocked with CASK preserve up to 70% of initial unbinding probability. This result can suit as a catalyst for future more biologically related experiments scrutinizing the transitional cells ability to bypass the mechanism in which CASK blocks syndecans activity. Although the EDTA caused lowering of unbinding probability in most cell lines, it was not as effective as CASK likely due to some divalent ions remaining in the membranes of still attached cells. Additionally, the experiments on HCV29 and HTB-5 cell lines in presence and in absence of a1 mM Ca^{2+} ddition suggested no impact of calcium ion supplementation on the value of unbinding force.

Obtained results suited to conclude that the hypothesis was confirmed with some minor restrictions. The analysis allowed to compare the robustness and applicability of both models in biological complexes characterization on living cells. The DHS model proved the difference only between the free energy of unbinding in the case of FN4-12 while according to BE model the bond lifetime differed in that case. Both BE and DHS models agreed that in case of GRGDTP binding the only statistically significant difference between energy landscape parameters for HCV29 and HT1376 was the bond length. According to DHS model based x_b of syndecan-1 and syndecan-4 monoclonal antibody unbinding differ between non-transitional bladder carcinoma cells (HTB-9) and that of the non-malignant cells of ureter (HCV29) and the transitional bladder cancer cell lines. In case of MabSDC-1 unbinding the free energy is significantly different between grade 2 cells and both transitional cell lines. In case of MabSDC-4 only the HT1376 cells unbinding free energy does not differ significantly from he value correspondent to non-malignant cells, probably as a result of higher error value. Although the BE derived energy landscape parameters significantly differed between grade 2 cells and TCC lines, they appeared way less consistent for MabSDC-4 measurement derived parameters. The Bell-Evans and the Dudko-Hummer-Szabo models essentially differ in an approach to unbinding dynamics. BE model assumes that under

pulling force F along the coordinate x the free energy changes following: $G^*=G_0$-Fx_b, while according to DHS $G^*=G_0$-F_x where x is not equal to the bond length in the absence of force x_b. BE model assumed for infinite energy barrier, while DHS model allows more realistic potential shape determination. In this work, potential barrier was modelled as linear-cubic. This approach was suggested to be favourable in the original work by the model creators because it fits better in the case of ligand-receptor complex unbinding with AFM probe. The original Bell's theory models the energy landscape of separation energy between two living cells considered as viscoelastic fluid mosaic bodies with a biphase plasma membrane and receptors immersed in it. Even for forces independent of time, BE model is valid only in case of diffusive barrier crossing with small forces [44]. However, due to BE models simplicity, it is regarded for stating whether there are significant differences between two data sets. It is concluded that each time both models may provide insight in DFS data analysis. However, the Dudko-Hummer-Szabo model characterizes with greater robustness and sensitivity. Simultaneously, the impact of application of even relatively small forces with AFM probe should not remain without impact on mechanical response of single receptors. The work presents also the importance of consistency and careful choice of AFM probes.

The work proves Dynamic Force Spectroscopy to be a powerful tool to probe the stability and near-equilibrium specific complexes unbinding events on the surface of living cells in the conditions where the membrane receptors are as close to native as possible outside human body. The energy landscape parameters differences revealed from this research reflect the general stability of the membrane ECM receptors, including contributions from hydrophobic interactions, hydrogen bonds, and Van der Waals forces. Future opportunities may include the determination of individual contributions of different types of molecular interactions that guide the unbinding, and functional condition of membrane proteins in the presence and in the absence of factors such as divalent ions and distinct ECM components.

8 Appendix

List of Figures

List of Tables

References

[1] B. D. Adair, J. P. Xiong, C. Maddock, S. L. Goodman, M. A. Arnaout, and M. Yeager. Three-dimensional EM structure of the ectodomain of integrin $\alpha V\beta 3$ in a complex with fibronectin. *J. Cell Biol.*, 168(7):1109–1118, mar 2005.

[2] D. Alsteens, M. Pfreundschuh, C. Zhang, P. M. Spoerri, S. R. Coughlin, B. K. Kobilka, and D. J. Müller. Imaging G protein-coupled receptors while quantifying their ligand-binding free-energy landscape. *Nat. Methods*, 12(9):845–851, aug 2015.

[3] C. Ang, A. F. Chambers, A. B. Tuck, E. Winquist, and J. I. Izawa. Plasma osteopontin levels are predictive of disease stage in patients with transitional cell carcinoma of the bladder. *BJU Int.*, 96(6):803–805, oct 2005.

[4] W. S. Argraves, S. Suzuki, H. Arai, K. Thompson, M. D. Pierschbacher, and E. Ruoslahti. Amino acid sequence of the human fibronectin receptor. *J. Cell Biol.*, 105(3):1183–1190, 1987.

[5] M. A. Arnaout, S. L. Goodman, and J.-P. Xiong. Coming to grips with integrin binding to ligands. *Curr. Opin. Cell Biol.*, 14(5):641–51, oct 2002.

[6] M. Barczyk, S. Carracedo, and D. Gullberg. Integrins. *Cell Tissue Res.*, 339(1):269–280, jan 2010.

[7] M. D. Bass, M. R. Morgan, and M. J. Humphries. Integrins and syndecan-4 make distinct, but critical, contributions to adhesion contact formation. *Soft Matter*, 3(3):372–376, 2007.

[8] I. B. Bayer-Garner and B. R. Smoller. The expression of syndecan-1 is preferentially reduced compared with that of E-cadherin in acantholytic squamous cell carcinoma. *J. Cutan. Pathol.*, 28(2):83–89, feb 2001.

[9] D. M. Beauvais and A. C. Rapraeger. Syndecan-1-mediated cell spreading requires signaling by alphavbeta3 integrins in human breast carcinoma cells. *Exp. Cell Res.*, 286(2):219–32, jun 2003.

[10] G. I. Bell. Models for the specific adhesion of cells to cells. *Science*, 200(4342):618–627, 1978.

[11] K. A. Beningo and Y. L. Wang. Fc-receptor-mediated phagocytosis is regulated by mechanical properties of the target. *J. Cell Sci.*, 115(4):849–856, feb 2002.

[12] G. Binnig, C. F. Quate, and C. Gerber. Atomic force microscope. *Phys. Rev. Lett.*, 56(9):930–933, 1986.

[13] P. Boggs. User's reference guide for odrpack version 2.01 software for weighted orthogonal distance regression. `https://docs.scipy.org/doc/external/odrpack_guide.pdf`, 1992. 2019-08-13.

[14] B. Bonanni, A. S. Kamruzzahan, A. R. Bizzarri, C. Rankl, H. J. Gruber, P. Hinterdorfer, and S. Cannistraro. Single molecule recognition between cytochrome C 551 and gold-immobilized azurin by force spectroscopy. *Biophys. J.*, 89(4):2783–2791, 2005.

[15] M. Bouaouina, Y. Lad, and D. A. Calderwood. The N-terminal domains of talin cooperate with the phosphotyrosine binding-like domain to activate $\beta 1$ and $\beta 3$ integrins. *J. Biol. Chem.*, 283(10):6118–6125, mar 2008.

[16] P. C. Brooks, R. L. Klemke, S. Schön, J. M. Lewis, M. A. Schwartz, and D. A. Cheresh. Insulin-like growth factor receptor cooperates with integrin $\alpha v \beta 5$ to promote tumor cell dissemination in vivo. *J. Clin. Invest.*, 99(6):1390–1398, mar 1997.

[17] L. F. Brown, B. Berse, L. Van de Water, A. Papadopoulos-Sergiou, C. A. Perruzzi, E. J. Manseau, H. F. Dvorak, and D. R. Senger. Expression and distribution of osteopontin in human tissues: Widespread association with luminal epithelial surfaces. *Mol. Biol. Cell*, 3(10):1169–1180, 1992.

[18] D. R. Brumley, M. Willcox, and J. E. Sader. Oscillation of cylinders of rectangular cross section immersed in fluid. *Phys. Fluids*, 22(5):1–15, 2010.

[19] C. A. Buck and A. F. Horwitz. Cell surface receptors for extracellular matrix molecules. *Annu. Rev. Cell Biol.*, 3:179–205, 1987.

[20] H. J. Butt and M. Jaschke. Calculation of thermal noise in atomic force microscopy. *Nanotechnology*, 6(1):1–7, 1995.

[21] T. V. Byzova, C. K. Goldman, N. Pampori, K. A. Thomas, A. Bett, S. J. Shattil, and E. F. Plow. A mechanism for modulation of cellular responses to VEGF: Activation of the integrins. *Mol. Cell*, 6(4):851–860, 2000.

[22] F. Caccavari, D. Valdembri, C. Sandri, F. Bussolino, and G. Serini. Integrin signaling and lung cancer. *Cell Adh. Migr.*, 4(1):124–129, jan 2010.

[23] B. Cappella and G. Dietler. Force-distance curves by atomic force microscopy. *Surf. Sci. Rep.*, 34(1-3):1–3, 1999.

[24] C. V. Carman and T. A. Springer. Integrin avidity regulation: Are changes in affinity and conformation underemphasized? *Curr. Opin. Cell Biol.*, 15(5):547–556, 2003.

[25] L. Caseli, R. P. Cavalheiro, H. B. Nader, and C. C. Lopes. Probing the interaction between heparan sulfate proteoglycan with biologically relevant molecules in mimetic models for cell membranes: A Langmuir film study. *Biochim. Biophys. Acta - Biomembr.*, 1818(5):1211–1217, may 2012.

[26] W. T. Chen, E. Hasegawa, T. Hasegawa, C. Weinstock, and K. M. Yamada. Development of cell surface linkage complexes in cultured fibroblasts. *J. Cell Biol.*, 100(4):1103–1114, apr 1985.

[27] X. Chen, H. Zhao, C. Chen, J. Li, J. He, X. Fu, and H. Zhao. The HPA/SDC1 axis promotes invasion and metastasis of pancreatic cancer cells by activating EMT via FGF2 upregulation. *Oncol. Lett.*, 19(1):211–220, 2020.

[28] Y. Chen, H. Lee, H. Tong, M. Schwartz, and C. Zhu. Force regulated conformational change of integrin α V β 3. *Matrix Biol.*, 60-61:70–85, jul 2017.

[29] R. C. Cherny, M. A. Honan, and P. Thiagarajan. Site-directed mutagenesis of the arginine-glycine-aspartic acid in vitronectin abolishes cell adhesion. *J. Biol. Chem.*, 268(13):9725–9, may 1993.

[30] A. Chigaev, A. M. Blenc, J. V. Braaten, N. Kumaraswamy, C. L. Kepley, R. P. Andrews, J. M. Oliver, B. S. Edwards, E. R. Prossnitz, R. S. Larson, and L. A. Sklar. Real time analysis of the affinity regulation of α 4-integrin: The physiologically activated receptor is intermediate in affinity between resting and Mn2+ or antibody activation. *J. Biol. Chem.*, 276(52):48670–48678, dec 2001.

[31] A. Chigaev, G. Zwartz, S. W. Graves, D. C. Dwyer, H. Tsuji, T. D. Foutz, B. S. Edwards, E. R. Prossnitz, R. S. Larson, and L. A. Sklar. $\alpha 4 \beta 1$ integrin affinity changes govern cell adhesion. *J. Biol. Chem.*, 278(40):38174–38182, oct 2003.

[32] D. Choquet, D. P. Felsenfeld, and M. P. Sheetz. Extracellular matrix rigidity causes strengthening of integrin- cytoskeleton linkages. *Cell*, 88(1):39–48, jan 1997.

[33] J. S. Chung, M. Tomihari, K. Tamura, T. Kojima, P. D. Cruz, and K. Arizumi. The DC-HIL ligand syndecan-4 is a negative regulator of T-cell alloreactivity responsible for graft-versus-host disease. *Immunology*, 138(2):173–182, feb 2013.

[34] J. P. Cleveland, S. Manne, D. Bocek, and P. K. Hansma. A nondestructive method for determining the spring constant of cantilevers for scanning force microscopy. *Rev. Sci. Instrum.*, 64(2):403–405, feb 1993.

[35] H. R. Contreras, R. A. Ledezma, J. Vergara, F. Cifuentes, C. Barra, P. Cabello, I. Gallegos, B. Morales, C. Huidobro, and E. A. Castellón. The expression of syndecan-1 and -2 is associated with Gleason score and epithelial-

mesenchymal transition markers, E-cadherin and β-catenin, in prostate cancer. *Urol. Oncol. Semin. Orig. Investig.*, 28(5):534–540, sep 2010.

[36] G. M. Cooper. *The Cell: A Molecular Approach. The Development and Causes of Cancer*. Sinauer Associates, 2nd edition edition, 2000.

[37] O. Corporation. Biolever. `http://probe.olympus-global.com/en/product/bl_rc150vb_hw`, 2018. 2020-02-23.

[38] O. Corporation. Omcl-tr400psa. `http://probe.olympus-global.com/en/product/omcl_tr400psa_hw`, 2018. 2010-02-23.

[39] D. Courter, H. Cao, S. Kwok, C. Kong, A. Banh, P. Kuo, D. M. Bouley, C. Vice, O. T. Brustugun, N. C. Denko, A. C. Koong, A. Giaccia, and Q. T. Le. The RGD domain of human osteopontin promotes tumor growth and metastasis through activation of survival pathways. *PLoS One*, 5(3), mar 2010.

[40] R. Cox, F. Josse, S. M. Heinrich, O. Brand, and I. Dufour. Characteristics of laterally vibrating resonant microcantilevers in viscous liquid media. *J. Appl. Phys.*, 111(1), jan 2012.

[41] C. H. Damsky, K. A. Knudsen, D. Bradley, C. A. Buck, and A. F. Horwltz. Distribution of the cell substratum attachment (csat) antigen on myogenic and fibroblastic cells in culture. *J. Cell Biol.*, 100(5):1528–1539, may 1985.

[42] G. E. Davis. Affinity of integrins for damaged extracellular matrix: αvβ3 binds to denatured collagen type I through RGD sites. *Biochem. Biophys. Res. Commun.*, 182(3):1025–1031, feb 1992.

[43] H. C. de Boer, K. T. Preissner, B. N. Bouma, and P. G. de Groot. Binding of vitronectin-thrombin-antithrombin III complex to human endothelial cells is mediated by the heparin binding site of vitronectin. *J. Biol. Chem.*, 267(4):2264–8, feb 1992.

[44] M. Dembo, D. C. Torney, K. Saxman, and D. Hammer. The reaction-limited kinetics of membrane-to-surface adhesion and detachment. *Proc. R. Soc. B Biol. Sci.*, 234(1274):55–83, 1988.

[45] J. S. Desgrosellier and D. A. Cheresh. Integrins in cancer: Biological implications and therapeutic opportunities. *Nat. Rev. Cancer*, 10(1):9–22, jan 2010.

[46] M. E. Doerr and J. I. Jones. The roles of integrins and extracellular matrix proteins in the insulin- like growth factor I-stimulated chemotaxis of human breast cancer cells. *J. Biol. Chem.*, 271(5):2443–2447, feb 1996.

[47] X. Dong, N. E. Hudson, C. Lu, and T. A. Springer. Structural determinants of integrin β-subunit specificity for latent TGF-β. *Nat. Struct. Mol. Biol.*, 21(12):1091–1096, dec 2014.

[48] O. K. Dudko, A. E. Filippov, J. Klafter, and M. Urbakh. Beyond the conventional description of dynamic force spectroscopy of adhesion bonds. *Proc. Natl. Acad. Sci. U. S. A.*, 100(20):11378–11381, sep 2003.

[49] O. K. Dudko, G. Hummer, and A. Szabo. Intrinsic rates and activation free energies from single-molecule pulling experiments. *Phys. Rev. Lett.*, 96(10), 2006.

[50] O. K. Dudko, G. Hummer, and A. Szabo. Theory, analysis, and interpretation of single-molecule force spectroscopy experiments. *Proc. Natl. Acad. Sci. U. S. A.*, 105(41):15755–15760, oct 2008.

[51] F. Echtermeyer, M. Streit, S. Wilcox-Adelman, S. Saoncella, F. Denhez, M. Detmar, and P. Goetinck. Delayed wound repair and impaired angiogenesis in mice lacking syndecan-4. *J. Clin. Invest.*, 107(2):R9–R14, jan 2001.

[52] J. Emsley, C. G. Knight, R. W. Farndale, M. J. Barnes, and R. C. Liddington. Structural basis of collagen recognition by integrin $\alpha 2\beta 1$. *Cell*, 101(1):47–56, mar 2000.

[53] E. Evans. Probing the Relation Between Force—Lifetime—and Chemistry in Single Molecular Bonds. *Annu. Rev. Biophys. Biomol. Struct.*, 30(1):105–128, jun 2001.

[54] E. Evans, A. Leung, D. Hammer, and S. Simon. Chemically distinct transition states govern rapid dissociation of single L-selectin bonds under force. *Proc. Natl. Acad. Sci. U. S. A.*, 98(7):3784–3789, mar 2001.

[55] E. Evans and K. Ritchie. Dynamic strength of molecular adhesion bonds. *Biophys. J.*, 72(4):1541–1555, 1997.

[56] E. A. Evans and K. Ritchie. Strength of a weak bond connecting flexible polymer chains. *Biophys. J.*, 76(5):2439–2447, 1999.

[57] C. Y. Fears, C. L. Gladson, and A. Woods. Syndecan-2 is expressed in the microvasculature of gliomas and regulates angiogenic processes in microvascular endothelial cells. *J. Biol. Chem.*, 281(21):14533–14536, may 2006.

[58] E. L. Florin, V. T. Moy, and H. E. Gaub. Adhesion forces between individual ligand-receptor pairs. *Science*, 264(5157):415–417, 1994.

[59] G. for WHO Inernational Agency of Reaserch on Cancer data. Bladder fact sheet. `http://gco.iarc.fr/today/data/factsheets/cancers/30-Bladder-fact-sheet.pdf`, 2018. 2019-09-10.

[60] A. L. Frelinger, I. Cohen, E. F. Plow, M. A. Smith, J. Roberts, S. C. Lam, and M. H. Ginsberg. Selective inhibition of integrin function by antibodies specific for ligand-occupied receptor conformers. *J. Biol. Chem.*, 265(11):6346–52, apr 1990.

[61] M. A. Frese, F. Milz, M. Dick, W. C. Lamanna, and T. Dierks. Characterization of the human sulfatase Sulf1 and its high affinity heparin/heparan sulfate interaction domain. *J. Biol. Chem.*, 284(41):28033–28044, oct 2009.

[62] J. C. Friedland, M. H. Lee, and D. Boettiger. Mechanically activated integrin switch controls $\alpha 5 \beta$ 1 function. *Science*, 323(5914):642–644, jan 2009.

[63] J. Friedrichs, A. Manninen, D. J. Muller, and J. Helenius. Galectin-3 regulates integrin $\alpha 2\beta 1$- mediated adhesion to collagen-I and -IV. *J. Biol. Chem.*, 283(47):32264–32272, nov 2008.

[64] J. Friedrichs, J. M. Torkko, J. Helenius, T. P. Teräväinen, J. Füllekrug, D. J. Muller, K. Simons, and A. Manninen. Contributions of galectin-3 and -9 to epithelial cell adhesion analyzed by single cell force spectroscopy. *J. Biol. Chem.*, 282(40):29375–29383, oct 2007.

[65] J. Gailit and E. Ruoslahti. Regulation of the fibronectin receptor affinity by divalent cations. *J. Biol. Chem.*, 263(26):12927–32, sep 1988.

[66] C. G. Galbraith, K. M. Yamada, and M. P. Sheetz. The relationship between force and focal complex development. *J. Cell Biol.*, 159(4):695–705, nov 2002.

[67] N. D. Gallant, K. E. Michael, and A. J. García. Cell adhesion strengthening: Contributions of adhesive area, integrin binding, and focal adhesion assembly. *Mol. Biol. Cell*, 16(9):4329–4340, sep 2005.

[68] R. Gallo, C. Kim, R. Kokenyesi, N. S. Adzick, and M. Bernfield. Syndecans-1 and -4 are induced during wound repair of neonatal but not fetal skin. *J. Invest. Dermatol.*, 107(5):676–683, 1996.

[69] K. K. Ganguly, S. Pal, S. Moulik, and A. Chatterjee. Integrins and metastasis. *Cell Adhes. Migr.*, 7(3):251–261, 2013.

[70] M. Germer, S. M. Kanse, T. Kirkegaard, L. Kjoller, B. Felding-Habermann, S. Goodman, and K. T. Preissner. Kinetic analysis of integrin-dependent cell adhesion on vitronectin. The inhibitory potential of plasminogen activator inhibitor-1 and RGD peptides. *Eur. J. Biochem.*, 253(3):669–674, may 1998.

[71] C. L. Gladson and D. A. Cheresh. Glioblastoma expression of vitronectin and the $\alpha v\beta 3$ integrin: Adhesion mechanism for transformed glial cells. *J. Clin. Invest.*, 88(6):1924–1932, 1991.

[72] S. Gopal, A. Bober, J. R. Whiteford, H. A. Multhaupt, A. Yoneda, and J. R. Couchman. Heparan sulfate chain valency controls syndecan-4 function in cell adhesion. *J. Biol. Chem.*, 285(19):14247–14258, may 2010.

[73] S. Gopal, J. Couchman, and R. Pocock. Redefining the role of syndecans in C. elegans biology. *Worm*, 5(1):e1142042, jan 2016.

[74] S. Gopal, P. Søgaard, H. A. Multhaupt, C. Pataki, E. Okina, X. Xian, M. E. Pedersen, T. Stevens, O. Griesbeck, P. W. Park, R. Pocock, and J. R. Couchman. Transmembrane proteoglycans control stretch-activated channels to set cytosolic calcium levels. *J. Cell Biol.*, 210(7):1199–1211, sep 2015.

[75] F. Grinnell, C. H. Ho, and A. Wysocki. Degradation of fibronectin and vitronectin in chronic wound fluid: Analysis by cell blotting, immunoblotting, and cell adhesion assays. *J. Invest. Dermatol.*, 98(4):410–416, 1992.

[76] J. J. Grootjans, P. Zimmermann, G. Reekmans, A. Smets, G. Degeest, J. Dürr, and G. David. Syntenin, a PDZ protein that binds syndecan cytoplasmic domains. *Proc. Natl. Acad. Sci. U. S. A.*, 94(25):13683–13688, dec 1997.

[77] O. Haddad, E. Guyot, N. Marinval, F. Chevalier, L. Maillard, L. Gadi, C. Laguillier-Morizot, O. Oudar, A. Sutton, N. Charnaux, and H. Hlawaty. Heparanase and syndecan-4 are involved in low molecular weight fucoidan-induced angiogenesis. *Mar. Drugs*, 13(11):6588–6608, nov 2015.

[78] W. Hanley, O. McCarty, S. Jadhav, Y. Tseng, D. Wirtz, and K. Konstantopoulos. Single molecule characterization of P-selectin/ligand binding. *J. Biol. Chem.*, 278(12):10556–10561, mar 2003.

[79] Y. Hata, S. Butz, and T. C. Südhof. CASK: A novel dlg/PSD95 homolog with an N-terminal calmodulin-dependent protein kinase domain identified by interaction with neurexins. *J. Neurosci.*, 16(8):2488–2494, apr 1996.

[80] A. G. Håti, F. L. Aachmann, B. T. Stokke, G. Skjåk-Bræk, and M. Sletmoen. Energy Landscape of Alginate-Epimerase Interactions Assessed by Optical

Tweezers and Atomic Force Microscopy. *PLoS One*, 10(10):e0141237, oct 2015.

[81] K. Hayashi, M. Hayashi, M. Jalkanen, J. H. Firestone, R. L. Trelstad, and M. Bernfield. Immunocytochemistry of cell surface heparan sulfate proteoglycan in mouse tissues. A light and electron microscopic study. *J. Histochem. Cytochem.*, 35(10):1079–1088, 1987.

[82] K. Hayashida, W. C. Parks, and W. P. Pyong. Syndecan-1 shedding facilitates the resolution of neutrophilic inflammation by removing sequestered CXC chemokines. *Blood*, 114(14):3033–3043, 2009.

[83] M. E. Hemler, C. Huang, and L. Schwarz. The VLA protein family. Characterization of five distinct cell surface heterodimers each with a common 130,000 molecular weight β subunit. *J. Biol. Chem.*, 262(7):3300–3309, 1987.

[84] K. Herman, M. Lekka, and A. Ptak. Unbinding Kinetics of Syndecans by Single-Molecule Force Spectroscopy. *J. Phys. Chem. Lett.*, 9(7):1509–1515, apr 2018.

[85] P. Hinterdorfer, W. Baumgartner, H. J. Gruber, K. Schilcher, and H. Schindler. Detection and localization of individual antibody-antigen recognition events by atomic force microscopy. *Proc. Natl. Acad. Sci.*, 93(8):3477–3481, apr 1996.

[86] E. R. Horton, A. Byron, J. A. Askari, D. H. Ng, A. Millon-Frémillon, J. Robertson, E. J. Koper, N. R. Paul, S. Warwood, D. Knight, J. D. Humphries, and M. J. Humphries. Definition of a consensus integrin adhesome and its dynamics during adhesion complex assembly and disassembly. *Nat. Cell Biol.*, 17(12):1577–1587, nov 2015.

[87] E. R. Horton, J. D. Humphries, J. James, M. C. Jones, J. A. Askari, and M. J. Humphries. The integrin adhesome network at a glance. *J. Cell Sci.*, 129(22):4159–4163, 2016.

[88] C. F. Hsieh, B. J. Chang, C. H. Pai, H. Y. Chen, J. W. Tsaia, Y. H. Yi, Y. T. Chiang, D. W. Wang, S. Chi, L. Hsu, and C. H. Lin. Stepped changes of monovalent ligand-binding force during ligand-induced clustering of integrin αIIBβ3. *J. Biol. Chem.*, 281(35):25466–25474, sep 2006.

[89] Y. P. Hsueh and M. Sheng. Regulated expression and subcellular localization of syndecan heparan sulfate proteoglycans and the syndecan-binding protein CASK/LIN-2 during rat brain development. *J. Neurosci.*, 19(17):7415–7425, sep 1999.

[90] Y. P. Hsueh, F. C. Yang, V. Kharazia, S. Naisbitt, A. R. Cohen, R. J. Weinberg, and M. Sheng. Direct interaction of CASK/LIN-2 and syndecan heparan sulfate proteoglycan and their overlapping distribution in neuronal synapses. *J. Cell Biol.*, 142(1):139–151, jul 1998.

[91] G. Hummer and A. Szabo. Kinetics from nonequilibrium single-molecule pulling experiments. *Biophys. J.*, 85(1):5–15, jul 2003.

[92] J. D. Humphries, A. Byron, and M. J. Humphries. Integrin ligands at a glance. *J. Cell Sci.*, 119(19):3901–3903, oct 2006.

[93] R. O. Hynes. Integrins: Versatility, modulation, and signaling in cell adhesion. *Cell*, 69(1):11–25, apr 1992.

[94] H. I. *Theory of STM and Related Scanning Probe Methods.* Springer, 1993.

[95] K. Ishiguro, K. Kadomatsu, T. Kojima, H. Muramatsu, M. Iwase, Y. Yoshikai, M. Yanada, K. Yamamoto, T. Matsushita, M. Nishimura, K. Kusugami, H. Saito, and T. Muramatsu. Syndecan-4 Deficiency Leads to High Mortality of Lipopolysaccharide-injected Mice. *J. Biol. Chem.*, 276(50):47483–47488, dec 2001.

[96] S. Izrailev, S. Stepaniants, M. Balsera, Y. Oono, and K. Schulten. Molecular dynamics study of unbinding of the avidin-biotin complex. *Biophys. J.*, 72(4):1568–1581, 1997.

[97] C. S. Izzard, R. Radinsky, and L. A. Culp. Substratum contacts and cytoskeletal reorganization of BALB/c 3T3 cells on a cell-binding fragment and heparin-binding fragments of plasma fibronectin. *Exp. Cell Res.*, 165(2):320–336, 1986.

[98] M. Jalkanen, A. Rapraeger, S. Saunders, and M. Bernfield. Cell surface proteoglycan of mouse mammary epithelial cells is shed by cleavage of its matrix-binding ectodomain from its membrane-associated domain. *J. Cell Biol.*, 105(6 II):3087–3096, 1987.

[99] M. C. Jones, P. T. Caswell, and J. C. Norman. Endocytic recycling pathways: emerging regulators of cell migration. *Curr. Opin. Cell Biol.*, 18(5):549–57, oct 2006.

[100] W. Kabsch, H. G. Mannherz, D. Suck, E. F. Pai, and K. C. Holmes. Atomic structure of the actin: DNase I complex. *Nature*, 347(6288):37–44, 1990.

[101] M. Kan, F. Wang, M. Kan, B. To, J. L. Gabriel, and W. L. McKeehan. Divalent cations and heparin/heparan sulfate cooperate to control assembly and activity of the fibroblast growth factor receptor complex. *J. Biol. Chem.*, 271(42):26143–26148, 1996.

[102] T. G. Kapp, F. Rechenmacher, S. Neubauer, O. V. Maltsev, E. A. Cavalcanti-Adam, R. Zarka, U. Reuning, J. Notni, H. J. Wester, C. Mas-Moruno, J. Spatz, B. Geiger, and H. Kessler. A comprehensive evaluation of the activity and selectivity profile of ligands for RGD-binding integrins. *Sci. Rep.*, 7, jan 2017.

[103] Kato M Bernfield M. Epithelial cells made deficient in syndecan lose cell surface expression of E-cadherin and Bl-integrins. *J. Cell. Biol*, 111, 1990.

[104] D. Katoh, K. Nagaharu, N. Shimojo, N. Hanamura, M. Yamashita, Y. Kozuka, K. Imanaka-Yoshida, and T. Yoshida. Binding of $\alpha v\beta 1$ and $\alpha v\beta 6$ integrins to tenascin-C induces epithelial–mesenchymal transition-like change of breast cancer cells. *Oncogenesis*, 2(8):e65–e65, aug 2013.

[105] T. Kawauchi. Cell adhesion and its endocytic regulation in cell migration during neural development and cancer metastasis. *Int. J. Mol. Sci.*, 13(4):4564–4590, apr 2012.

[106] M. S. Kellermayer, S. B. Smith, H. L. Granzier, and C. Bustamante. Folding-unfolding transitions in single titin molecules characterized with laser tweezers. *Science*, 276(5315):1112–1116, may 1997.

[107] J. H. Kim and J. Park. Prognostic significance of heme oxygenase-1, S100 calcium-binding protein A4, and syndecan-1 expression in primary non-muscle-invasive bladder cancer. *Hum. Pathol.*, 45(9):1830–1838, 2014.

[108] J. Kiviniemi, M. Kallajoki, I. Kujala, M. T. Matikainen, K. Alanen, M. Jalkanen, and M. Salmivirta. Altered expression of syndecan-1 in prostate cancer. *APMIS*, 112(2):89–97, feb 2004.

[109] J. E. Koda, A. Rapraeger, and M. Bernfield. Heparan sulfate proteoglycans from mouse mammary epithelial cells. Cell surface proteoglycan as a receptor for interstitial collagens. *J. Biol. Chem.*, 260(13):8157–62, jul 1985.

[110] E. Kokkoli, S. E. Ochsenhirt, and M. Tirrell. Collective and single-molecule interactions of alpha5beta1 integrins. *Langmuir*, 20(6):2397–404, mar 2004.

[111] M. H. Korayem, A. Kavousi, and N. Ebrahimi. Dynamic analysis of tapping-mode AFM considering capillary force interactions. *Sci. Iran.*, 18(1 B):121–129, 2011.

[112] A. J. Kulik, M. Lekka, K. Lee, G. Pyka-Fościak, and W. Nowak. Probing fibronectin–antibody interactions using AFM force spectroscopy and lateral force microscopy. *Beilstein J. Nanotechnol.*, 6:1164–1175, may 2015.

[113] Y. Kuwano, O. Spelten, H. Zhang, K. Ley, and A. Zarbock. Rolling on E- or P-selectin induces the extended but not high-affinity conformation of LFA-1 in neutrophils. *Blood*, 116(4):617–624, jul 2010.

[114] D. I. Leavesley, M. A. Schwartz, M. Rosenfeld, and D. A. Cheresh. Integrin β1- and β3-mediated endothelial cell migration is triggered through distinct signaling mechanisms. *J. Cell Biol.*, 121(1):163–170, 1993.

[115] J. O. Lee, P. Rieu, M. A. Arnaout, and R. Liddington. Crystal structure of the A domain from the a subunit of integrin CR3 (CD11 b/CD18). *Cell*, 80(4):631–638, feb 1995.

[116] C. T. Lefort, J. Rossaint, M. Moser, B. G. Petrich, A. Zarbock, S. J. Monkley, D. R. Critchley, M. H. Ginsberg, R. Fässler, and K. Ley. Distinct roles for talin-1 and kindlin-3 in LFA-1 extension and affinity regulation. *Blood*, 119(18):4275–4282, may 2012.

[117] P. P. Lehenkari and M. A. Horton. Single integrin molecule adhesion forces in intact cells measured by atomic force microscopy. *Biochem. Biophys. Res. Commun.*, 259(3):645–650, jun 1999.

[118] M. Lekka. THE USE OF ATOMIC FORCE MICROSCOPY AS A TECHNIQUE FOR THE IDENTIFICATION OF CANCEROUS CELLS. Technical report, The Henryk Niewodniczański Institute of Nuclear Physics Polish Academy of Sciences, 2007.

[119] M. Lekka, D. Gil, W. Dabroś, J. Jaczewska, A. J. Kulik, J. Lekki, Z. Stachura, J. Stachura, and P. Laidler. Characterization of N-cadherin unbinding properties in non-malignant (HCV29) and malignant (T24) bladder cells. *J. Mol. Recognit.*, 24(5):833–842, 2011.

[120] M. Lekka, J. Pabijan, and B. Orzechowska. Morphological and mechanical stability of bladder cancer cells in response to substrate rigidity. *Biochim. Biophys. Acta - Gen. Subj.*, 1863(6):1006–1014, jun 2019.

[121] S. Leppa, M. Mali, H. M. Miettinen, and M. Jalkanen. Syndecan expression regulates cell morphology and growth of mouse mammary epithelial tumor cells (extracellular matrix receptor/differentiation/tumor growth). *Journal Cell Biol.*, 89:932–936, 1992.

[122] F. Li, S. D. Redick, H. P. Erickson, and V. T. Moy. Force measurements of the alpha5beta1 integrin-fibronectin interaction. *Biophys. J.*, 84(2 Pt 1):1252–62, feb 2003.

[123] R. I. Litvinov, V. Barsegov, A. J. Schissler, A. R. Fisher, J. S. Bennett, J. W. Weisel, and H. Shuman. Dissociation of bimolecular αIIbβ3-fibrinogen complex under a constant tensile force. *Biophys. J.*, 100(1):165–173, jan 2011.

[124] R. I. Litvinov, O. V. Gorkun, S. F. Owen, H. Shuman, and J. W. Weisel. Polymerization of fibrin: Specificity, strength, and stability of knob-hole interactions studied at the single-molecule level. *Blood*, 106(9):2944–2951, nov 2005.

[125] R. I. Litvinov, M. Mravic, H. Zhu, J. W. Weisel, W. F. DeGrado, and J. S. Bennett. Unique transmembrane domain interactions differentially modulate integrin αvβ3 and αIIbβ3 function. *Proc. Natl. Acad. Sci. U. S. A.*, 116(25):12295–12300, jun 2019.

[126] B. H. Luo and T. A. Springer. Integrin structures and conformational signaling. *Curr. Opin. Cell Biol.*, 18(5):579–586, oct 2006.

[127] R. Madan, M. B. Smolkin, R. Cocker, R. Fayyad, and M. H. Oktay. Focal adhesion proteins as markers of malignant transformation and prognostic indicators in breast carcinoma. *Hum. Pathol.*, 37(1):9–15, jan 2006.

[128] D. E. Makarov. Communication: Does force spectroscopy of biomolecules probe their intrinsic dynamic properties? *J. Chem. Phys.*, 141(24):241103, dec 2014.

[129] J. F. Marko and E. D. Siggia. Statistical mechanics of supercoiled DNA. *Phys. Rev. E*, 52(3):2912–2938, 1995.

[130] J. F. Marshall and I. R. Hart. The role of αv-integrins in tumour progression and metastasis. *Semin. Cancer Biol.*, 7(3):129–138, 1996.

[131] L. A. Martinez-Lemus, Z. Sun, A. Trache, J. P. Trzeciakowski, and G. A. Meininger. Integrins and regulation of the microcirculation: From arterioles to molecular studies using atomic force microscopy. *Microcirculation*, 12(1):99–112, jan 2005.

[132] D. Marzioni, T. Lorenzi, R. Mazzucchelli, L. Capparuccia, M. Morroni, R. Fiorini, C. Bracalenti, A. Catalano, G. David, M. Castellucci, G. Muzzonigro, and R. Montironi. Expression of basic fibroblast growth factor, its receptors and syndecans in bladder cancer. *Int. J. Immunopathol. Pharmacol.*, 22(3):627–638, 2009.

[133] R. Merkel, P. Nassoy, A. Leung, K. Ritchie, and E. Evans. Energy landscapes of receptor–ligand bonds explored with dynamic force spectroscopy. *Nature*, 397(6714):50–53, jan 1999.

[134] S. K. Mitra and D. D. Schlaepfer. Integrin-regulated FAK-Src signaling in normal and cancer cells. *Curr. Opin. Cell Biol.*, 18(5):516–523, oct 2006.

[135] M. R. Morgan, M. J. Humphries, and M. D. Bass. Synergistic control of cell adhesion by integrins and syndecans. *Nat. Rev. Mol. Cell Biol.*, 8(12):957–969, dec 2007.

[136] A. P. Mould, S. J. Barton, J. A. Askari, S. E. Craig, and M. J. Humphries. Role of ADMIDAS Cation-binding Site in Ligand Recognition by Integrin $\alpha 5\beta 1$. *J. Biol. Chem.*, 278(51):51622–51629, dec 2003.

[137] V. T. Moy, E. L. Florin, and H. E. Gaub. Intermolecular forces and energies between ligands and receptors. *Science*, 266(5183):257–259, 1994.

[138] K. Mythreye and G. C. Blobe. Proteoglycan signaling co-receptors: Roles in cell adhesion, migration and invasion. *Cell. Signal.*, 21(11):1548–1558, nov 2009.

[139] N. Nishida, C. Xie, M. Shimaoka, Y. Cheng, T. Walz, and T. A. Springer. Activation of Leukocyte $\beta 2$ Integrins by Conversion from Bent to Extended Conformations. *Immunity*, 25(4):583–594, oct 2006.

[140] M. P. O'Connell, J. L. Fiori, E. K. Kershner, B. P. Frank, F. E. Indig, D. D. Taub, K. S. Hoek, and A. T. Weeraratna. Heparan sulfate proteoglycan modulation of Wnt5A signal transduction in metastatic melanoma cells. *J. Biol. Chem.*, 284(42):28704–28712, oct 2009.

[141] Y. J. Oh, M. Hubauer-Brenner, H. J. Gruber, Y. Cui, L. Traxler, C. Siligan, S. Park, and P. Hinterdorfer. Curli mediate bacterial adhesion to fibronectin via tensile multiple bonds. *Sci. Rep.*, 6, sep 2016.

[142] N. Ojeh, V. Pekovic, C. Jahoda, and A. Määttä. The MAGUK-family protein CASK is targeted to nuclei of the basal epidermis and controls keratinocyte proliferation. *J. Cell Sci.*, 121(16):2705–2717, aug 2008.

[143] E. Österlund, I. Eronen, K. Österlund, and M. Vuento. Secondary Structure of Human Plasma Fibronectin: Conformational Change Induced by Calf Alveolar Heparan Sulfates. *Biochemistry*, 24(11):2661–2667, may 1985.

[144] C. Oxvig and T. A. Springer. Experimental support for a β-propeller domain in integrin α-subunits and a calcium binding site on its lower surface. *Proc. Natl. Acad. Sci. U. S. A.*, 95(9):4870–4875, apr 1998.

[145] Z. Pap, Z. Pávai, L. Dénes, I. Kovalszky, and J. Jung. An immunohistochemical study of colon adenomas and carcinomas: E-cadherin, Syndecan-1, Ets-1. *Pathol. Oncol. Res.*, 15(4):579–587, dec 2009.

[146] C. Partovian, R. Ju, Z. W. Zhuang, K. A. Martin, and M. Simons. Syndecan-4 Regulates Subcellular Localization of mTOR Complex2 and Akt Activation in a PKCα-Dependent Manner in Endothelial Cells. *Mol. Cell*, 32(1):140–149, oct 2008.

[147] K. C. Patterson, R. Yang, B. Zeng, B. Song, S. Wang, N. Xi, and M. D. Basson. Measurement of cationic and intracellular modulation of integrin binding affinity by AFM-Based nanorobot. *Biophys. J.*, 105(1):40–47, jul 2013.

[148] M. Pfaff, S. Liu, D. J. Erle, and M. H. Ginsberg. Integrin β cytoplasmic domains differentially bind to cytoskeletal proteins. *J. Biol. Chem.*, 273(11):6104–6109, mar 1998.

[149] A. Pierres, A. M. Benoliel, and P. Bongrand. Studying receptor-mediated cell adhesion at the single molecule level. *Cell Adhes. Commun.*, 5(5):375–95, jul 1998.

[150] M. D. Pierschbacher and E. Ruoslahti. Cell attachment activity of fibronectin can be duplicated by small synthetic fragments of the molecule. *Nature*, 309(5963):30–33, 1984.

[151] T. Pirzer and T. Hugel. Atomic force microscopy spring constant determination in viscous liquids. *Rev. Sci. Instrum.*, 80(3), 2009.

[152] E. F. Plow, T. A. Haas, L. Zhang, J. Loftus, and J. W. Smith. Ligand binding to integrins. *J. Biol. Chem.*, 275(29):21785–21788, jul 2000.

[153] L. H. Pope, M. C. Davies, C. A. Laughton, C. J. Roberts, S. J. Tendler, and P. M. Williams. Force-induced melting of a short DNA double helix. *Eur. Biophys. J.*, 30(1):53–62, 2001.

[154] K. Prechtel, A. R. Bausch, V. Marchi-Artzner, M. Kantlehner, H. Kessler, and R. Merkel. Dynamic Force Spectroscopy to Probe Adhesion Strength of Living Cells. *Phys. Rev. Lett.*, 89(2), 2002.

[155] J. R. Ramos, J. Pabijan, R. Garcia, and M. Lekka. The softening of human bladder cancer cells happens at an early stage of the malignancy process. *Beilstein J. Nanotechnol.*, 5(1):447–457, 2014.

[156] A. Rapraeger and M. Bernfield. Cell surface proteoglycan of mammary epithelial cells. Protease releases a heparan sulfate-rich ectodomain from a putative membrane-anchored domain. *J. Biol. Chem.*, 260(7):4103–9, apr 1985.

[157] A. Rapraeger, M. Jalkanen, and M. Bernfield. Cell surface proteoglycan associates with the cytoskeleton at the basolateral cell surface of mouse mammary epithelial cells. *J. Cell Biol.*, 103(6):2683–2696, dec 1986.

[158] B. M. Rapraeger AC. An integral membrane proteoglycan is capable of binding components of the cytoskeleton and the extracellular matrix. *Biosci. Rep.*, 9(2):265–269, apr 1982.

[159] S. Rasheed, M. B. Gardner, R. W. Rongey, W. A. Nelson-Rees, and P. Arnstein. Human bladder carcinoma: characterization of two new tumor cell lines and search for tumor viruses. *J. Natl. Cancer Inst.*, 58(4):881–90, apr 1977.

[160] S. Rasmussen and A. Rapraeger. Altered structure of the hybrid cell surface proteoglycan of mammary epithelial cells in response to transforming growth factor-beta. *J. Cell Biol.*, 107(5):1959–1967, 1988.

[161] A. M. Ray, F. Schaffner, H. Janouskova, F. Noulet, D. Rognan, I. Lelong-Rebel, L. Choulier, A. F. Blandin, M. Lehmann, S. Martin, T. Kapp, S. Neubauer, F. Rechenmacher, H. Kessler, and M. Dontenwill. Single cell tracking assay reveals an opposite effect of selective small non-peptidic $\alpha 5\beta 1$ or $\alpha \mathrm{v}\beta 3/\beta 5$ integrin antagonists in U87MG glioma cells. *Biochim. Biophys. Acta - Gen. Subj.*, 1840(9):2978–2987, 2014.

[162] S. D. Redick, D. L. Settles, G. Briscoe, and H. P. Erickson. Defining Fibronectin's cell adhesion synergy site by site-directed mutagenesis. *J. Cell Biol.*, 149(2):521–527, apr 2000.

[163] M. Rief, M. Gautel, F. Oesterhelt, J. M. Fernandez, and H. E. Gaub. Reversible unfolding of individual titin immunoglobulin domains by AFM. *Science*, 276(5315):1109–1112, may 1997.

[164] M. Rief, J. Pascual, M. Saraste, and H. E. Gaub. Single molecule force spectroscopy of spectrin repeats: Low unfolding forces in helix bundles. *J. Mol. Biol.*, 286(2):553–561, feb 1999.

[165] D. Riveline, E. Zamir, N. Q. Balaban, U. S. Schwarz, T. Ishizaki, S. Narumiya, Z. Kam, B. Geiger, and A. D. Bershadsky. Focal contacts as mechanosensors: Externally applied local mechanical force induces growth of focal contacts by an mDia1-dependent and ROCK-independent mechanism. *J. Cell Biol.*, 153(6):1175–1185, jun 2001.

[166] E. Ruoslahti and M. D. Pierschbacher. New perspectives in cell adhesion: RGD and integrins. *Science*, 238(4826):491–497, 1987.

[167] J. Sader. Atomic force microscope cantilevers. `http://www.ampc.ms.unimelb.edu.au/afm/calibration.html`. 2017-09-30.

[168] J. E. Sader, J. W. Chon, and P. Mulvaney. Calibration of rectangular atomic force microscope cantilevers. *Rev. Sci. Instrum.*, 70(10):3967–3969, 1999.

[169] J. E. Sader, I. Larson, P. Mulvaney, and L. R. White. Method for the calibration of atomic force microscope cantilevers. *Rev. Sci. Instrum.*, 66(7):3789–3798, 1995.

[170] J. E. Sader, J. Pacifico, C. P. Green, and P. Mulvaney. General scaling law for stiffness measurement of small bodies with applications to the atomic force microscope. *J. Appl. Phys.*, 97(12), 2005.

[171] J. E. Sader, J. A. Sanelli, B. D. Adamson, J. P. Monty, X. Wei, S. A. Crawford, J. R. Friend, I. Marusic, P. Mulvaney, and E. J. Bieske. Spring constant calibration of atomic force microscope cantilevers of arbitrary shape. *Rev. Sci. Instrum.*, 83(10), oct 2012.

[172] R. D. Sanderson and M. Bernfield. Molecular polymorphism of a cell surface proteoglycan: Distinct structures on simple and stratified epithelia. *Proc. Natl. Acad. Sci. U. S. A.*, 85(24):9562–9566, 1988.

[173] P. Santala and J. Heino. Regulation of integrin-type cell adhesion receptors by cytokines. *J. Biol. Chem.*, 266(34):23505–9, dec 1991.

[174] E. Sariisik, C. Popov, J. P. Müller, D. Docheva, H. Clausen-Schaumann, and M. Benoit. Decoding Cytoskeleton-Anchored and Non-Anchored Receptors from Single-Cell Adhesion Force Data. *Biophys. J.*, 109(7):1330–1333, oct 2015.

[175] S. Saunders and M. Bernfield. Cell surface proteoglycan binds mouse mammary epithelial cells to fibronectin and behaves as a receptor for interstitial matrix. *J. Cell Biol.*, 106(2):423–430, 1988.

[176] S. Saunders, M. Jalkanen, S. O'Farrell, and M. Bernfield. Molecular cloning of syndecan, an integrated membrane proteoglycan. *J. Cell Biol.*, 108(4):1547–1556, 1989.

[177] H. Schillers, C. Rianna, J. Schäpe, T. Luque, H. Doschke, M. Wälte, J. J. Uriarte, N. Campillo, G. P. Michanetzis, J. Bobrowska, A. Dumitru, E. T. Herruzo, S. Bovio, P. Parot, M. Galluzzi, A. Podestà, L. Puricelli, S. Scheuring, Y. Missirlis, R. Garcia, M. Odorico, J. M. Teulon, F. Lafont, M. Lekka, F. Rico, A. Rigato, J. L. Pellequer, H. Oberleithner, D. Navajas, and M. Radmacher. Standardized Nanomechanical Atomic Force Microscopy Procedure (SNAP) for Measuring Soft and Biological Samples. *Sci. Rep.*, 7(1), dec 2017.

[178] Y. Shan, J. Huang, J. Tan, G. Gao, S. Liu, H. Wang, and Y. Chen. The study of single anticancer peptides interacting with HeLa cell membranes by single molecule force spectroscopy. *Nanoscale*, 4(4):1283–1286, feb 2012.

[179] X. Shi, Y. Q. Ma, Y. Tu, K. Chen, S. Wu, K. Fukuda, J. Qin, E. F. Plow, and C. Wu. The MIG-2/integrin interaction strengthens cell-matrix adhesion and modulates cell motility. *J. Biol. Chem.*, 282(28):20455–20466, jul 2007.

[180] M. Shimaoka, J. Takagi, and T. A. Springer. Conformational regulation of integrin structure and function. *Annu. Rev. Biophys. Biomol. Struct.*, 31:485–516, 2002.

[181] M. Shimaoka, T. Xiao, J. H. Liu, Y. Yang, Y. Dong, C. D. Jun, A. McCormack, R. Zhang, A. Joachimiak, J. Takagi, J. H. Wang, and T. A. Springer. Structures of the αL I domain and its complex with ICAM-1 reveal a shape-shifting pathway for integrin regulation. *Cell*, 112(1):99–111, jan 2003.

[182] J. Shin, W. Lee, D. Lee, B. K. Koo, I. Han, Y. Lim, A. Woods, J. R. Couchman, and E. S. Oh. Solution structure of the dimeric cytoplasmic domain of syndecan-4. *Biochemistry*, 40(29):8471–8478, jul 2001.

[183] M. L. Smith, D. Gourdon, W. C. Little, K. E. Kubow, R. A. Eguiluz, S. Luna-Morris, and V. Vogel. Force-induced unfolding of fibronectin in the extracellular matrix of living cells. *PLoS Biol.*, 5(10):2243–2254, oct 2007.

[184] S. B. Smith, L. Finzi, and C. Bustamante. Direct mechanical measurements of the elasticity of single DNA molecules by using magnetic beads. *Science*, 258(5085):1122–1126, 1992.

[185] A. Sobiepanek, M. Milner-Krawczyk, M. Lekka, and T. Kobiela. AFM and QCM-D as tools for the distinction of melanoma cells with a different metastatic potential. *Biosens. Bioelectron.*, 93:274–281, jul 2017.

[186] T. A. Springer and J. H. Wang. The three-dimensional structure of integrins and their ligands, and conformational regulation of cell adhesion. *Adv. Protein Chem.*, 68:29–63, 2004.

[187] R. W. Stark, T. Drobek, and W. M. Heckl. Thermomechanical noise of a free v-shaped cantilever for atomic-force microscopy. *Ultramicroscopy*, 86(1-2):207–15, jan 2001.

[188] D. F. Sticke, L. G. Presta, K. A. Dill, and G. D. Rose. Hydrogen bonding in globular proteins. *J. Mol. Biol.*, 226(4):1143–1159, may 1992.

[189] J. K. Stuart and V. Hlady. Effects of Discrete Protein-Surface Interactions in Scanning Force Microscopy Adhesion Force Measuremenss. *Langmuir*, 11(4):1368–1374, apr 1995.

[190] J. E. Sun, J. Vranic, R. J. Composto, C. Streu, P. C. Billings, J. S. Bennett, J. W. Weisel, and R. I. Litvinov. Bimolecular integrin-ligand interactions quantified using peptide-functionalized dextran-coated microparticles. *Integr. Biol.*, 4(1):84–92, jan 2012.

[191] X. Sun, D. F. Mosher, and A. Rapraeger. Heparan sulfate-mediated binding of epithelial cell surface proteoglycan to thrombospondin. *J. Biol. Chem.*, 264(5):2885–9, feb 1989.

[192] Z. Sun, L. A. Martinez-Lemus, A. Trache, J. P. Trzeciakowski, G. E. Davis, U. Pohl, and G. A. Meininger. Mechanical properties of the interaction between fibronectin and $\alpha 5\beta 1$-integrin on vascular smooth muscle cells studied using atomic force microscopy. *Am. J. Physiol. - Hear. Circ. Physiol.*, 289(6 58-6), dec 2005.

[193] T. Szarvas, H. Reis, G. Kramer, S. F. Shariat, F. Vom Dorp, S. Tschirdewahn, K. W. Schmid, I. Kovalszky, and H. Rübben. Enhanced stromal syndecan-1 expression is an independent risk factor for poor survival in bladder cancer. *Hum. Pathol.*, 45(4):674–682, 2014.

[194] S. Tadokoro, S. J. Shattil, K. Eto, V. Tai, R. C. Liddington, J. M. De Pereda, M. H. Ginsberg, and D. A. Calderwood. Talin binding to integrin β tails: A final common step in integrin activation. *Science*, 302(5642):103–106, oct 2003.

[195] J. Takagi, H. P. Erickson, and T. A. Springer. C-terminal opening mimics 'inside-out' activation of integrin $\alpha 5\beta$ 1. *Nat. Struct. Biol.*, 8(5):412–416, 2001.

[196] J. Takagi, B. M. Petre, T. Walz, and T. A. Springer. Global conformational earrangements in integrin extracellular domains in outside-in and inside-out signaling. *Cell*, 110(5):599–611, sep 2002.

[197] J. W. Tamkun, D. W. DeSimone, D. Fonda, R. S. Patel, C. Buck, A. F. Horwitz, and R. O. Hynes. Structure of integrin, a glycoprotein involved in

the transmembrane linkage between fibronectin and actin. *Cell*, 46(2):271–282, jul 1986.

[198] Y. Taniguchi and M. Kawakami. Variation in the Mechanical Unfolding Pathway of p53DBD Induced by Interaction with p53 N-Terminal Region or DNA. *PLoS One*, 7(11), nov 2012.

[199] A. Taninaka, Y. Hirano, O. Takeuchi, and H. Shigekawa. Force measurement enabling precise analysis by dynamic force spectroscopy. *Int. J. Mol. Sci.*, 13(1):453–465, 2012.

[200] A. Taubenberger, D. A. Cisneros, J. Friedrichs, P.-H. Puech, D. J. Muller, and C. M. Franz. Revealing early steps of alpha2beta1 integrin-mediated adhesion to collagen type I by using single-cell force spectroscopy. *Mol. Biol. Cell*, 18(5):1634–44, may 2007.

[201] J. te Riet, A. J. Katan, C. Rankl, S. W. Stahl, A. M. van Buul, I. Y. Phang, A. Gomez-Casado, P. Schön, J. W. Gerritsen, A. Cambi, A. E. Rowan, G. J. Vancso, P. Jonkheijm, J. Huskens, T. H. Oosterkamp, H. Gaub, P. Hinterdorfer, C. G. Figdor, and S. Speller. Interlaboratory round robin on cantilever calibration for AFM force spectroscopy. *Ultramicroscopy*, 111(12):1659–1669, dec 2011.

[202] D. F. Tees, R. E. Waugh, and D. A. Hammer. A microcantilever device to assess the effect of force on the lifetime of selectin-carbohydrate bonds. *Biophys. J.*, 80(2):668–82, feb 2001.

[203] V. Thamilselvan, M. Fomby, M. Walsh, and M. D. Basson. Divalent cations modulate human colon cancer cell adhesion. *J. Surg. Res.*, 110(1):255–65, mar 2003.

[204] I. Thesleff, M. Jalkanen, S. Vainio, and M. Bernfield. Cell surface proteoglycan expression correlates with epithelial-mesenchymal interaction during tooth morphogenesis. *Dev. Biol.*, 129(2):565–572, 1988.

[205] M. S. Trautman and J. Kimelmant. Developmental expression of syndecan, an integral membrane proteoglycan, correlates with cell differentiation. *Development*, 111:213–220, 1991.

[206] UniProt. vitronectin structure. `https://uniprot.org/blast/?about=P04004[20-478]&key=Chain&id=PRO_0000036394`, ? 2019-09-10.

[207] O. Vinogradova, A. Velyvis, A. Velyviene, B. Hu, T. Haas, E. Plow, and J. Qin. A structural mechanism of integrin alpha(IIb)beta(3) "inside-out" activation as regulated by its cytoplasmic face. *Cell*, 110(5):587–97, 2002.

[208] F. M. Watt, M. D. Kubler, N. A. Hotchin, L. J. Nicholson, and J. C. Adams. Regulation of keratinocyte terminal differentiation by integrin-extracellular matrix interactions. *J. Cell Sci.*, 106(1):175–182, 1993.

[209] R. C. Weast. *CRC handbook of chemistry and physics*. CRC Press, 65 edition, 1984.

[210] B. Wehrle-Haller and B. A. Imhof. Integrin-dependent pathologies. *J. Pathol.*, 200(4):481–487, jul 2003.

[211] T.-Q. Wei, D.-Y. Luo, L. Chen, T. Wu, and K.-J. Wang. Cyclic hydrodynamic pressure induced proliferation of bladder smooth muscle cells via integrin alpha5 and FAK. *Physiol. Res.*, 63(1):127–34, 2014.

[212] P. H. Weinreb, S. Li, S. X. Gao, T. Liu, R. B. Pepinsky, J. A. Caravella, J. H. Lee, and V. L. Woods. Dynamic structural changes are observed upon collagen and metal ion binding to the integrin α1 I domain. *J. Biol. Chem.*, 287(39):32897–32912, sep 2012.

[213] M. Weitzhandler, H. B. Streeter, W. J. Henzel, and M. Bernfield. The cell surface proteoglycan of mouse mammary epithelial cells. The extracellular domain contains N terminus and a peptide sequence present in a conditioned medium proteoglycan. *J. Biol. Chem.*, 263(15):6949–52, may 1988.

[214] J. R. Whiteford, V. Behrends, H. Kirby, M. Kusche-Gullberg, T. Muramatsu, and J. R. Couchman. Syndecans promote integrin-mediated adhesion of mesenchymal cells in two distinct pathways. *Exp. Cell Res.*, 313(18):3902–3913, nov 2007.

[215] K. E. Wilson, S. P. Langdon, A. M. Lessells, and W. R. Miller. Expression of the extracellular matrix protein tenascin in malignant and benign ovarian tumours. *Br. J. Cancer*, 74(7):999–1004, 1996.

[216] E. P. Wojcikiewicz, X. Zhang, and V. T. Moy. Force and compliance measurements on living cells using atomic force microscopy (AFM). *Biol. Proced. Online*, 6(1):1–9, jan 2004.

[217] A. Woods, J. R. Couchman, S. Johansson, and M. Höök. Adhesion and cytoskeletal organisation of fibroblasts in response to fibronectin fragments. *EMBO J.*, 5(4):665–70, apr 1986.

[218] A. Woods, R. L. Longley, S. Tumova, and J. R. Couchman. Syndecan-4 binding to the high affinity heparin-binding domain of fibronectin drives focal adhesion formation in fibroblasts. *Arch. Biochem. Biophys.*, 374(1):66–72, feb 2000.

[219] Y. Wu, Y. Huang, B. P. Herring, and S. J. Gunst. Integrin-linked kinase regulates smooth muscle differentiation marker gene expression in airway tissue. *Am. J. Physiol. - Lung Cell. Mol. Physiol.*, 295(6), dec 2008.

[220] I. Xanthis, C. Souilhol, J. Serbanovic-Canic, H. Roddie, A. C. Kalli, M. Fragiadaki, R. Wong, D. R. Shah, J. A. Askari, L. Canham, N. Akhtar, S. Feng, V. Ridger, J. Waltho, E. Pinteaux, M. J. Humphries, M. T. Bryan, and P. C. Evans. β1 integrin is a sensor of blood flow direction. *J. Cell Sci.*, 132(11), jun 2019.

[221] T. Xia, J. Takagi, B. S. Coller, J. H. Wang, and T. A. Springer. Structural basis for allostery in integrins and binding to fibrinogen-mimetic therapeutics. *Nature*, 432(7013):59–67, nov 2004.

[222] J.-P. Xiong, T. Stehle, S. L. Goodman, and M. A. Arnaout. Integrins, cations and ligands: making the connection. *J. Thromb. Haemost.*, 1(7):1642–1654, jul 2003.

[223] J. P. Xiong, T. Stehle, R. Zhang, A. Joachimiak, M. Frech, S. L. Goodman, and M. A. Arnaout. Crystal structure of the extracellular segment of integrin αVβ3 in complex with an Arg-Gly-Asp ligand. *Science*, 296(5565):151–155, apr 2002.

[224] S.-T. Xu, F.-Z. Zou, L.-N. Cai, and W.-L. Xu. The downregulation of OPN inhibits proliferation and migration and regulate activation of Erk1/2 in ECA-109 cells. *Int. J. Clin. Exp. Med.*, 8(4):5361–9, 2015.

[225] Y. Yang, V. MacLeod, H. Q. Miao, A. Theus, F. Zhan, J. D. Shaughnessy, J. Sawyer, J. P. Li, E. Zcharia, I. Vlodavsky, and R. D. Sanderson. Heparanase enhances syndecan-1 shedding: A novel mechanism for stimulation of tumor growth and metastasis. *J. Biol. Chem.*, 282(18):13326–13333, may 2007.

[226] A. Zaravinos, G. I. Lambrou, D. Volanis, D. Delakas, and D. A. Spandidos. Spotlight on Differentially Expressed Genes in Urinary Bladder Cancer. *PLoS One*, 6(4):e18255, apr 2011.

[227] D. Zhang, A. E. Hudson, C. F. Delostrinos, N. Carmean, R. Eastman, B. Hicks, R. E. Hurst, and J. A. Bassuk. Dual sources of vitronectin in the human lower urinary tract: Synthesis by urothelium vs. extravasation from the bloodstream. *Am. J. Physiol. - Ren. Physiol.*, 300(2), feb 2011.

[228] J. Zhang, G. Wu, C. Song, Y. Li, H. Qiao, P. Zhu, P. Hinterdorfer, B. Zhang, and J. Tang. Single Molecular Recognition Force Spectroscopy Study of a Luteinizing Hormone-Releasing Hormone Analogue as a Carcinoma Target Drug. *J. Phys. Chem. B*, 116(45):13331–13337, nov 2012.

[229] X. Zhang, A. Chen, D. De Leon, H. Li, E. Noiri, V. T. Moy, and M. S. Goligorsky. Atomic force microscopy measurement of leukocyte-endothelial interaction. *Am. J. Physiol. - Hear. Circ. Physiol.*, 286(1 55-1), jan 2004.

[230] Z. Zhang, A. O. Morla, K. Vuori, J. S. Bauer, R. L. Juliano, and E. Ruoslahti. The αvβ1 integrin functions as a fibronectin receptor but does not support fibronectin matrix assembly and cell migration on fibronectin. *J. Cell Biol.*, 122(1):235–242, 1993.

[231] G. Zhao, J. Cui, Q. Qin, J. Zhang, L. Liu, S. Deng, C. Wu, M. Yang, S. Li, and C. Wang. Mechanical stiffness of liver tissues in relation to integrin β1 expression may influence the development of hepatic cirrhosis and hepatocellular carcinoma. *J. Surg. Oncol.*, 102(5):482–489, jun 2010.

[232] W. Zhao, M. Cai, H. Xu, J. Jiang, and H. Wang. A single-molecule force spectroscopy study of the interactions between lectins and carbohydrates on cancer and normal cells. *Nanoscale*, 5(8):3226–3229, apr 2013.